ABSTRACT

Title of Thesis: HIGHLY EXTENSIBLE SKIN FOR A VARIABLE WING-SPAN MORPHING AIRCRAFT UTILIZING PNEUMATIC ARTIFICIAL MUSCLE ACTUATION.

Edward A. Bubert, Master of Science, 2009

Thesis Directed By: Professor Norman M. Wereley
Department of Aerospace Engineering

Two different technologies are demonstrated for a span-morphing wingtip: a linear controller for a pneumatic artificial muscle (PAM) actuator, and a passive 1-D morphing skin. A generic PAM system incorporating a single PAM working against a nonlinear spring is described in a Simulink model, which is validated using experimental data. A linear PID controller is then incorporated into the model. Frequency responses are obtained by both simulation and experiment, and the ability to track relatively high frequency control inputs is demonstrated. The morphing skin system includes an elastomer-fiber-composite surface layer that is supported by a flexible honeycomb structure, each of which exhibit a near-zero in-plane Poisson's ratio. Composite skin and substructure configurations are designed using analytical methods and downselected after experimental evaluation. A complete prototype morphing skin, mated to a PAM driven extension mechanism, demonstrates 100% uniaxial extension accompanied by a 100% increase in surface area. Out-of-plane deflections under surface pressures up to 200 psf (9.58 kPa) are reported at varying levels of area change.

HIGHLY EXTENSIBLE SKIN FOR A VARIABLE WING-SPAN MORPHING AIRCRAFT UTILIZING PNEUMATIC ARTIFICIAL MUSCLE ACTUATION.

By

Edward A. Bubert

Thesis submitted to the Faculty of the Graduate School of the
University of Maryland, College Park, in partial fulfillment
of the requirements for the degree of
Master of Science
2009

Advisory Committee:
Professor Norman M. Wereley, Chair
Professor Christopher Cadou
Professor J. Sean Humbert

Acknowledgments

I would like to begin by thanking my advisor, Dr. Norman Wereley, who has been a reliable source of knowledge and guidance, and the other members of my graduate committee, Dr. Christopher Cadou and Dr. Sean Humbert, for their advice and help in preparing this thesis.

Much of the work presented here was done with the support of Techno-Sciences, Inc. under Dr. Peter Chen. Additional thanks go to Dr. Curt Kothera for his invaluable assistance during testing and analysis.

For the work in Chapter 3, sponsorship was provided by the Air Force Research Laboratory (AFRL) through a Phase I STTR, contract number FA9550-06-C-0132. I would like to thank technical monitors Drs. Brian Sanders and Victor Giurgiutiu for their contributions.

Finally, I would like to thank my friends and coworkers at the University of Maryland, in particular Ben Woods, Robert Vocke, and Michael Gentry, for help in all aspects of executing this research.

Table of Contents

List of Figures

List of Tables

List of Notations

A = proportional spool valve orifice area

$[A]$ = extensional stiffness matrix for orthotropic composite lamina

$[B]$ = coupling stiffness matrix for orthotropic composite lamina

b = depth of honeycomb cell

c = honeycomb cell width

C_d = discharge coefficient for orifice mass flow

C_1 = subsonic mass flow term

C_2 = supersonic mass flow term

CLPT = Classical Laminated Plate Theory

$[D]$ = bending stiffness matrix for orthotropic composite lamina

D_t = tubing diameter

E = Young's modulus

E_f = FMC fiber modulus

$E_\mathbf{L}$ = longitudinal elastic modulus for orthotropic composite lamina

$E_\mathbf{T}$ = transverse elastic modulus for orthotropic composite lamina

E_m = FMC matrix modulus

E_0 = honeycomb material elastic modulus

E_1 = effective honeycomb elastic modulus

E_2 = transverse or spanwise FMC elastic modulus

F = force on honeycomb bending member during extension

f = Moody friction factor for internal flow

F_p = PAM actuator force

FMC = Flexible Matrix Composite

$G_{\mathbf{LT}}$ = shear modulus for unidirectional composite lamina

h = honeycomb cell height

h_k = distance of top of k^{th} lamina from bottom of laminate

$h_{k\text{-}1}$ = distance of bottom of k^{th} lamina from bottom of laminate

I = honeycomb bending member second moment of area

L_{a} = length of actuator in x-frame mechanism

L_{ap} = distance of actuator mounting from center of x-frame mechanism

L_{t} = length of tubing between valve and volume to be filled

L_{x} = chordwise length of x-frame actuator

L_{y} = spanwise length of x-frame actuator

$L_{\text{P,0}}$ = PAM resting length

ℓ = length of honeycomb bending member leg

$\{M\}$ = vector of CLPT laminate in-plane moments

$\dot{m}$ = mass flow rate through orifice

$\dot{m}_{delay}$ = mass flow rate through orifice, delayed by tubing length

$\{N\}$ = vector of CLPT laminate in-plane forces

n = number of laminae in FMC composite

P = PAM actuator pressure

PAM = Pneumatic Artificial Muscle

P_{cr} = critical pressure ratio for orifice flow

PI = proportional-integral linear controller

PID = proportional-integral-derivative linear controller

P_u = upstream pressure in orifice flow calculation

P_d = downstream pressure in orifice flow calculation

$[Q]$ = lamina stiffness matrix in material axes

$[\bar{Q}]$ = lamina stiffness matrix in laminate body axes

R = gas constant for fluid during mass flow

Re_D = Reynolds number inside tubing

r_d = reference displacement for SPTA linear controller

R_t = resistance in tubing due to fluid viscosity

RTV = Room Temperature Vulcanization

$[S]$ = lamina compliance matrix in material axes

SPTA = Single PAM Test Apparatus

T = ambient temperature

t = thickness of honeycomb bending member

t_s = FMC laminate skin thickness

UAV = Unmanned Aerial Vehicle

u_d = control input to SPTA proportional valve

V = PAM actuator volume

V_f = FMC lamina fiber volume fraction

α = specific heat constant for fluid undergoing changing volume

α_{in} = approximate specific heat constant for pressure change due to inflow

α_{out} = approximate specific heat constant for pressure change due to exhaust

γ = ratio of specific heats for fluid during orifice mass flow

ΔL_P = change in PAM length, contraction is positive

ΔP = pressure drop along length of tubing

δ = deflection of honeycomb bending bending member

$\{\varepsilon_0\}$ = vector of CLPT laminate mid-plane strains

ε = PAM actuator non-dimensionalized contraction

ε_1 = global honeycomb strain

θ = angle between honeycomb rib member and bending member

θ_f = fiber offset angle, measured from chordwise (**1**) axis

μ = fluid viscosity

ν = honeycomb material Poisson's ratio

$\nu_{\mathbf{LT}}$ = major Poisson's ratio of orthotropic composite lamina

ν_{21} = minor Poisson's ratio for an FMC laminate

σ_1 = effective global honeycomb stress

τ = mass flow time delay due to tubing length

Φ = tubing loss term providing mass flow amplitude attenuation

Chapter 1

Introduction

1.1 Morphing Overview

Since the Wright Brothers' first flight, the idea of changing an airplane's aerodynamic characteristics through continuous shape change, rather than discrete flaps or moving surfaces, has held the promise of more efficient flight. While the Wrights used a technique known as wing warping, or twisting the wings through structural deformation to control the roll of the aircraft [1], any number of possible morphological changes could be undertaken to modify an aircraft's flight path or overall performance. Some notable examples include the Parker Variable Camber Wing used for increased forward speed [2], the impact of a variable dihedral wing on aircraft stability [3], the high speed dash/low speed cruise abilities associated with wings of varying sweep [4], and the multiple benefits of cruise/dash performance and efficient roll control gained through telescopic wingspan changes [5, 6, 7].

While the aforementioned concepts focused on large-scale, manned aircraft, morphing technology is certainly not limited to vehicles of this size. In fact, the development of a new generation of unmanned aerial vehicles (UAVs), combined with advances in actuator and materials technology, has spawned renewed interest in radical morphing configurations capable of matching multiple mission profiles through shape change – this class has come to be referred to as "morphing aircraft" [8]. Contemporary research is primarily dedicated to various wing configuration changes, namely, twist, camber, span,

and sweep. It has been shown that morphing adjustments in the planform of a wing without hinged surfaces leads to improved roll performance, which can expand the flight envelope of an aircraft [9]. More specifically, morphing to increase the span of a wing results in a reduction in induced drag, allowing for increased range or endurance [10]. The research presented here is intended for just such a span-morphing application, for example a UAV with span-morphing wingtips depicted in Fig. 1. By achieving large changes in the span dimension over a small section of wing, the wing aspect ratio can be optimized in-flight for different roles. Furthermore, differential span change between wingtips can generate a roll moment, potentially replacing ailerons on the aircraft [11].

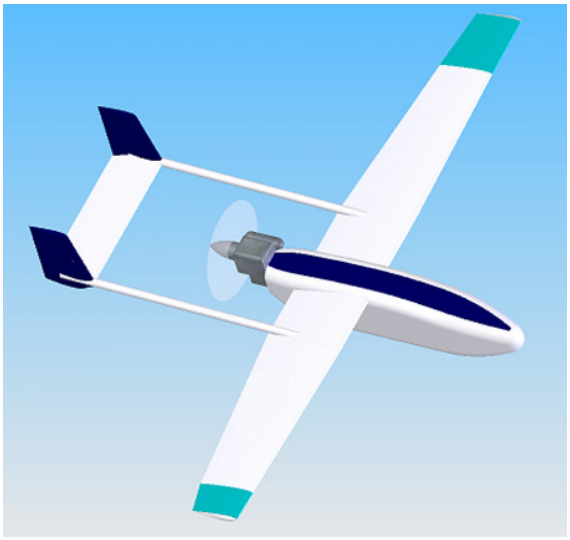

Fig. 1: Span-morphing UAV showing 1-D morphing wingtips.

1.2 Morphing Skin Review

A key challenge in developing a span-morphing wingtip is the development of a useful morphing skin, defined here as a continuous layer of material that would stretch over the morphing structure and mechanism to form a smooth aerodynamic skin surface. For a span-morphing wingtip in particular, the necessity of a high degree of surface area change, large strain capability in the span direction, and little to no strain in the

chordwise direction, all impose difficult requirements on any proposed morphing skin. The goal of this effort was a 100% increase in both the span and area of a morphing wing tip, or morphing cell.

A review of contemporary morphing skin technology [12] yields three major areas of research being pursued: compliant structures, shape memory polymers, and anisotropic elastomeric skins. Compliant structures such as the FlexSys Inc. Mission Adaptive Compliant Wing (MACW) rely on an internal structure tailored to deform in a prescribed manner to allow small amounts of trailing edge camber change [13]. Because only small deformations are needed, conventional metal or resin-matrix-composite skin materials can be used to carry aerodynamic loads. Due to the large geometrical changes required for a span-morphing wingtip as envisioned here, metal or resin-matrix-composite skin materials are unsuitable because they are simply unable to achieve the desired goal of 100% increases in morphing cell span and area.

Shape memory polymer (SMP) skin materials are relatively new and have recently received attention for morphing aircraft concepts. They may at first glance seem highly suited to a span-morphing wingtip: shape memory polymers made by Cornerstone Research Group [14] exhibit an order of magnitude reduction in modulus and up to 200% strain capability when heated past a transition temperature, yet return to their original modulus upon cooling. This would allow a skin to hold its shape under aerodynamic loads in different morphed positions, yet be made soft enough to morph to new positions with low actuation forces. There have been attempts to capitalize on the capabilities of SMP skins, such as Lockheed Martin's Z-wing morphing UAV concept [15]. However, electrical heating of the SMP skin to reach transition temperature proved difficult to

implement in the wind tunnel test article and the SMP skin was abandoned as a high-risk option. Additionally, the time required for heating SMP material to transition appears to make it ill-suited for dynamic control morphing objectives.

With maximum strains above 100%, low stiffness, and a lower degree of risk due to their passive operation, elastomeric materials are ideal candidates for a morphing skin [16]. Isotropic elastomer morphing skins have been successfully implemented on the MFX-1 UAV [17]. This UAV employs a mechanized sliding spar wing structure capable of altering the sweep, wing area, and aspect ratio during flight. Sheets of silicone elastomer connect rigid leading and trailing edge spars, forming the upper and lower surfaces of the wing. The elastomer skin is reinforced against out-of-plane loads by ribbons stretched taught immediately underneath the skin, which proved effective for wind tunnel testing and flight testing. Not seen in literature at the start of this research were any examples of elastomeric skins tailored specifically for span-morphing applications with a suitable supporting substructure to withstand aerodynamic loads.

1.3 Span Morphing Actuation Mechanism

A complete span morphing wing system would incorporate a morphing skin as well as a mechanized supporting structure to provide actuation power to the skin surface and transfer aerodynamic loads to the rest of the wing. Strain capability is once again a primary motivating factor, with an overall goal of 100% length change. Weight is also a critical factor in any aircraft design, especially for an actuator system situated at the wingtip, where the impact on wing root bending moment will be greatest. Background work focused on the selection and development of a high length change extending mechanism using a high power density pneumatic artificial muscle actuator [18].

1.3.1 PAM Actuators

McKibben actuators, the type of pneumatic artificial muscle (PAM) used in this study, consist of a rubber bladder surrounded by a braided sleeve attached at each end to rigid fittings, as seen in Fig. 2. Upon inflation of the bladder by a working fluid (in this case air), the bladder and braid will expand radially. Because the braid fibers are relatively stiff and fixed at each end, in order to expand radially the braided sleeve will necessarily have to contract axially. If unloaded, contraction will continue until the angle between braid fibers which yields the maximum internal volume is achieved, as in Fig. 2b. This point corresponds to the minimum energy state, where internal pressure is minimized for a given mass of air [19]. If contraction is opposed by a load, the pressure within the PAM will generate axial tension which seeks to return the PAM to the minimum energy state. This return force is directly proportional to internal pressure and decreases with contraction ratio (defined here as $\varepsilon = \Delta L_P / L_{P,0}$, with contraction positive) as seen in a typical set of constant pressure actuator load lines in Fig. 3. Significant forces and displacements can be attained by very simple, lightweight PAM actuators, with power to weight ratios over 1 kW/kg possible at 250 kPa [20] and typical free contraction ratio of 25-30%. Actuation frequency is determined by the volume of the PAM and the flow capacity of the pneumatic system.

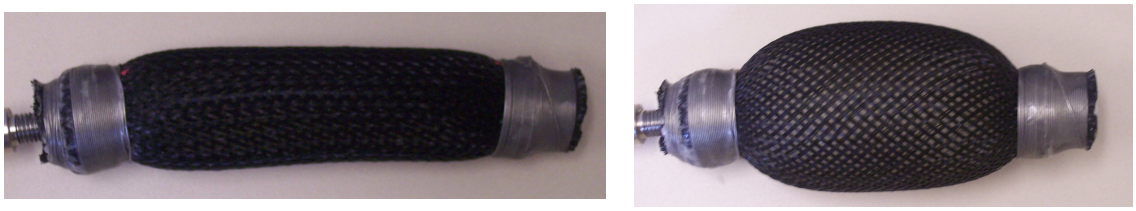

(a) **(b)**

Fig. 2: Pneumatic artificial muscle (a) at rest; (b) inflated, free contraction.

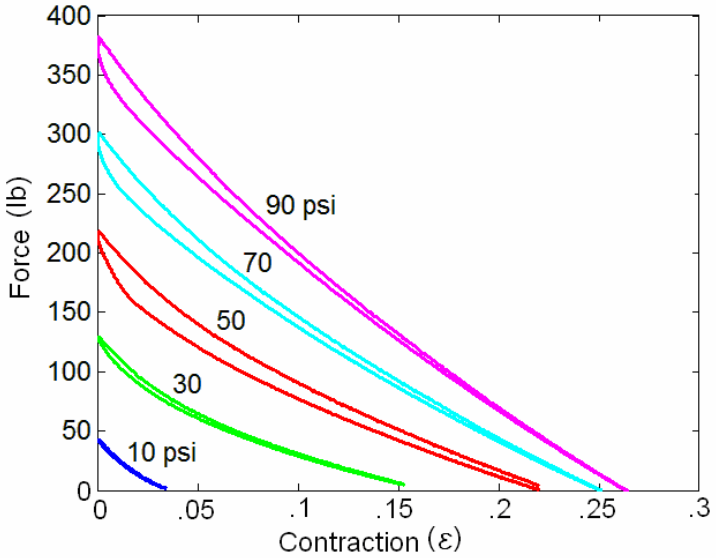

Fig. 3: Typical PAM load line characterization.

Actuator performance is dependent on a number of design variables explored by Kothera et al. [21]. The material selection for both braid and bladder will affect strain energy losses; a stiff braid and a compliant bladder being desirable for increased blocked force and free contraction. Similarly, a thicker bladder will incur higher losses and hysteresis due to greater stiffness. Increasing actuator length has little impact on either blocked force or contraction ratio but naturally yields greater free contraction and thus greater work output, while increasing the overall diameter will result in higher force levels. Furthermore, blocked force and contraction ratio are highly dependent on the resting braid angle as this determines the amount of work that can be performed before the actuator has reached the minimum energy braid angle [22].

Since their introduction over 50 years ago [23], pneumatic artificial muscles have seen little use outside of limited robotics applications, where the natural compliance of the actuator makes it appealing for working in close contact with humans [24]. The compressibility of the working fluid and the flexible rubber/braid construction give the

actuator compliance through low stiffness, but also makes position control difficult under dynamic loads [20]. Hysteresis due to braid/bladder friction, the compressibility of air, and the flexibility of the bladder all result in a highly nonlinear system with a constantly changing pressure-position relationship, suggesting the need for an accurate system model and a robust controller [25]. Using a PAM actuation mechanism therefore requires development of a closed loop controller.

1.3.2 Pneumatic Artificial Muscle Control Review

In the past twenty years, many papers have been written on the topic of closed loop pneumatic controls, including a number of papers dealing specifically with control of PAMs. The selections of both the control algorithm and the mechanical pressure or flow control device have large impacts on the capabilities of the system. The use of electronic pressure regulators and two PI feedback loops seems to guarantee a stable PAM system, but with very poor bandwidth [25]. Discrete proportional control also succeeds at inducing a limit cycle in a variable stiffness PAM joint using pulse width modulation [30]. Nonlinear and adaptive controllers appear to be preferred in the literature for position control of PAM systems, with a number of pulse width modulation systems with good low bandwidth operation [19,26]. When coupled with proportional valves, nonlinear controllers exhibit impressive performance in pneumatic systems. One example uses a nonlinear controller to allow a PAM to track large step inputs [29], and another example controls a pneumatic piston with very low error at upwards of 20 Hz [27].

A summary of selected pneumatic control studies has been provided in Table 1. For each study, the table details the type of pneumatic control element used (electronic pressure regulator, pulse width modulation, or proportional valves), the closed loop

control method used, and the maximum frequency of operation described. Where no operating frequency was mentioned, an estimate has been made based on figures provided, with estimated frequencies marked by an asterisk.

Table 1: Results of selected pneumatic actuator control studies.

Authors	Year	Actuator Type	Control Element	Controller Type	Actuation Frequency
Schroeder et al [25]	2003	PAM	Pressure Reg.	Cascading PI	<<1 Hz
Tondu & Lopez [24]	2000	PAM	Pressure Reg.	Sliding Mode	<<1 Hz
Caldwell et al [19]	1995	PAM	PWM	Adaptive Linear	<1 Hz
Paul et al [26]	1994	Piston	PWM	Sliding Mode	<1 Hz
Hildebrandt et al [28]	2002	PAM	Proportional	Sliding Mode	~5 Hz
Richer & Hurmuzlu [27]	2000	Piston	Proportional	Sliding Mode	>20 Hz

The studies in Table 1 employed a mix of linear and nonlinear controls. Based upon the inherit nonlinearities of pneumatic systems, more impressive bandwidth would be expected from systems using nonlinear sliding mode control in Table 1. However, there appears to be no consistency in this regard, with one nonlinear controller achieving frequencies upwards of 20 Hz while others are demonstrated at significantly less than 1 Hz. The two studies which achieved the highest bandwidth used proportional control valves rather than electronic pressure regulators or pulse width modulation (PWM) as in the other studies. Missing from the literature are any studies where the benefits of proportional valves are used in conjunction with linear rather than nonlinear control methods.

1.3.3 X-Frame Extension Mechanism

In order to make use of a PAM in a wing-span morphing application, a mechanism is needed to transform the PAM's contractile force into an extension force. The following is a summary of parallel development done by Kothera and Wereley [18] of a scissoring "x-frame" extension mechanism specifically for a morphing wingtip utilizing the morphing skin described in this research. The x-frame design, shown in Fig. 4, converts the contraction of the PAM actuator into extension output needed in a span-morphing wing. In this design, the PAM actuators are oriented chordwise, with the inboard end of the mechanism fixed to the wing and the moving outboard end attached to a rigid wingtip cap. The section in between would be bridged by a morphing section utilizing a morphing skin.

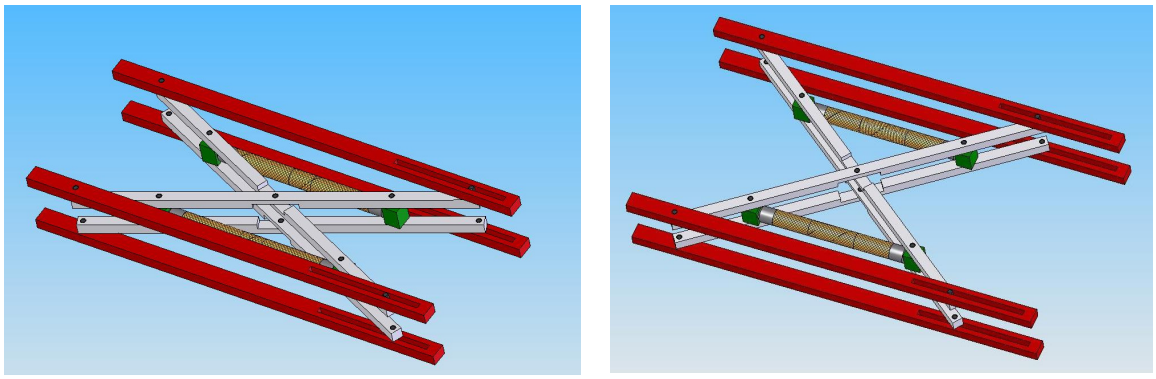

(a) **(b)**

Fig. 4: PAM-driven x-frame actuation mechanism concept (a) fully contracted; (b) fully extended [18].

Using the x-frame geometry as defined in Fig. 5, a set of kinematic equations can be derived to predict the force and displacement output based on PAM actuator performance.

$$\frac{F_y}{F_x} = \frac{L_{ap}}{L/2}\tan\theta \tag{1}$$

$$\frac{L_y}{L_a} = \frac{L/2}{L_{ap}} \tan\theta \tag{2}$$

The output force, F_y, is therefore proportional to PAM force F_a by a ratio of the actuator attachment distance L_{ap} to half the leg length L. However, the changing angle made by the scissoring legs alters the moment arm seen by the PAM, reducing it initially but increasing as the mechanism extends. This helps to offset the sharply decreasing force output of the PAM actuator with contraction. Prediction of x-frame performance is given in Fig. 5b, with an estimated morphing skin stiffness providing the force required curve and 100% extension being the design goal.

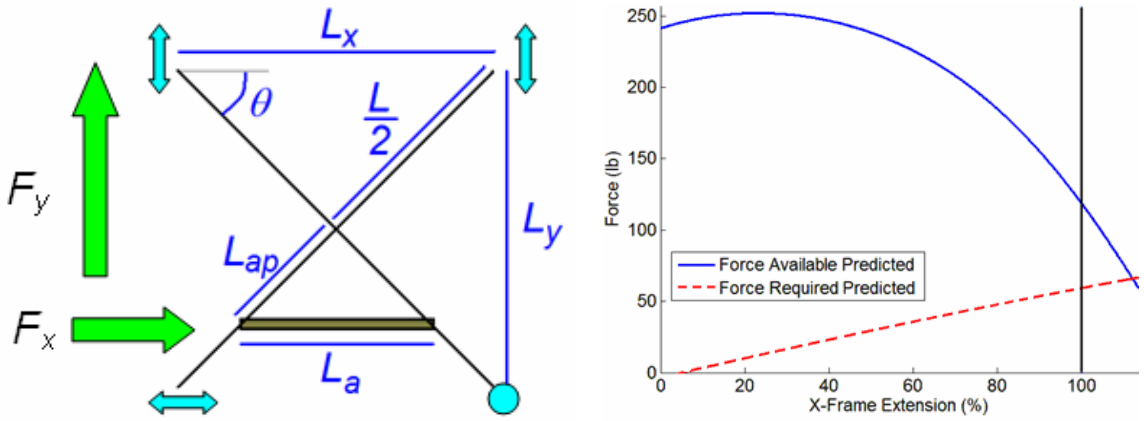

(a) (b)

Fig. 5: X-frame design (a) system geometry; (b) F_y prediction based on x-frame kinematics and empirical PAM actuator data [18].

A test article was fabricated using PAM actuators designed to generate maximum force and displacement within the geometric constraints of the x-frame. Two PAM actuators were used, with $L_{ap}/(L/2) = 1$ to maximize output. Decreasing starting angle of the x-frame legs increases F_y output, but reduces overall displacement. A starting angle of 18^o was chosen, which was predicted to start at 3.5-in and reach 7-in at 100% extension.

Testing was conducted on an MTS machine as shown in Fig. 6, where force versus displacement was characterized with the actuator pressure held constant at 90 psi gauge. Active length L_y was defined as the distance between the pinned ends of the x-frame legs as in Fig. 5a, with zero displacement defined at the starting 18° leg angle. The x-frame mechanism was allowed to extend from zero displacement until the measured force output went to zero and then returned to the start position. Force and displacement were recorded for several cycles and averaged.

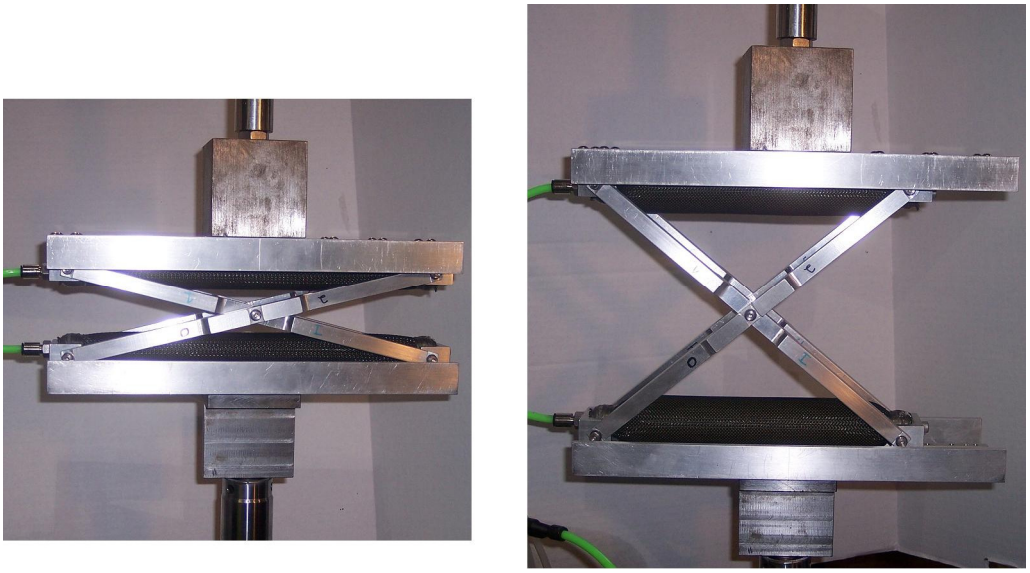

(a) **(b)**

Fig. 6: X-frame testing (a) blocked force; (b) full extension [18].

Results of the MTS testing are provided in Fig. 7 as a dash-dotted green line. The force output prediction, shown as a solid blue line, is based on PAM performance data at 90 psi and x-frame kinematics from Eqns. (1) and (2). Qualitatively, performance predictions matched the experimental results quite well. A decrease in available force is seen due to losses in the mechanism, but sufficient excess force was provided in the design stage that even with losses, the test article is able to exceed the 100% extension goal for the design skin stiffness.

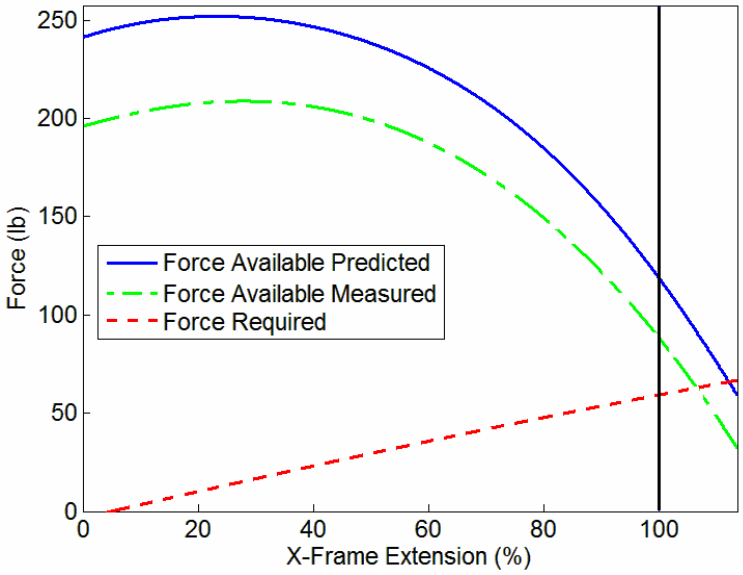

Fig. 7: System performance comparison at 90 psi [18].

1.4 Outline of Thesis and Technical Objectives

In Chapter 2, a control scheme is tested for a PAM actuator system. A 1DOF system is constructed with a single PAM operating against a nonlinear spring, simulating a hypothetical morphing implementation such as that used in the extension morphing actuator described above. A proportional valve is used as the pneumatic control element. A Simulink model of the PAM system is made and validated by comparison with experimental results. This Simulink model is then used to tune a cascaded PI controller capable of tracking displacements at frequencies up to 20 Hz. The objective of this section is to demonstrate the capabilities of simple linear control methods for nonlinear PAM actuation systems with a proportional valve as the control element. The combination of a linear controller with a proportional valve has not previously been demonstrated in the literature.

Chapter 3 focuses on the development of a passive anisotropic elastomer composite skin with potential for use in a 1-D span-morphing UAV wingtip. The extension

morphing actuator described above is mated to an elastomeric skin with anisotropic fiber reinforcement and a bonded high strain honeycomb substructure. The skin is capable of sustaining 100% active strain with negligible major axis Poisson effects, giving a 100% change in surface area, and can withstand typical aerodynamic loads, assumed to range up to 200 psf (9.58 kPa) for a maneuvering flight surface, with minimal out-of-plane deflection. The objective of this section is to advance the state of the art of elastomeric morphing skins by designing a skin specifically for a variable span wing using reinforcement techniques not seen before in the literature for this application.

Chapter 4 contains the conclusions of the thesis and provides suggestions for future work.

Chapter 2

Pneumatic Actuator System Modeling and Control

2.1 Overview

In order to implement a morphing skin powered by a PAM actuator, the shortcomings in the control of PAM systems needed to be addressed. A PAM morphing system would need to track inputs up to at least 5 Hz for flight control, while inputs up to 20-30 Hz or more are desired for higher order control. To achieve this, a separate test stand, the Single PAM Test Apparatus (SPTA) was constructed to characterize the performance of a single PAM under simulated operating conditions. Detailed attention was paid to the design of the pneumatic system providing air to the actuator as the capabilities of the pneumatics determined the performance limits and controllability of the PAM to a great degree. A detailed model of the SPTA was then developed in Simulink to capture the behavior of the PAM system up to 35 Hz and validated by comparison with experimental results. Finally, linear controllers were compared using the Simulink model, and a PID controller was selected for experimental testing. Control gains were chosen using Zeigler-Nichols tuning with acceptable results over a range of frequencies, demonstrating the effectiveness of linear control on PAM actuation systems.

2.2 SPTA Description

The Single PAM Test Apparatus attempted to emulate the operation of a PAM actuator straining a morphing skin in a nonlinear arrangement such as the scissoring frame developed in the previous chapter, but in a generalized fashion. The apparatus,

shown in Fig. 8a, consists primarily of a frame with a cantilevered C-channel aluminum beam attached in an adjustable manner to a vertical 80/20 aluminum post fixed to an 80/20 base. This frame was clamped to a lab table during testing to prevent movement. The PAM actuator is secured at the top to the cantilevered beam by a threaded rod which has an air-through hole to provide pressurized air to the PAM. An Omegadyne PX209-200G5V pressure transducer measures the PAM pressure via an aluminum block which was screws directly onto the threaded air-through rod. The bottom of the PAM is attached to a flat plate shown in Fig. 8b by means of the threaded ends of a Honeywell Sensotech Model 31 1000lb load cell in line with the PAM. To one edge of the plate is bolted the moving end of an Omega LP804-2 LVDT position sensor, the fixed end of which is attached to the cantilevered beam. This sensor measures the motion of the spring plate as the PAM contracts, with contraction regarded as positive by convention.

The plate has eye hooks for four springs arranged in parallel and sized to provide approximately 3% strain in the test PAM at 90 psi (621 kPa). The springs are not loaded beyond their initial steeper spring rate, leading to a two-part piecewise nonlinear spring rate which stands in for the nonlinearity of an actual morphing load. The springs are fixed via four similar eyehooks to the base of the frame. To constrain the system to motion in the vertical axis, a hollow aluminum guide tube was attached to the base between the four springs. A steel rod fixed to the bottom of the spring plate slides in sleeve bearings which line the guide tube, preventing side to side motion of the PAM during operation. Detail of the spring plate/guide rod arrangement is shown in Fig. 8b.

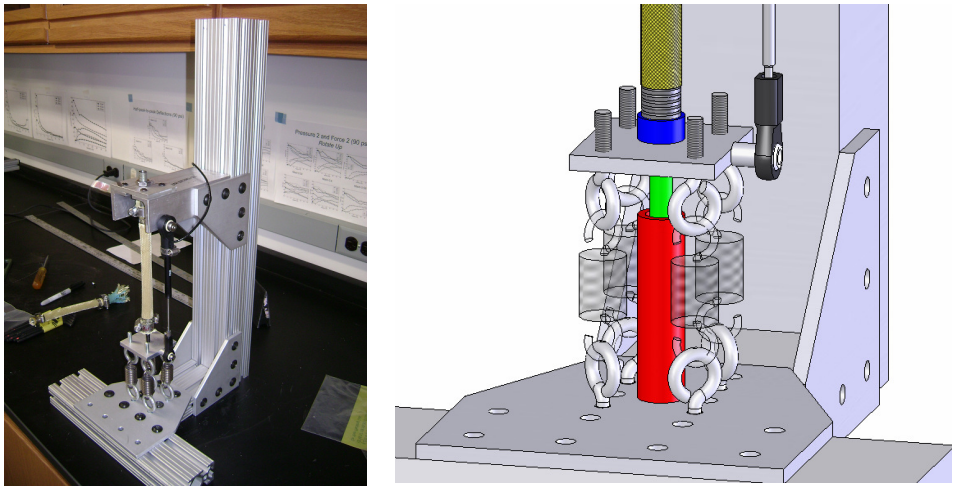

(a) (b)

Fig. 8: Single PAM Test Apparatus (a); detail of spring plate including guide rod (b).

The PAM used for testing on the SPTA was a 0.625” (1.59 cm) nominal outer diameter, 5.15” (13.1 cm) active length PAM with a Kevlar braid at a braid angle of 60.8°. The internal bladder was natural latex tubing with an OD of 0.61” (1.55 cm) and a wall thickness of 0.0625” (0.16 cm). Note that the PAM used on the SPTA is intended to have broad application to different morphing designs.

The pneumatic circuit providing air to the PAM is diagrammed in Fig. 9. Compressed air was supplied by the shop air compressor through about 100 ft of flexible 1” hose connected to a dial regulator. Flexible 3/8” plastic tubing and instant tube fittings were used between all other pneumatic components. Downstream of the regulator, an 18” long section of closed off 4” diameter steel pipe was installed with instant tube fitting connections at both ends to form a 130 cubic inch plenum. During testing, the plenum helped to reduce periodicity in the flow by essentially acting as a capacitor. This was confirmed by measuring pressure immediately after the regulator during step inputs to the PAM, where the plenum reduced the magnitude of upstream pressure transients by approximately 70%.

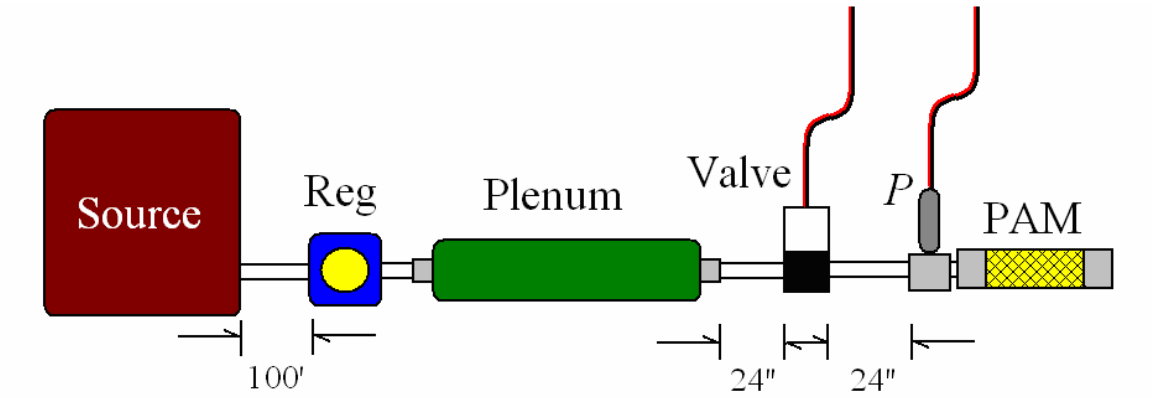

Fig. 9: Pneumatic circuit setup; distances between components less than 3" unless noted.

Flow control was provided by a Festo MPYE-5-1/8HF-010-B, a proportional 5/3-way spool valve. The valve consists of a sliding spool that alternately connects two output ports to either a pressure source or an exhaust port. This allows two actuators to be controlled simultaneously in a bi-directional manner. In this study a single actuator was operated while the second output port was blocked off. The spool position is varied continuously via a solenoid coil. The coil is powered by a 17-30 V excitation and controlled by an analog input signal of 0-10 V. By applying a signal voltage to change the spool position, valve orifice cross-sectional area can be continuously varied, giving control over flow rate to the PAM. The spool valve has a fast response time of 5 ms, and an operating pressure range from 0-10 bar, delivering 700 l/min at a nominal pressure of 6 bar.

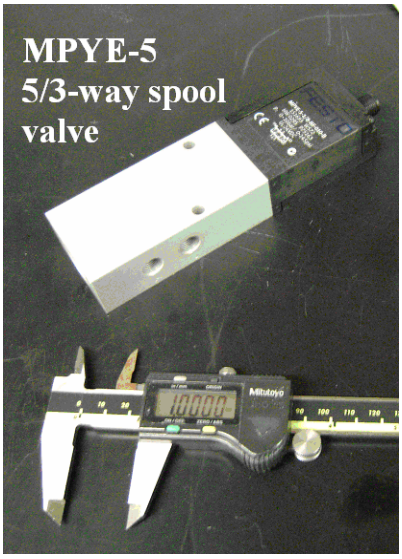

Fig. 10: Festo MPYE-5-1/8HF-010-B proportional 5/3-way spool valve.

Data on SPTA force, pressure, and displacement was acquired for square, triangle, and sinusoidal valve signals at frequencies from 1 to 35 Hz and input pressures of 30, 60, and 90 psi [2, 4, and 6 bar]. This gave a body of experimental data for comparison later when designing a Simulink model of the system. A few typical time histories are presented in Fig. 11 showing the system response to a sine input. Force, displacement, and pressure are given for a 90 psi input pressure with six different valve signal voltage inputs: three different frequencies (1, 7, and 14 Hz), and two different voltage levels corresponding to a moderate flow case (Fig. 11a, c, and e) and a high flow case (Fig. 11b, d, and f).

From these results, the system appears to be highly nonlinear in nature. At lower frequencies, the response to a sine input is nearly a square wave, indicating the presence of an almost infinite number of frequencies in the output. The shape of the output also undergoes a distinct change with frequency and input amplitude, approaching a sine wave at higher frequencies and lower flow rates. The broad spectrum of frequencies present in the response and multiple modes of behavior exhibited are distinct characteristics of nonlinear systems [28].

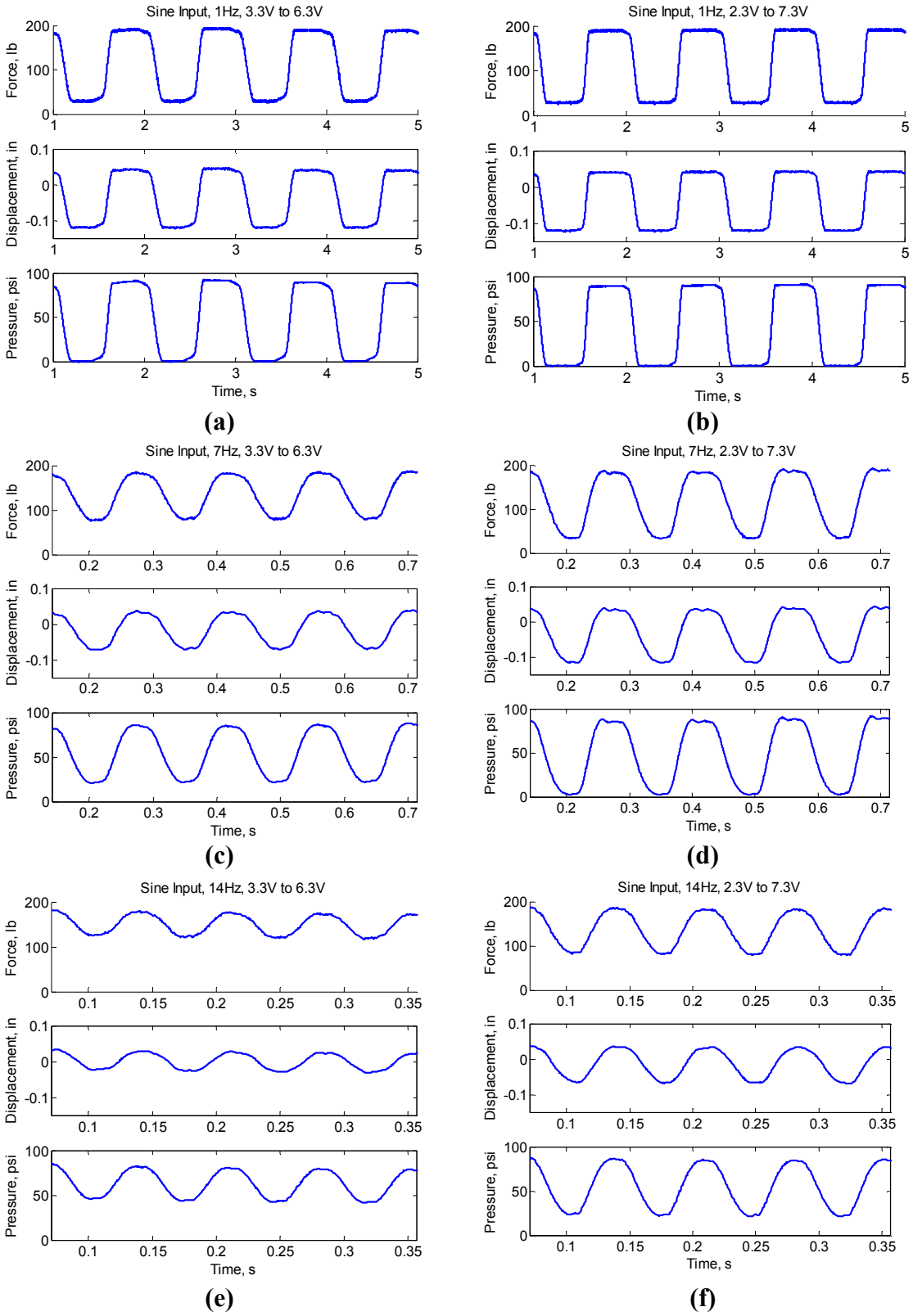

Fig. 11: SPTA force, displacement, and pressure for sine inputs at 1, 7, and 14 Hz and three voltage inputs: moderate flow (a, c, and e) and higher flow (b, d, and f).

2.3 SPTA Model Development and Verification

The first step to developing a controller for the SPTA was to construct a mathematical model of the physical system. Each individual component was described analytically or empirically and incorporated into the model. The model was then implemented in Simulink and validated by comparison with experimental data. The main components of the SPTA model were the mechanical system dynamics, the mass flow through the valve and connecting tubing, the pressure change in the PAM as a result of mass flow, and the force output of the PAM itself based upon pressure and displacement. The equation of motion governing the SPTA dynamics is given by:

$$M\ddot{x} + F_f + F_s = F_p - W \tag{3}$$

where M and W are the mass and weight of the moving parts of the system (spring plate, eye hooks, load cell, position sensor attachment bolt), x is the PAM position, F_p is the PAM force, and F_s is the spring force. The friction force on the guide rod under the spring plate, F_f, was incorporated into a general viscous friction force discussed later.

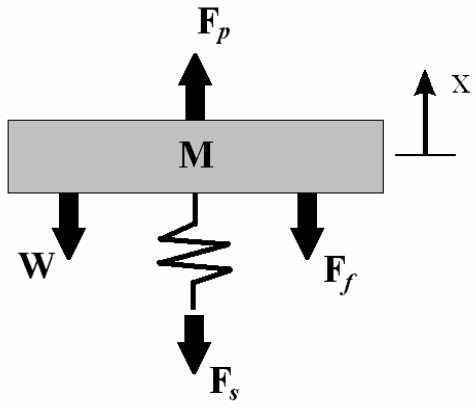

Fig. 12: Free body diagram of spring plate assembly.

2.3.1 PAM Force Model

A review of methods for prediction of PAM force output reveals a number of different models, all of which suffer from large errors or require empirical actuator characterization for accuracy. Most are based on an energy conservation approach, with each model having a similar combination of geometric and experimentally determined parameters relating force to pressure and displacement [25]. In one model for a PAM system controller, Caldwell et al. suggest calculating PAM force based on the driving force generated due to volume change away from the lowest energy state due to braid reorientation at different PAM displacements [19]. This method produces the correct qualitative response but is different from the actual PAM force by up to 50% due to the non-ideal losses. A similar initial approach was taken by Hildebrandt et al. [29] who subsequently modeled the PAM as a pneumatic cylinder with an empirically determined "virtual piston area" to account for non-ideal losses. Another model by van der Linde [30] uses a lumped parameter model that relies on work by Chou and Hannaford [31] for PAM force, with a number of parameters estimated empirically. The model also assumes constant PAM volume, which is not a valid assumption for the larger displacements seen in the research presented here. Kothera et al. [21] improve upon an older model by Gaylord [32] with the addition of a number of further parameters to account for non-cylindrical bladder shape and the nonlinear stiffness when stretched. However, this model still exhibits some error and requires parameter estimation from experiment.

The purpose of this research was control of a morphing control surface and not refinement of PAM actuator models. Thus it was decided to rely on lookup tables based on empirical actuator data, rather than a predictive model, to provide the PAM force term

in Simulink. Underlying this lookup table method is an assumption of quasi-static PAM force. A series of isobaric load lines shown in Fig. 13 were found by holding the SPTA PAM at constant pressure while measuring quasi-static force on an MTS machine over contraction ratios from 0.2 to -0.05. High order polynomials were fit via the least mean squares method to the actuator load lines at each pressure, appearing as thick red lines in Fig. 13. These polynomials were then used to generate a 2-D lookup table giving PAM force based on pressure and displacement, with linear interpolation between entries.

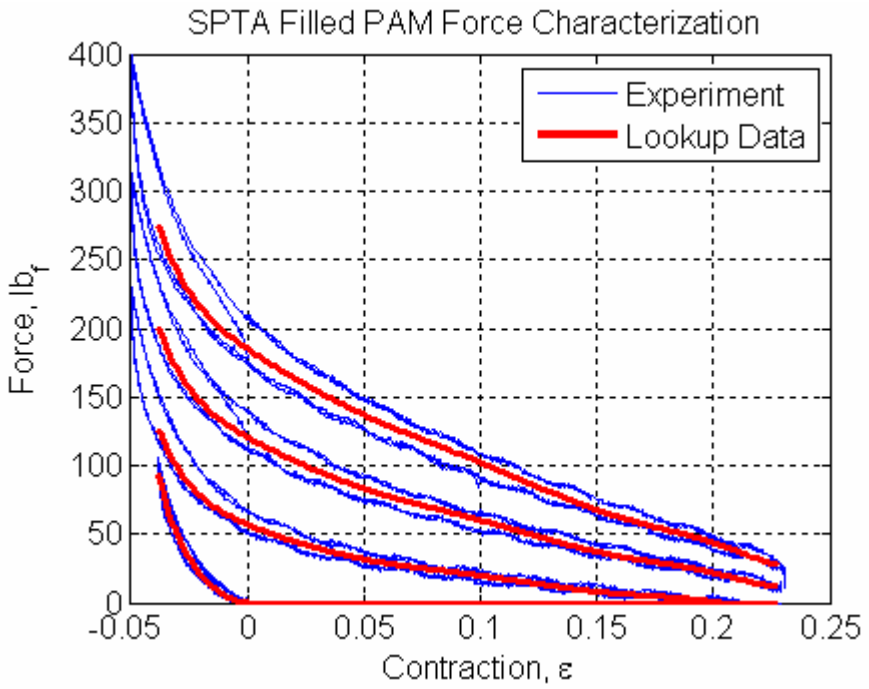

Fig. 13: High order polynomial fits to SPTA PAM data used to generate 2-D lookup table.

Hysteresis was excluded from the PAM force model as Chou and Hannaford [31] show that PAM friction is largely velocity independent and highly dependent on position history. Thus over the modest displacements expected in the model, hysteresis was expected to be small and difficult to predict. For simplification, Chou and Hannaford include a constant hysteresis force of about 5% of maximum blocked force. Using this

approach in the Simulink model was found to negatively affect system stability and simulation results. Instead, a small viscous damping force was introduced to account for friction throughout the system, resulting in a better match with experimental data.

2.3.2 Nonlinear Spring Model

The load on the SPTA was provided by four steel tension coil springs attached in parallel by eye hooks to the bottom of the spring plate. Because the system operated at a very low pretension shared over all four springs, the springs were not loaded into the linear range. Spring force was measured versus displacement on an MTS machine. The results below, Fig. 14a, display typical behavior for a tension spring: an initial steep slope before transitioning to the actual spring constant. Using the same approach applied to the PAM force model, spring force was included in Simulink via a 1-D lookup table. Three polynomials were fit in a piecewise fashion to different sections of the spring force data using the least mean squares method. These polynomials were then used to generate a lookup table which was once again implemented with linear interpolation between entries.

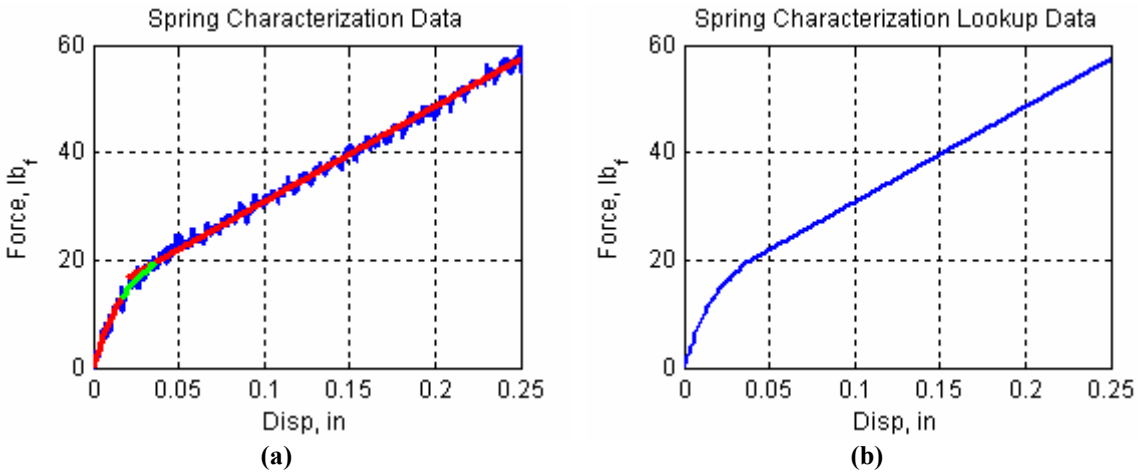

Fig. 14: Spring force characterization (a) piecewise curve fits to experimental data; (b) lookup table data, generated from curve fits.

2.3.3 PAM Pressure Model

To use the PAM force data described above, an accurate model is needed to determine internal pressure based on mass flow into the PAM. Richer and Hurmuzlu [33] derive an expression for pressure change in a container of changing volume using the ideal gas law, conservation of mass, and conservation of energy:

$$\dot{P} = \frac{RT}{V}\left(\alpha_{in}\dot{m}_{in} - \alpha_{out}\dot{m}_{out}\right) - \alpha P\frac{\dot{V}}{V} \tag{4}$$

Here R is the gas constant for the medium, T is the upstream temperature, V is the actuator volume, and the α coefficients are specific heat ratios for the different processes. According to work by Al-Ibrahim and Otis [34] on pneumatic cylinders as related by Richer and Hurmuzlu, the pressure change is approximately adiabatic only during inflow, where the specific heat coefficient can be estimated as α_{in} = 1.4. During exhaust the process was nearly isothermal and the specific heat α_{out} = 1 is appropriate. For pressure change due to changing volume the process is somewhere between adiabatic and isothermal and the specific heat can be approximated as α = 1.2.

Unlike a pneumatic cylinder, the internal volume of a PAM is difficult to determine during operation. While a pneumatic cylinder's volume can be calculated based upon its geometry and cylinder position, the bladder and braid of a PAM will change shape nonlinearly when inflated. For a PAM with a very stiff braid material, the geometry of the braid will limit the expansion of the bladder and should lead to a volume change which is not dependent on pressure. As the braid angle changes, the PAM expands radially and contracts axially, leading to a nonlinear relationship between displacement and volume when pressurized.

To measure this relationship, a volume measurement device was attached to the MTS machine used to characterize PAMs. The device, shown in Fig. 15, consists of a water-filled tube surrounding the PAM, with an observation tube connected by a flexible hose to the side of the main tube. The water level in the observation tube is measured by a laser position sensor. The PAM is then pressurized and quasi-static change in water height is recorded versus contraction ratio. Based upon the cross section of the two tubes, the change in volume from rest can be determined. The braid and rubber bladder are essentially incompressible and occupy constant volume during testing. The resting volume of the PAM bladder, calculated based on geometry, is then added to the change in volume to yield the total internal volume versus pressure and displacement.

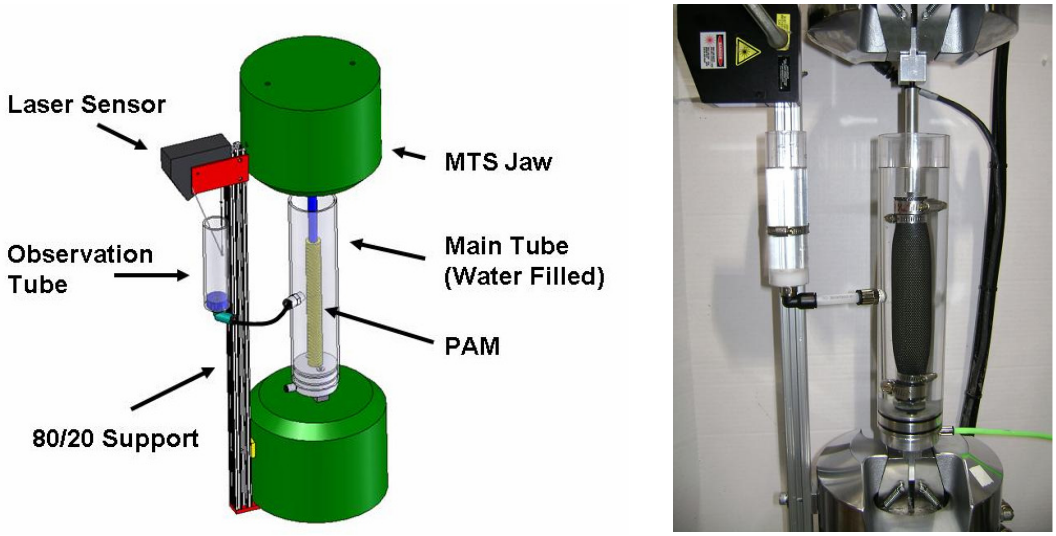

Fig. 15: PAM volume measurement device (a) design; (b) fabricated assembly.

Results from volume characterization of the SPTA PAM are plotted below in Fig. 15. Each curve is a high order polynomial fit via the linear least squares method to a curve of constant pressure. Except below about 10 psi where the PAM does not seem to inflate to its full shape, the internal volume is largely dictated by braid geometry at a given

displacement. There is a slight dependence on pressure above 10 psi, which suggests that rubber stiffness, friction between braid and rubber or within the braid itself, or even strain in the braid help dictate the volume that can be achieved for a given pressure. The polynomials plotted in Fig. 15 were used to generate data points for a 2-D lookup table.

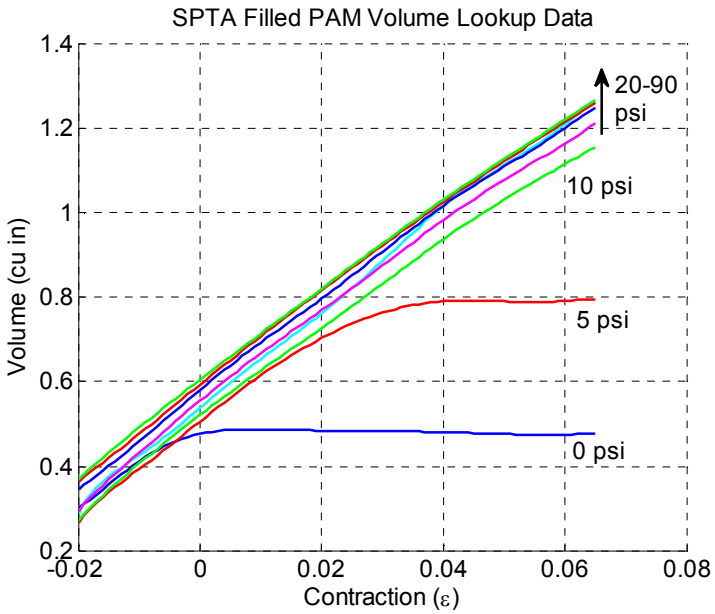

Fig. 16: Volume measurement device for SPTA PAM showing six different pressures.

2.3.4 Mass Flow through Valve Orifice

Accurately predicting mass flow is both important and difficult for a pneumatic system. The effects of compressibility and losses throughout the system will affect performance and should be included in a pneumatic mass flow model. The following equation predicts steady mass flow through a well-rounded orifice [35], but has also been found useful for dynamic flow [36]:

$$\dot{m} = \begin{cases} A \cdot C_d \cdot P_u \cdot C_1 \sqrt{2/(R \cdot T)} & \text{for } P_d / P_u > P_{cr} \\ A \cdot C_d \cdot P_u \cdot C_2 \sqrt{2/(R \cdot T)} & \text{for } P_d / P_u \le P_{cr} \end{cases} \tag{5}$$

Here, A is the valve orifice area, P_u and P_d are the absolute pressures upstream and downstream of the valve, R is the gas constant for the medium, and T is the temperature upstream of the valve (taken to be room temperature). The terms C_1 and C_2 are pressure and medium dependent flow terms for subsonic and sonic flow respectively:

$$C_1 = \sqrt{\gamma/(\gamma-1)\left[\left(P_d/P_u\right)^{2/\gamma} - \left(P_d/P_u\right)^{(\gamma+1)/\gamma}\right]}$$
$$C_2 = \left(2/(\gamma+1)\right)^{1/(\gamma-1)}\sqrt{\gamma/(\gamma+1)} \tag{6}$$

The term C_d is a discharge coefficient, capturing losses in the orifice, which is considered independent of valve position or signal voltage. Pugi et al. [37] give an expression which approximates C_d for compressible flow based on the ratio of downstream to upstream pressure:

$$C_d = 0.8414 - 0.1001\left(P_d/P_u\right) + 0.8415\left(P_d/P_u\right)^2 - 3.9\left(P_d/P_u\right)^3 \ldots$$
$$\ldots + 4.001\left(P_d/P_u\right)^4 - 1.6827\left(P_d/P_u\right)^5 \tag{7}$$

With this, all terms required to find mass flow can be calculated except for valve cross sectional area, which must be found through valve characterization. Losses due to neglecting tubing should also be included in a mass flow model and will be discussed later.

2.3.5 Valve Area Characterization

In order to use the Festo MPYE 5/3-way proportional valve to control PAM position, the cross sectional area of the valve orifice must be quantified as a function of input voltage. Based on knowledge of mass flow rate, Eq. (5) can be solved for valve orifice area. To experimentally measure dynamic mass flow rate, the valve was used to fill and

exhaust a fixed volume container. Flow rate was then estimated based upon the pressure history and used to characterize valve area versus voltage. The small steel pressure vessel shown in Fig. 17 was constructed for this purpose, with a volume of approximately 15 cu. in., an input port on one end, and a pressure transducer on the other.

Fig. 17: Steel pressure vessel for spool valve characterization.

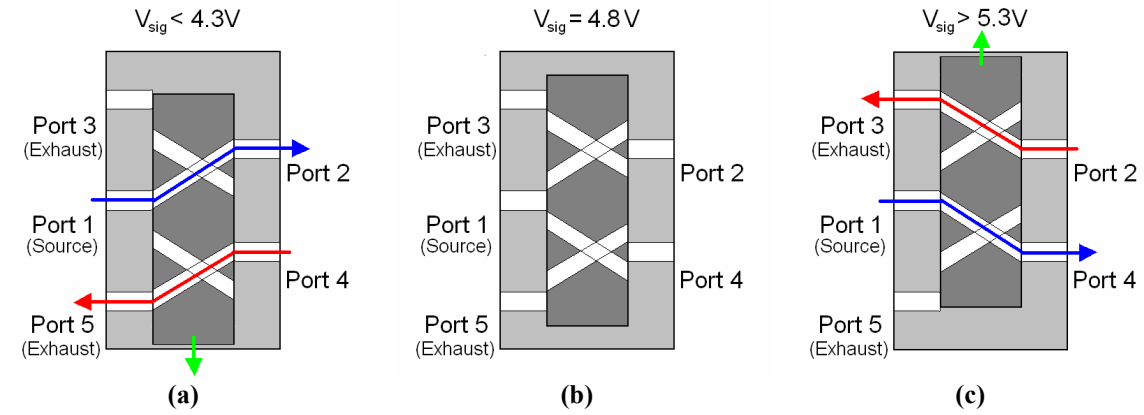

Fig. 18: 5/3-way spool valve operation (a) port 2 open to source; (b) neutral; (c) port 4 open to source.

The Festo MPYE 5/3-way proportional valve has five ports numbered 1-5 as shown in Fig. 18 with a sliding spool in the center determining which ports are connected. At an input signal of 4.8 V, the valve spool is centered such that nominally no flow occurs (although there is slight leakage), and between 4.3 and 5.3 V there is a deadband region with very low leakage flow. At voltages lower than 4.3 V, port 2 is connected to the

source pressure and port 4 is open to atmosphere, while at voltages above 5.3 V port 4 is open to source pressure while port 2 is connected to atmosphere. Flow rate for both inflow and exhaust is related to the difference of the signal voltage from the neutral voltage.

A series of tests were conducted to characterize the inflow and exhaust flow rates for each of the two output ports using a 90 psi source pressure. The pressure vessel was connected to one of two output ports, either port 2 or port 4, by a very short length of 3/8" tubing so that the impact of connecting tubing losses on flow rate could be neglected. The unused output port was blocked during characterization. To measure inflow into the vessel, the valve was cycled at a low frequency between the fully opened exhaust voltage and a range of inflow signal voltages from 0 V to 4.8 V for port 2 and 4.8 V to 10 V for port 4. A similar series of tests was run to acquire exhaust data. The valve was cycled between fully open to input pressure and a range of exhaust signal voltages, going from 4.8 V to 10 V for port 2 and 0 V to 4.8 V for port 4. The inflow or exhaust regions of the pressure histories were used to find the time rate of change pressure, from which mass flow rate and then valve cross sectional area could be determined.

To determine mass flow rate from pressure history, examine Eq. (5). For $P_d / P_u \leq P_{cr}$, flow is choked, and for a given valve area mass flow is linear with upstream pressure P_u. Theoretically for air the critical downstream/upstream pressure ratio is 0.528. However, the critical pressure ratio for a specific valve will vary due to geometry and losses in the valve. Proportional valves can have critical pressure ratios as low as 0 [35], with data for one model ranging between 0.3 and 0.5 [38]. Due to the difficulty of measuring the critical pressure ratio, a value of 0.3 was chosen for normal inflow and exhaust and 0.1

was chosen for the deadband "leak flow" region based on visual approximation from the data. By considering only choked flow, the mass flow equation is simplified to:

$$\dot{m} = A \cdot C_{\mathrm{d}} \cdot C_2 \sqrt{2/(RT)} \cdot P_u \tag{8}$$

This expression for mass flow can be substituted into the pressure change Eq. (4) and simplified for a fixed volume cylinder:

$$\dot{P} = \frac{RT}{V} \alpha \cdot A \cdot C_{\mathrm{d}} \cdot C_2 \sqrt{2/(RT)} \cdot P_u \tag{9}$$

All terms in the above equation are constant except for A. Therefore, finding the slope of the pressure history in the choked flow regime allows A to be calculated for a given signal voltage. For each time history acquired as described above, a least squares linear regression was applied to the choked flow portion of the data and averaged over multiple step inputs. Fig. 19a below gives an example of the method for a 4.2 V to 10 V square wave signal with the results of the linear fit shown as a dotted line.

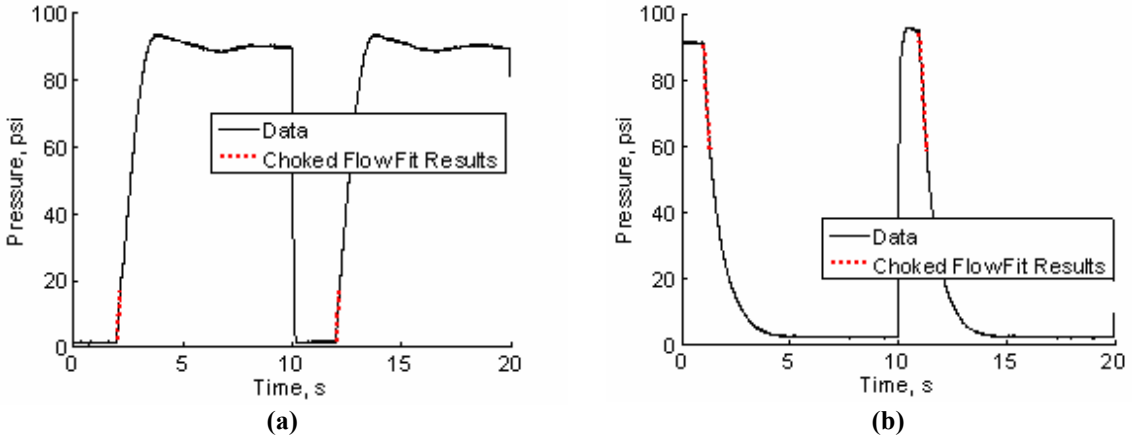

Fig. 19: Port 2 flow characterization showing pressure prediction based on valve area fit results (a) inflow at 4.2 V; (b) exhaust at 5.4 V.

Exhaust occurs through a separate channel in the valve from inflow and thus requires separate characterization. A similar method can be followed to find the exhaust area, but now the upstream pressure, i.e. pressure in the chamber, is no longer constant. An expression is needed for upstream pressure versus time. Taking the Laplace transform of Eq. (9) and rearranging, with $\alpha = 1$ for exhaust flow, yields:

$$P_u(s) = \frac{P_u(0)}{s + \frac{RT}{V} A \cdot C_\mathrm{d} \cdot C_2 \sqrt{2/(RT)}} \tag{10}$$

The inverse Laplace yields an expression for upstream pressure as a function of time:

$$P_u(t) = P_u(0) \cdot e^{\frac{RT}{V} A \cdot C_\mathrm{d} \cdot C_2 \sqrt{2/(RT)} \cdot t} \tag{11}$$

This expression can be used to solve for A based on experimental data. Rearranging, a linear least squares fit for A can be found:

$$\left(RT/V \cdot C_\mathrm{d} \cdot C_2 \sqrt{2/(RT)} \right)^{-1} \log\left(P_u / P_u(0) \right) = A \cdot t \tag{12}$$

By applying the above equation to the pressure data in the choked flow region, it is possible to find a value for valve area for exhaust flow. Using this valve area, predictions from Eq. (11) match the pressure history as demonstrated in Fig. 19b.

By applying the above two methods to inflow and exhaust data, the valve area can be characterized versus signal voltage for both output ports. Results of this characterization for both ports are given in Fig. 20. Incorporating the characterization data into the

Simulink model was a simple matter of importing the valve area versus signal voltage data into two 1-D lookup tables, one for each port.

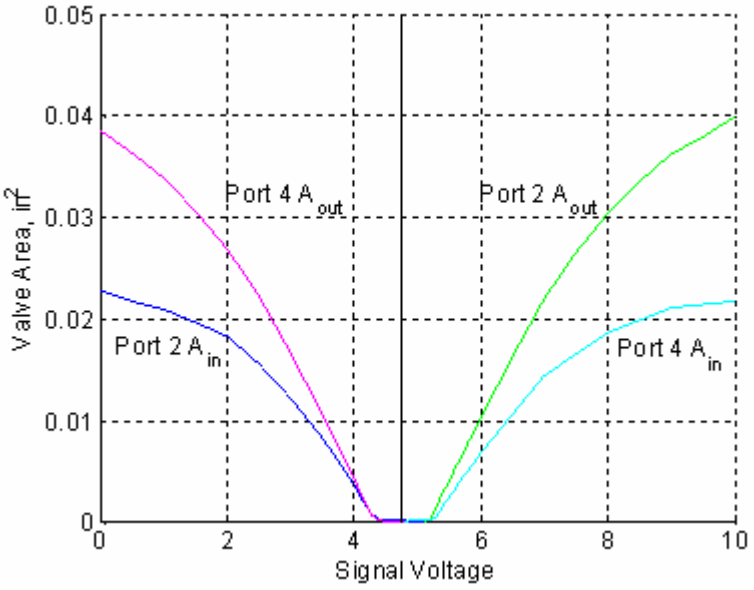

Fig. 20: Festo MPYE 5/3-way spool valve characterization results.

2.3.6 Effects of Connecting Tubing

Two different models were used to include the effects of tubing losses on mass flow for the connecting tubing between the valve and the cylinder. Richer and Hurmuzlu [33] model the tubing losses in two parts. By assuming a change in mass flow to propagate as a wave with no dispersion along a short length of smooth tubing, they find a time delay and amplitude attenuation. The time delay is determined simply by the length of connecting tubing L_t divided by the speed of sound c, and is modeled as follows:

$$\dot{m}_{delay}(t) = \begin{cases} 0 & \text{if } t < L_t / c \\ \dot{m}(t - L_t / c) & \text{if } t \geq L_t / c \end{cases} \tag{13}$$

For the amplitude attenuation due to friction, they multiply the mass flow by the following expression:

$$\phi = \exp\left(\frac{-R_t RT}{2P_d}\frac{L_t}{c}\right) \tag{14}$$

Here, R_t is the tube resistance, L_t is the length of tubing between valve and actuator, and c is the speed of sound in the fluid. The pressure P_d is called the "end pressure" in their text and it is assumed this refers to the pressure at the end of the tubing, the downstream pressure. To simplify the model, fully laminar flow was assumed to determine the tube resistance based on $R_t = 32\mu/D_t^2$, where μ is the fluid viscosity and D_t is the tubing internal diameter.

A second model as derived by Incropera and DeWitt [39] based on Poiseuille flow gives the pressure drop required to sustain steady, fully developed internal flow. As an approximation, this can be used to determine the pressure drop ΔP over the length of connecting tubing between the valve and the volume to be filled:

$$\Delta P = f\frac{\rho u_m^{\,2}}{2D_t}L_t \tag{15}$$

To make use of this equation, three further pieces of information must be calculated. First, the air density ρ is approximated by the ideal gas law using ambient air temperature and the average of upstream and downstream pressure. Second, the mean velocity u_m is estimated based on the air density, the mass flow as calculated by an initial guess without tubing losses, and the cross-sectional area of the tubing. Last, the Moody friction factor f for laminar flow can be calculated in one of two ways. First, for fully laminar flow [39]:

$$f = \frac{64}{\mathrm{Re}_D} \tag{16}$$

The Reynolds number Re_D is based on the mean velocity and the internal diameter of the tubing. For turbulent flow, one method of approximating the friction factor is given by [39]:

$$f = \begin{cases} 0.316\,\mathrm{Re}_D^{-1/4} & \text{for } \mathrm{Re}_D \le 2\times10^4 \\ 0.184\,\mathrm{Re}_D^{-1/5} & \text{for } \mathrm{Re}_D > 2\times10^4 \end{cases} \tag{17}$$

The resulting pressure change from Eq. (15) can then be applied to the upstream or downstream pressure depending on the flow direction. For flow entering the chamber, the pressure is seen by the valve as a back pressure, and ΔP is added to the downstream pressure. For exhaust flow, the pressure drop in the connecting tubing results in a head loss upstream of the valve, and ΔP is subtracted from the upstream pressure. The new upstream and downstream pressure is then used to calculate a new mass flow. This must be iterated until the previous mass flow used to find mean velocity and the new mass flow based on the updated pressures converge.

2.3.7 Pneumatic Model in Simulink

To test the mass flow model and compare the two methods of calculating tubing losses, a Simulink model was made to simulate the filling and exhausting of a fixed volume pressure vessel identical to the one used while characterizing the Festo spool valve. The block diagram of the fixed volume pneumatic model is shown in Fig. 21. A signal voltage is used to determine spool valve area from the Fig. 20 lookup table data in the block labeled “Valve A”. The valve area is then passed to the “Orifice Flow” block containing Eq. (5), where the valve area and current PAM pressure are used to calculate mass flow through the valve.

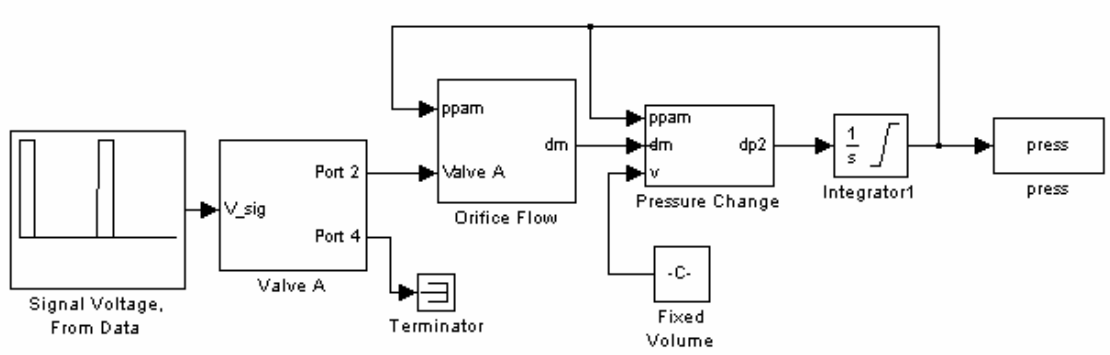

Fig. 21: Fixed volume Simulink pneumatic model.

There are two different versions of the fixed volume pneumatic model compared here; these are referred to as "fv7" and "fv13". In model "fv7", mass flow is multiplied by the Richer-Hurmuzlu loss term Φ from Eq. (14) to include the effects of tubing losses. In model "fv13", the pressure drop term ΔP from Eq. (15) is iterated within the mass flow block at each time step to determine a final mass flow including tubing losses. Model "fv13" assumes turbulent inflow and laminar exhaust flow to best match experimental data. In both model versions, a transport delay function is applied to the mass flow to add a time delay $\tau = L_t/c$ as in Eq. (13). The mass flow is then passed to the "Pressure Change" block, where Eq. (4) is used to determine the change in internal pressure in the chamber. This pressure change is then integrated and output as the chamber pressure.

The fixed volume models were compared with experimental data for two different tubing lengths using triangle, sine, and square wave signal voltage inputs to fill and exhaust a volume equal to the small steel cylinder used during valve characterization. In Fig. 22 through Fig. 24, time histories are presented using 4" of connecting tubing at 1 Hz and 7 Hz signal frequencies. The magnitude of the valve signal voltage was changed to achieve a range of flow rates. Both the lowest and highest flow rates tested at 1 Hz are presented as well.

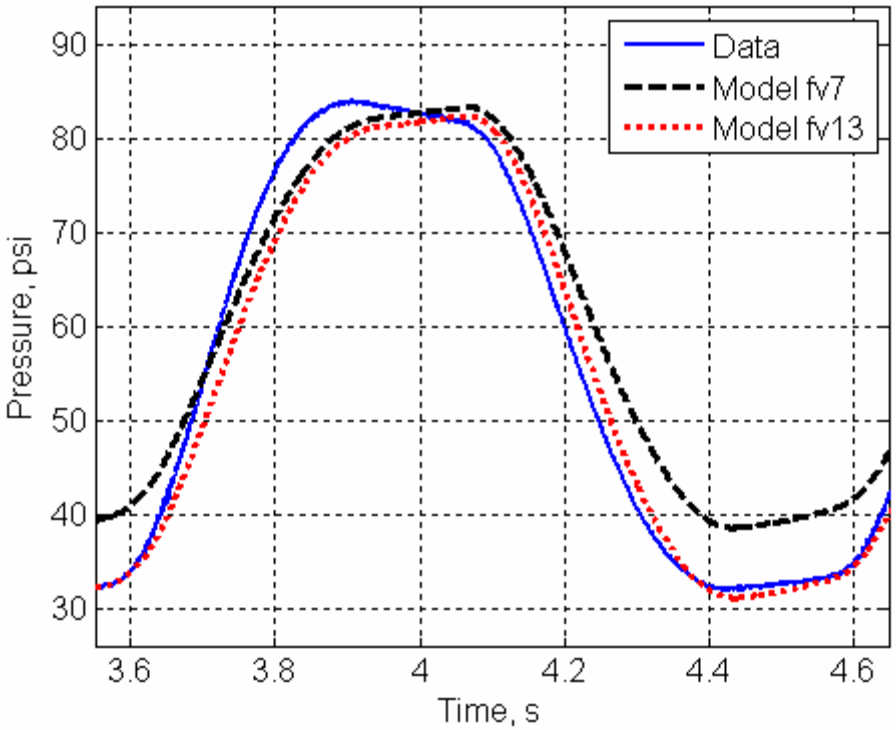

Fig. 22: Tubing loss model comparison, 4" tubing, 1 Hz, low flow.

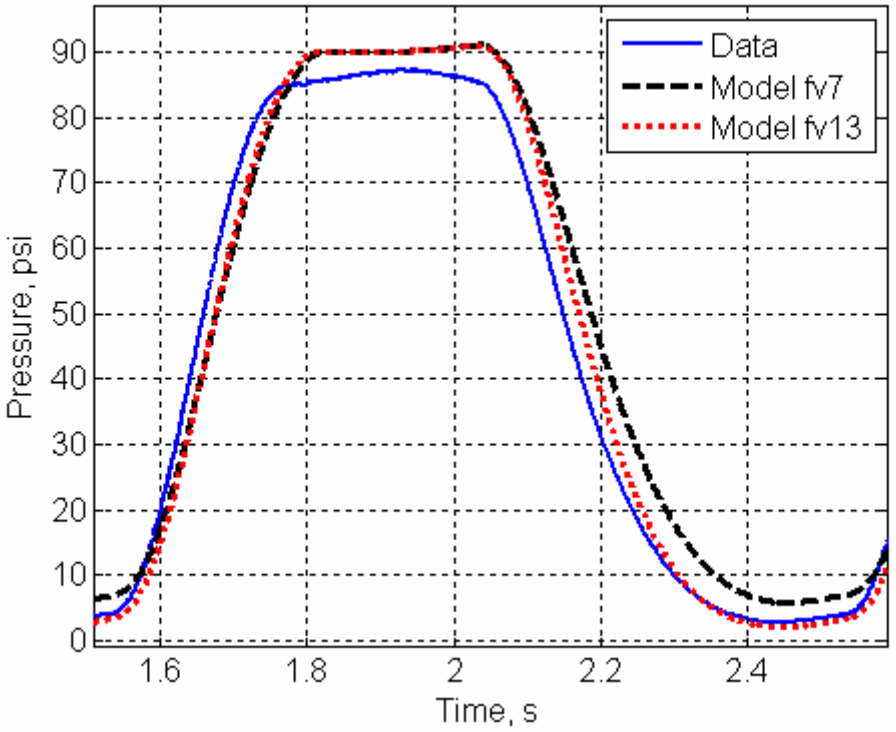

Fig. 23: Tubing loss model comparison, 4" tubing, 1 Hz, high flow.

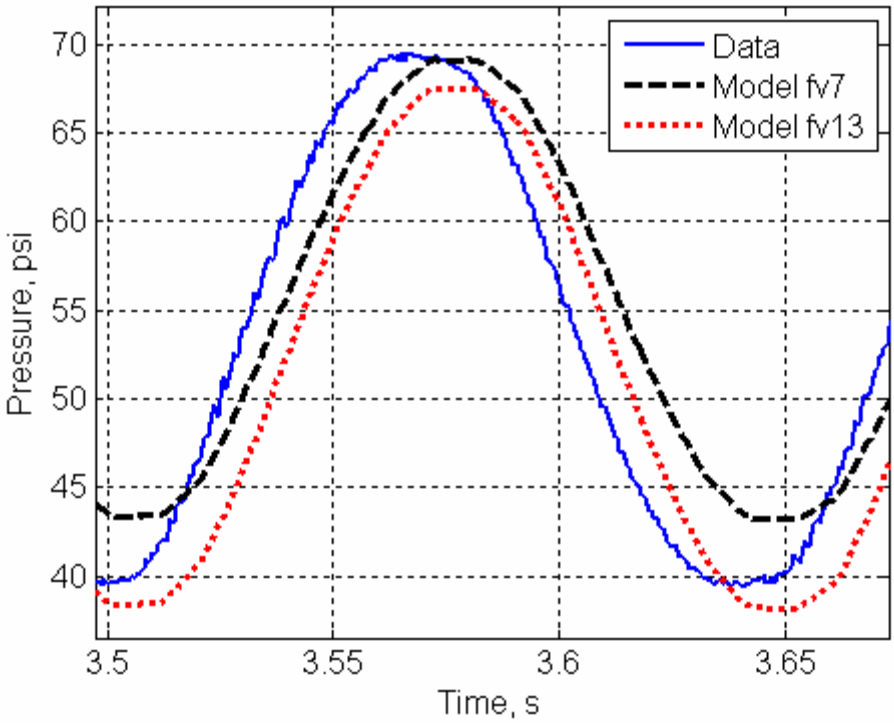

Fig. 24: Tubing loss model comparison, 4" tubing, 7 Hz, high flow.

The models both match the data best at higher flow rates and lower frequencies as seen in Fig. 23, but still exhibit less than about 10% error at low flow rates and/or high frequencies as in Fig. 22 and Fig. 24. In general, neither model appears significantly better at matching experimental data. This result is expected since the tubing loss has little impact when tubing length is short. As a result they both exhibit small discrepancies in flow rate which appear as different rates of pressure change during inflow and exhaust.

Next both models are compared using data taken with 24" of connecting tubing between valve and cylinder. In Fig. 25 and Fig. 26, results for 1 Hz at low and high flow rates are compared, while in Fig. 27, a 7 Hz high flow result is shown. Results vary wildly between models, with model "fv13" using the ΔP loss term from Eq. (15) matching the data well under all conditions, and model "fv7" using the Φ loss term from Eq. (14) filling and exhausting far too slowly.

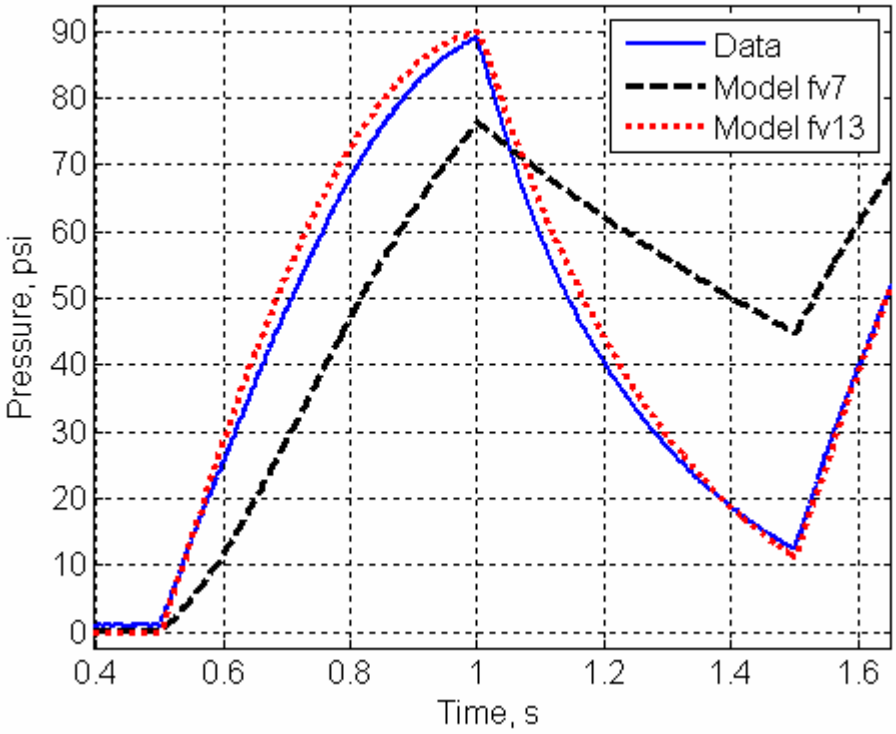

Fig. 25: Tubing loss model comparison, 24" tubing, 1 Hz, low flow.

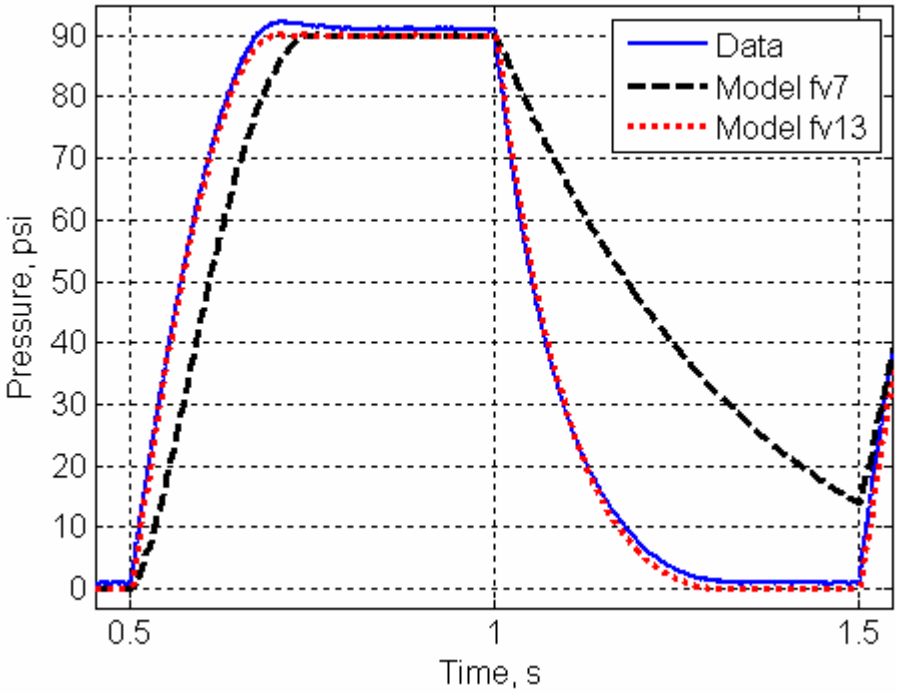

Fig. 26: Tubing loss model comparison, 24" tubing, 1 Hz, high flow.

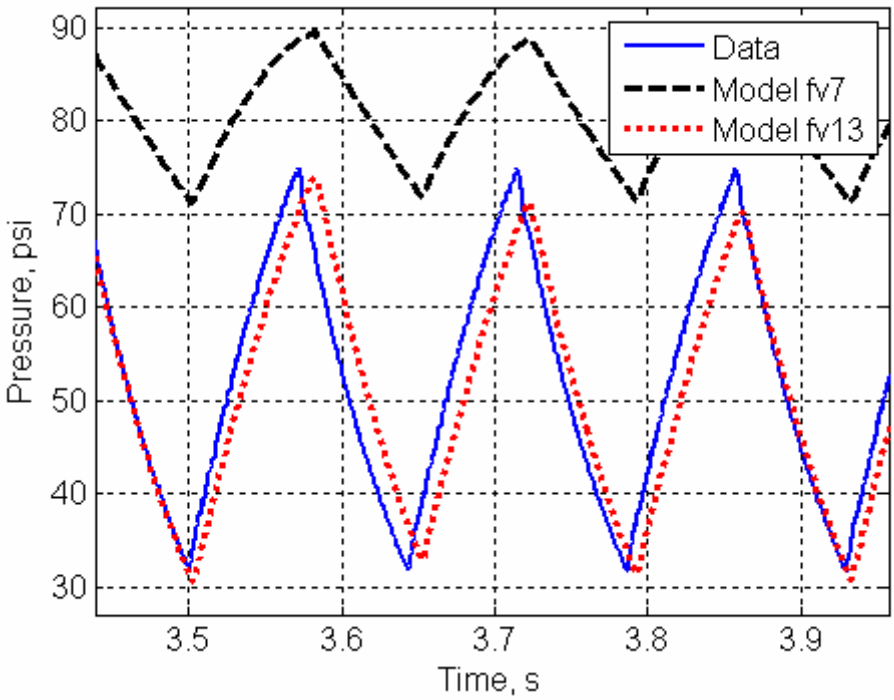

Fig. 27: Tubing loss model comparison, 24" tubing, 7 Hz, high flow.

Based on the results of the fixed volume pneumatic model testing, it is clear that the Richer and Hurmuzlu term for tubing losses as described in their paper and presented in Eq. (14) inadequately represents measured behavior. The ΔP loss term from Eq. (15) is based on a well-known hydrodynamic internal flow pressure drop equation and, when iterated at each time step, appears to give a much better estimate of tubing losses.

2.3.8 Full SPTA Model in Simulink

The pneumatic model, the system dynamics, and the various component characterizations were incorporated into a Simulink model of the complete SPTA system, a diagram of which is presented in Fig. 28. As in the pneumatic model, a signal voltage is used to determine valve orifice area from a lookup table. Based on the valve area and the system velocity and displacement, the PAM states can be calculated and the PAM output force, F_p, determined. The system displacement is also used to find spring force, F_s, from

a lookup table. From the system dynamics, the forces on the system are summed and new system velocity and position are determined.

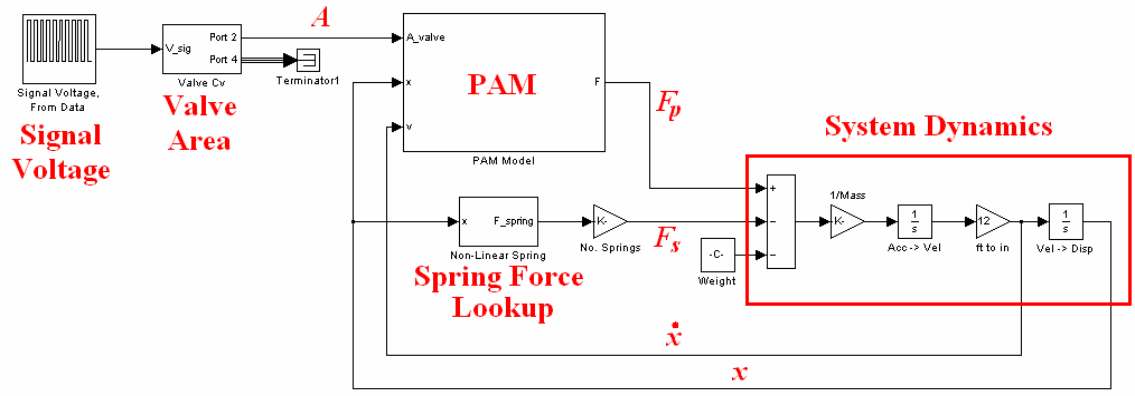

Fig. 28: Full SPTA System Simulink model.

Within the PAM block in Fig. 28, there are two main subroutines: the orifice mass flow block and the PAM force model itself, shown in Fig. 29. The orifice mass flow block uses the flow model from "fv13" based on Eqns. (5) and (15), and calculates mass flow into or out of the PAM based on the valve cross sectional area, supply pressure, atmospheric pressure, current PAM internal pressure, and connecting tubing properties.

Unlike the fixed volume pneumatic model, the best match to the experimental data was achieved by assuming turbulent flow for both inflow and exhaust, using Eq. (17) for the friction factor. Recall that the fixed volume pneumatic model assumed laminar exhaust flow and achieved good agreement with data. It is possible that during SPTA testing, the inclusion of a pressure transducer mounting block with a rough internal surface near the PAM orifice triggers turbulent flow during the exhaust phase, while during fixed volume testing the pressure transducer was mounted to the rear of the pressure vessel, where it did not impact the formation of laminar flow exiting the vessel.

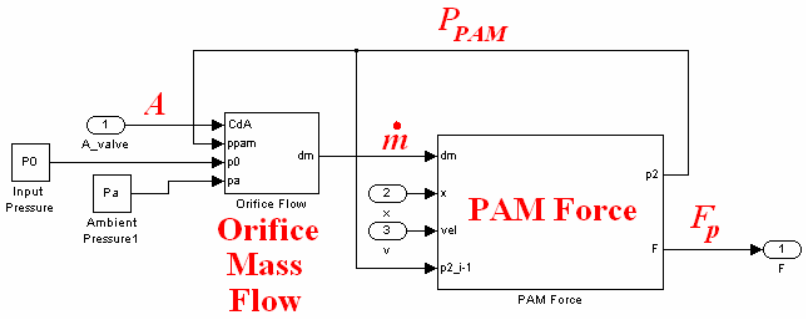

Fig. 29: PAM block showing orifice flow block and PAM force block.

Subsequently, calculation of the PAM states can be carried out inside the PAM force block, details of which are shown in Fig. 30. The following sequence of steps is carried out to determine the PAM internal pressure and ultimately the PAM force. First, based on the position and current internal pressure, the PAM volume is found from the volume lookup table. Internal volume of connecting tubing between valve and PAM is added to find total volume. The total volume, current internal pressure, and mass flow are then used to find the rate change in internal pressure from Eq. (4), which is integrated to find the new internal pressure. The system position and new internal pressure are then used to find the PAM force from a lookup table. A small amount of viscous damping is included to better match the system experimental behavior.

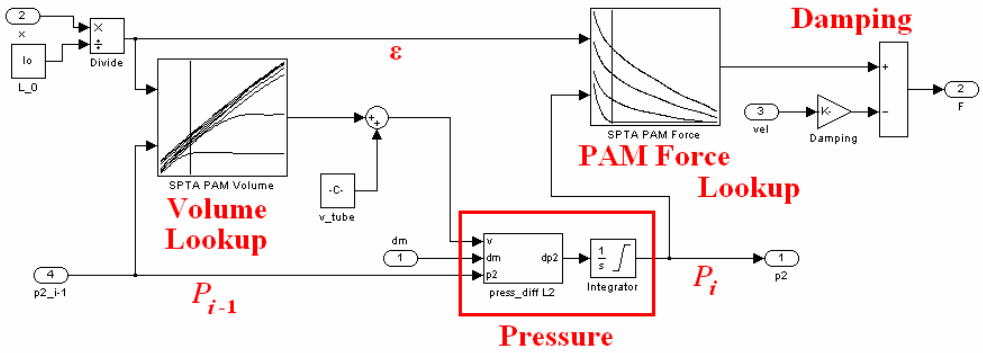

Fig. 30: PAM Force block, where volume, pressure, and then output force are found.

To validate the SPTA Simulink model, predictions were compared with experimental data gathered on the SPTA. Square, triangle, and sine inputs over three different frequencies and flow rates were tested, with sine input results reproduced here. Low and high flow cases are shown at 1 Hz in Fig. 31, at 7 Hz in Fig. 32, and at 14 Hz in Fig. 33.

Agreement between experiment and model is qualitatively good. However, model agreement appears better at higher flow rates for a given frequency. Comparing the rate change of pressure between flow cases at each frequency, there is enough relative error in the flow rate in Fig. 32a and Fig. 33a to introduce a noticeable pressure offset as the PAM model finds a different equilibrium pressure. Second, model accuracy suffers with increasing frequency. Not only is there an increased pressure offset at lower flow rate in Fig. 33a, but there is slight phase lag in Fig. 33b. Finally, in all test cases, it appears that the model inflow and exhaust mass flow rates are higher than observed experimentally, with exhaust flow showing greater error than inflow.

In light of the good performance demonstrated by the fixed volume Simulink model, some aspect or aspects introduced by the SPTA are likely to blame. Inaccuracies in the PAM volume model are one possible source. Another possibility is underprediction of the effect of the SPTA pressure transducer mounting block on tubing losses. As it was previously said, it is believed the rough surface of the pressure transducer mounting block is responsible for tripping turbulent flow during exhaust; however it is possible that the block not only causes turbulent flow during exhaust but increases friction during inflow and exhaust in a manner that this simple loss model does not take into account.

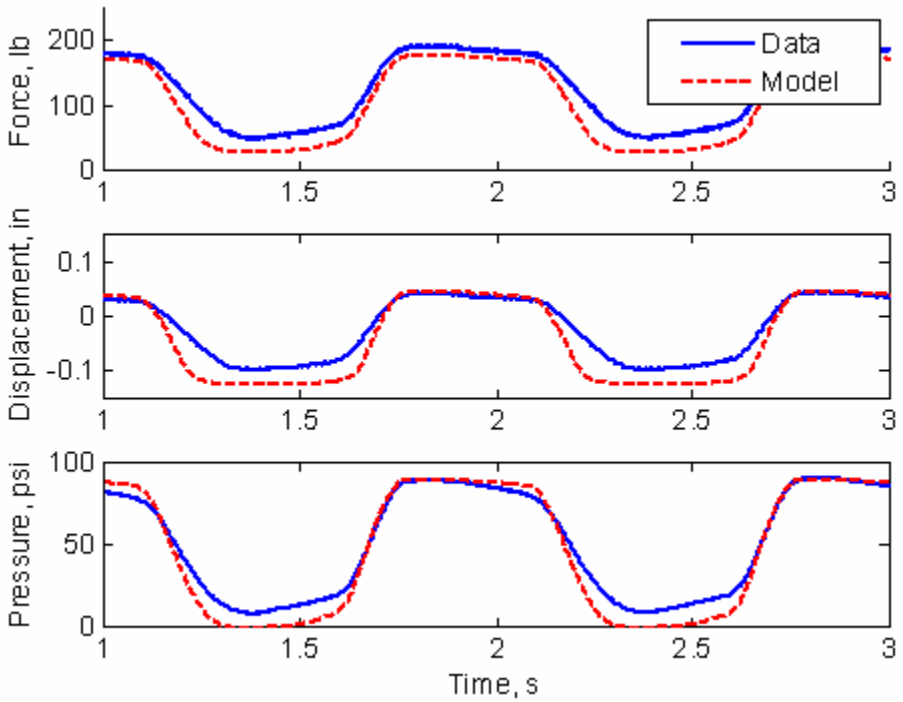

(a)

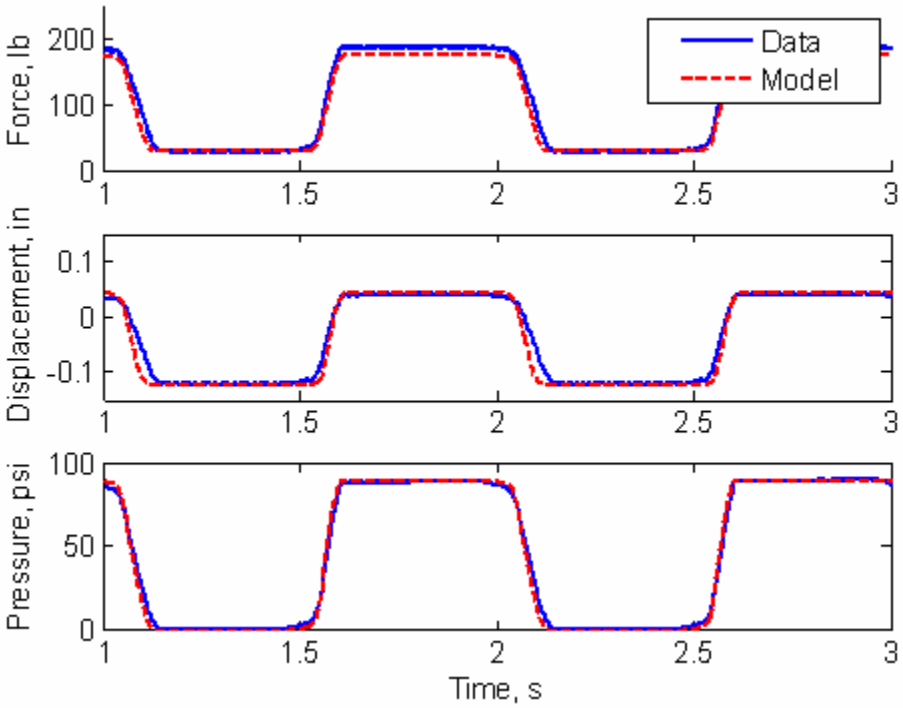

(b)

Fig. 31: SPTA model comparison, 1 Hz sine input (a) low flow; (b) high flow.

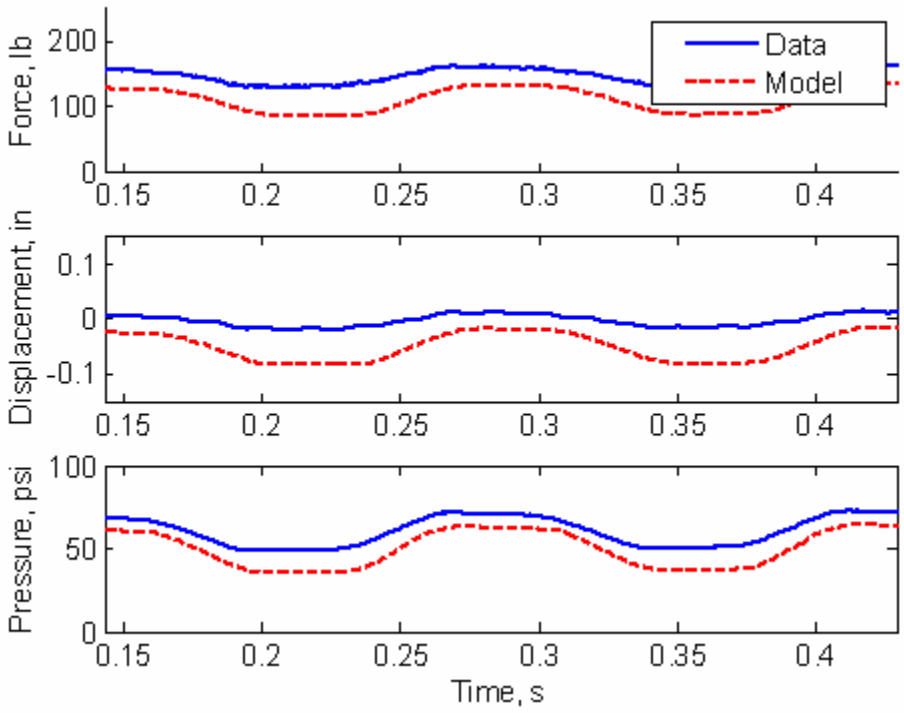

(a)

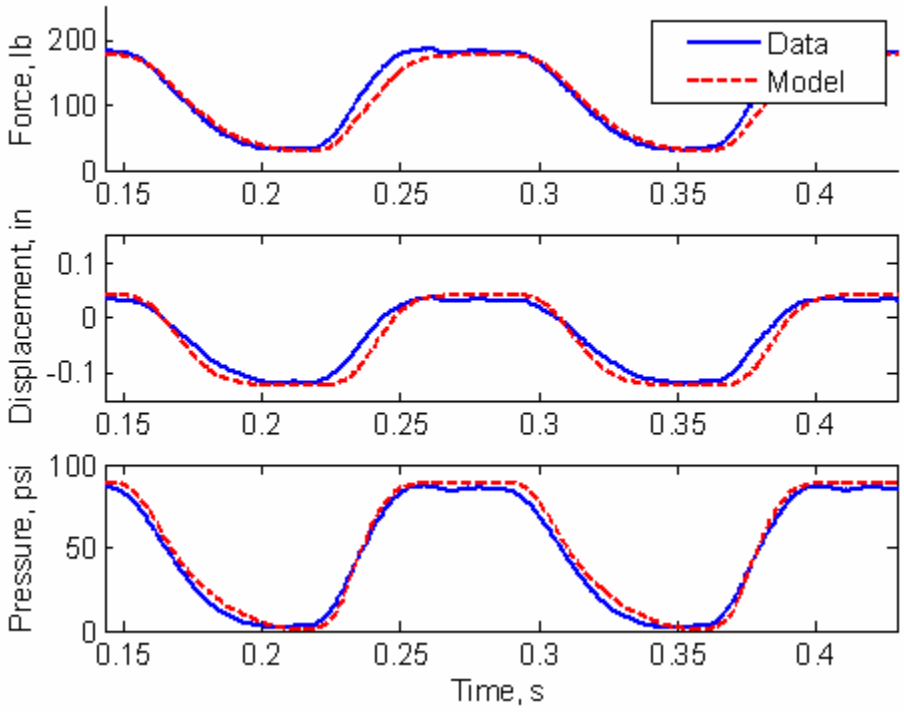

(b)

Fig. 32: SPTA model comparison, 7 Hz sine input (a) low flow; (b) high flow.

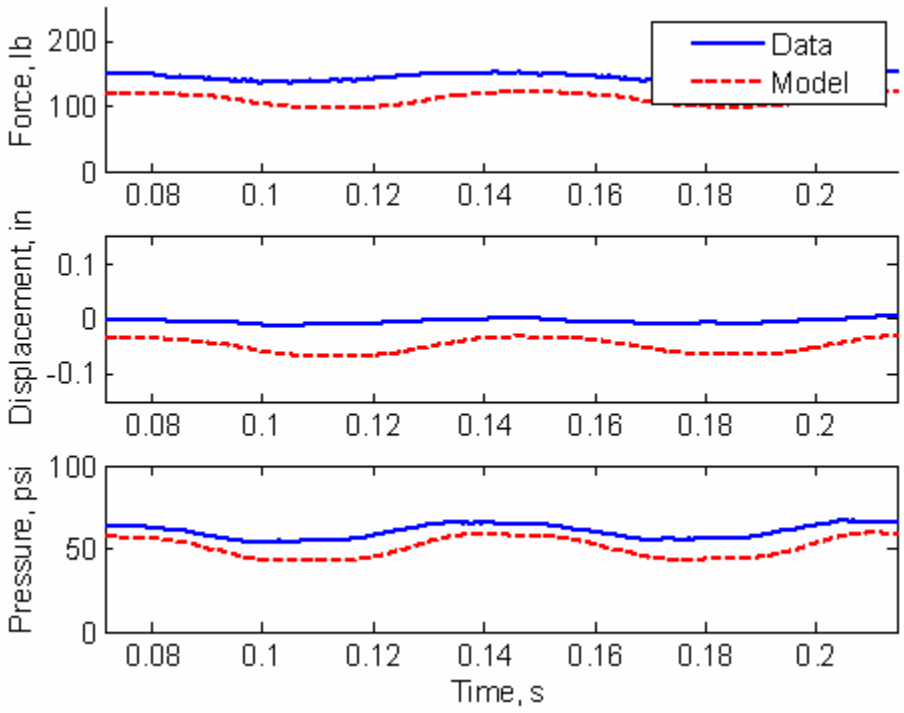

(a)

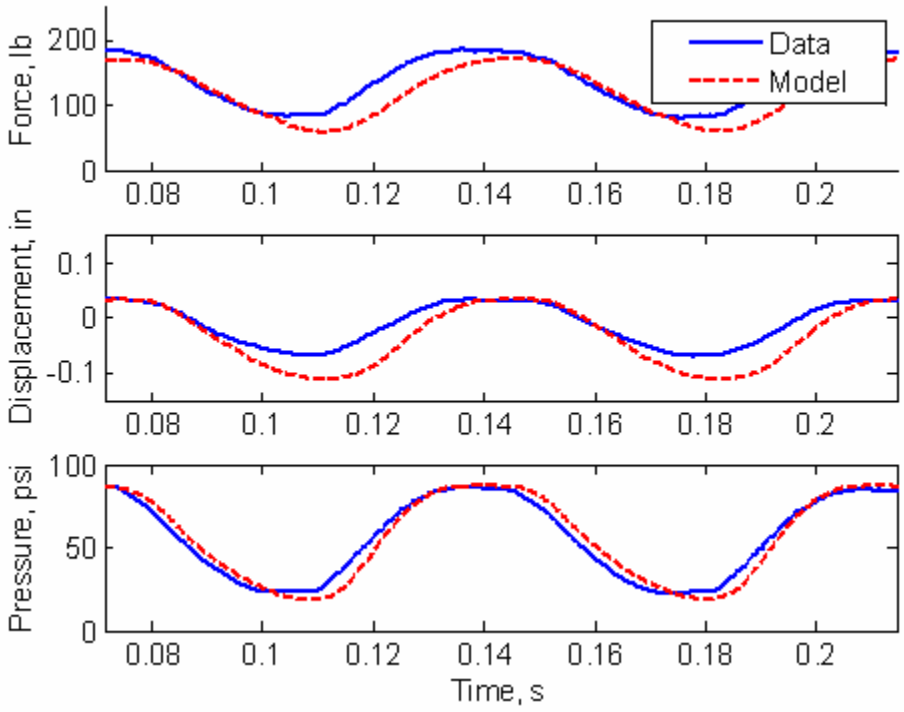

(b)

Fig. 33: SPTA model comparison, 14 Hz sine input (a) low flow; (b) high flow.

2.4 SPTA Controller

The principal objective of this project was to demonstrate the effectiveness of a linear controller on a PAM actuator. To do so, two different controllers, one PI and one PID, were implemented in simulation using displacement feedback, and the better of the two was then tested experimentally on the physical system to verify the simulation results.

2.4.1 SPTA Controller Design

Control was achieved by feeding back PAM displacement and comparing to a reference displacement, r_d, as shown in the Simulink diagram in Fig. 35. The resulting error was input to a built-in PID control block, whose output u_d provided the signal voltage input for the proportional valve. Because the valve accepted signal voltages from 0-10 V and the controller would output both positive and negative voltages, a bias of 4.8 V was added to u_d to provide a neutral signal when no inflation or deflation was commanded. Control gains for both a PID and a PI controller were calculated based on Ziegler and Nichols' tuning rules [40].

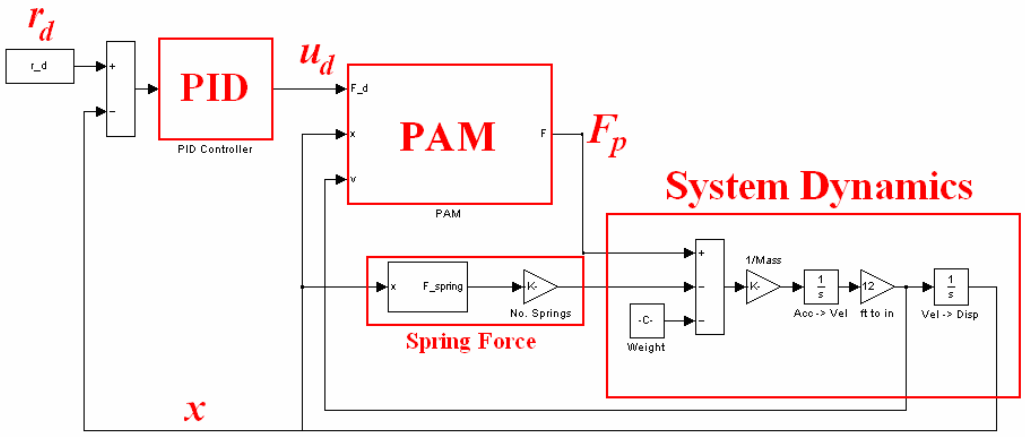

Fig. 34: Displacement feedback control diagram.

2.4.2 SPTA Controller Results and Analysis

To test each controller, a displacement sine sweep was simulated in Simulink from 0.1 to 42 Hz in 1 Hz increments at peak-to-peak amplitude of 0.1 in. This was approximately the maximum displacement achievable by the SPTA and so would provide evidence of each controller's ability to track large displacements at high frequencies.

Frequency responses for the PI and PID controllers are presented in Fig. 35. The two controllers are able to maintain amplitude out to the maximum frequency tested, and seem to overshoot above about 10 Hz. While both controllers begin to lag beyond 10 Hz, the PID controller demonstrates better phase response than the PI controller with increasing frequency.

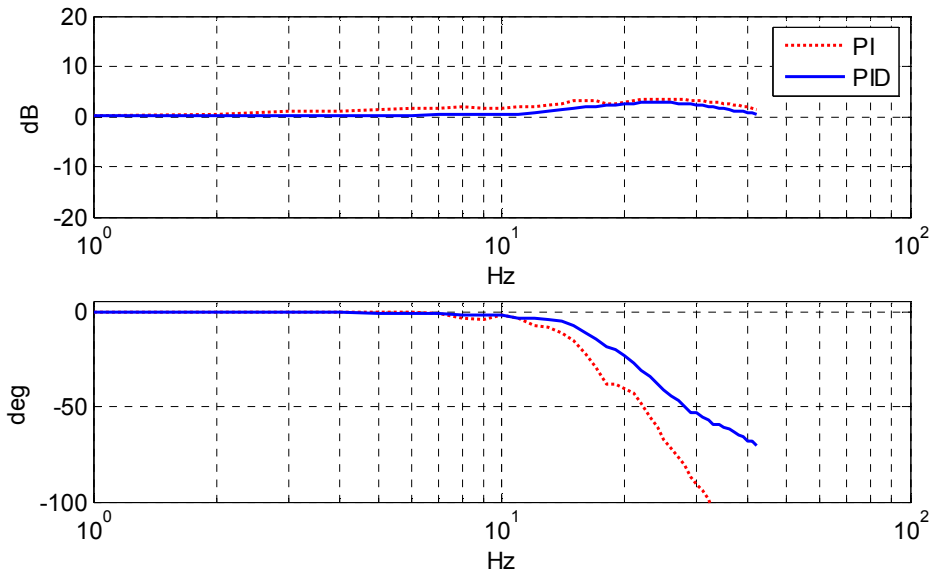

Fig. 35: Simulated frequency response of PI and PID controllers.

A comparison of the waveform of the PI and PID responses yields further evidence of the PID controller's superiority for this application. In Fig. 36 through Fig. 39, closed loop responses for each controller are provided at a sample of different frequencies. In each figure, the reference input is provided as a dotted line.

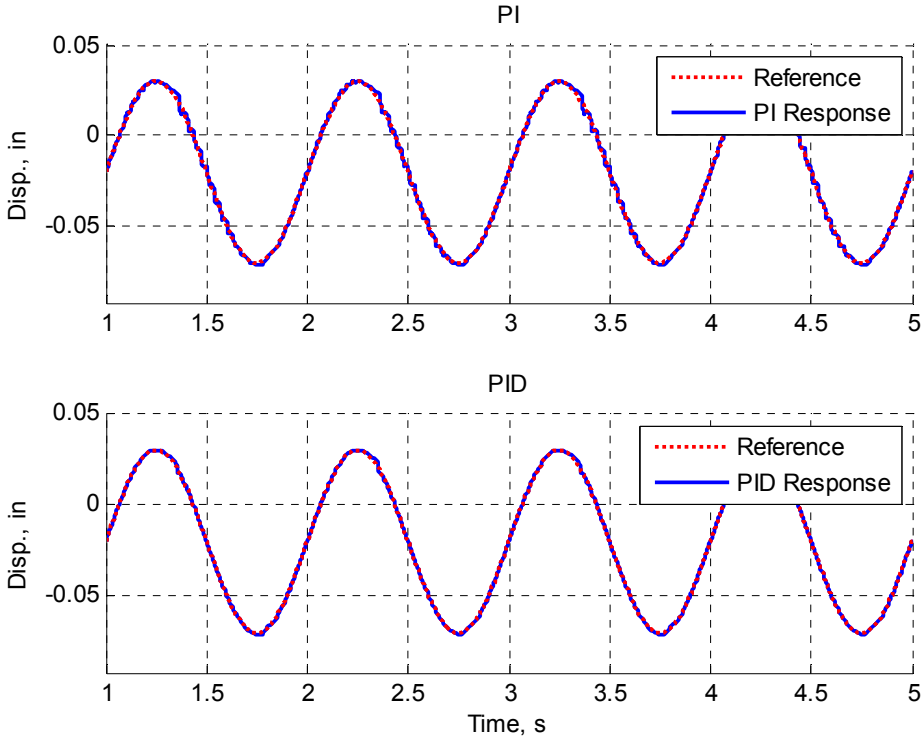

Fig. 36: SPTA simulation, controller comparison, 0.1" sine input, 1 Hz.

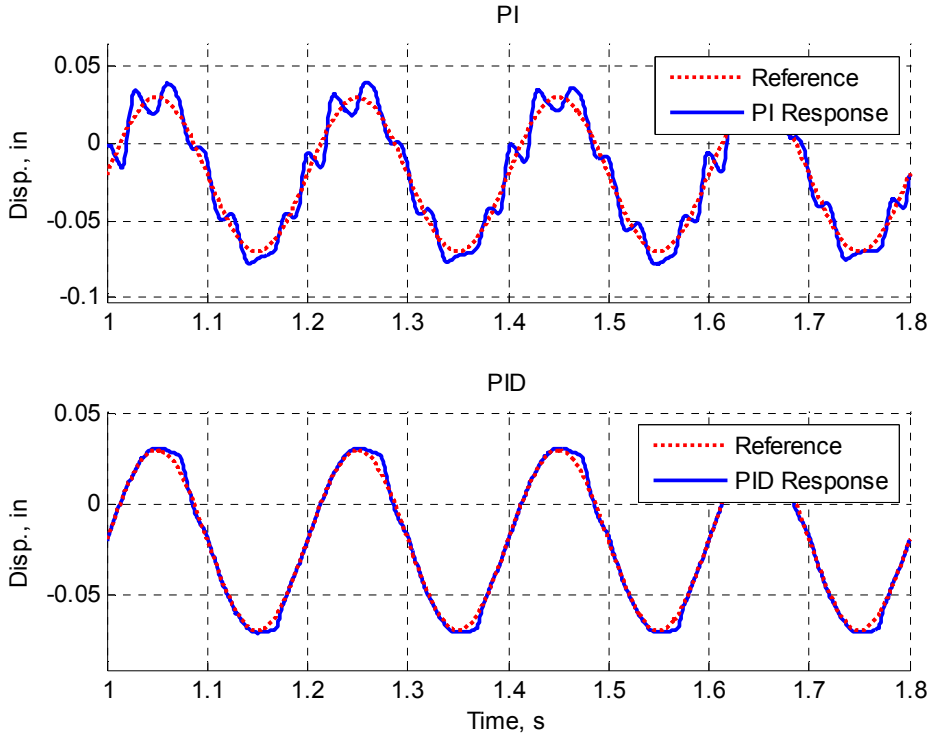

Fig. 37: SPTA simulation, controller comparison, 0.1" sine input, 5 Hz.

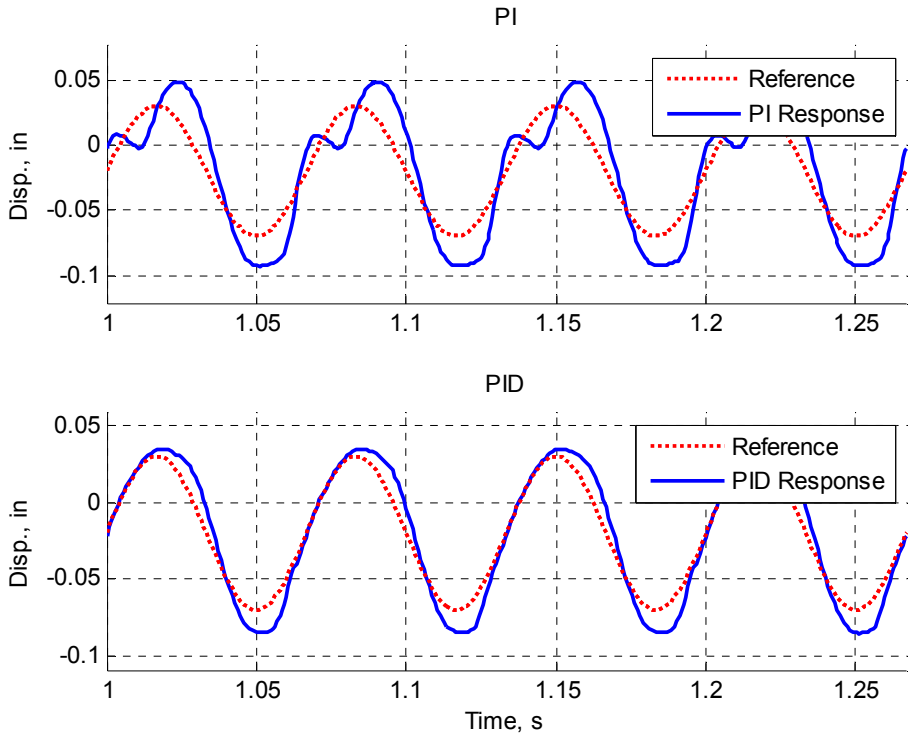

Fig. 38: SPTA simulation, controller comparison, 0.1" sine input, 15 Hz.

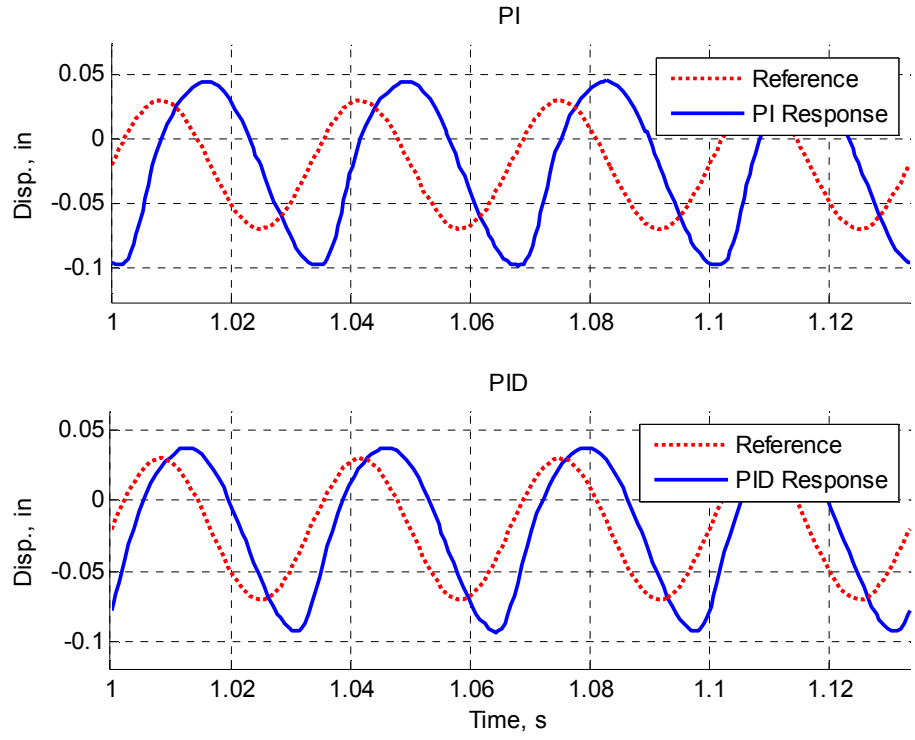

Fig. 39: SPTA simulation, controller comparison, 0.1" sine input, 30 Hz.

At low frequencies such as the 1 Hz case in Fig. 36, the PI and PID controllers both track the reference waveform with almost no deviation. As frequency increases, the PI controller appears unable to replicate the reference waveform. Considerable oscillation about the desired path is apparent around 5 Hz for the PI controller, as seen in Fig. 37. This oscillation is still apparent at 15 Hz in Fig. 38, along with noticeable phase shift and overshoot in overall amplitude. The PID controller continues to track the reference waveform well in Fig. 37 and Fig. 38. As frequency increases, both the PI and PID response take on approximately the same shape and overshoot as in Fig. 39, yet the PID response still exhibits less phase lag.

Based upon these results, the SPTA actuation system coupled with a PID controller appears capable of performing adequately for a hypothetical aerodynamic control surface. To use a familiar example, an active control surface on a helicopter rotor blade is typically expected to track large inputs at the rotor frequency for primary control and smaller inputs at the N-1, N, and N+1 harmonics of the rotor frequency for vibration control, where N is the number of blades on the rotor [41]. In Fig. 40, the controller tracks a simulated 4-blade active rotor displacement input which is a sum of four sine waves. The primary control input is a 7 Hz, 0.1” peak-to-peak sinusoid, and the higher order inputs are 21, 28, and 35 Hz inputs at 1/8, 1/10, and 1/12 the primary amplitude, respectively. This ability to track an arbitrary input with higher harmonics provides a good qualitative demonstration of the utility of the controller and actuation system for active aerodynamic surfaces.

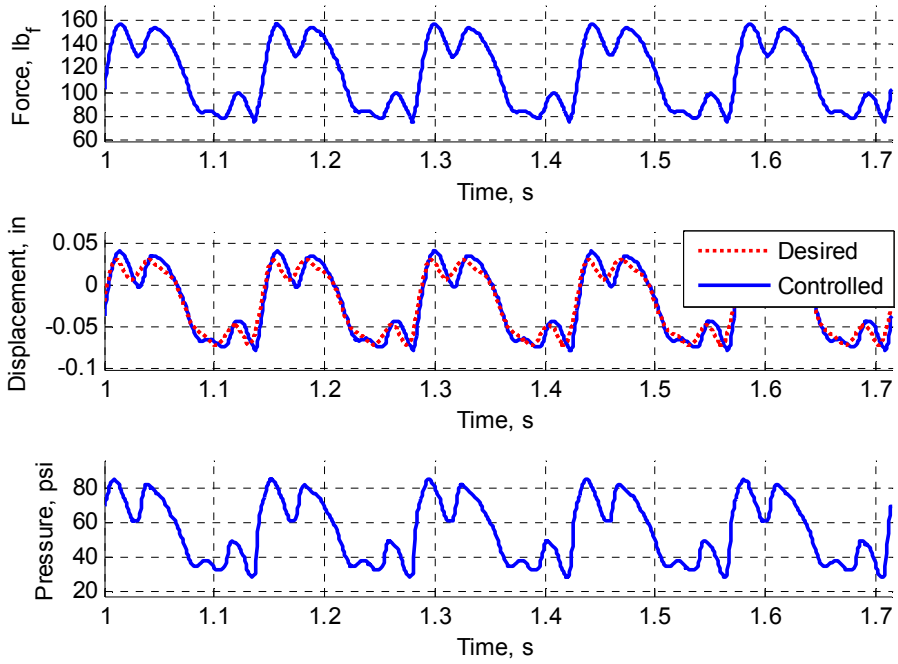

Fig. 40: Prediction of higher order closed loop displacement tracking capability, 7 Hz + 3ω, 4ω, and 5ω sine excitation.

2.5 SPTA Closed Loop Experimental Results

To validate the promising simulation results achieved using PID, a PID controller implemented in dSPACE was used to control the physical SPTA system. In order to select the control gains, the values found during simulation by Ziegler-Nichols tuning were used as a starting point, and optimization was done manually. Gains were introduced one at a time, proportional, integral, and then derivative, and adjusted by hand to find an optimum value before the next gain was included. The proportional and derivative gains from simulation was found to be appropriate, but integral gain was reduced by a factor of roughly 4, and a 50 Hz low pass Butterworth filter was included to prevent the derivative gain from causing instability. The closed loop response to a 0.1 in

sine wave was then measured at a range of frequencies between 0.1 Hz and 42 Hz, identical to the frequency sweep performed in simulation.

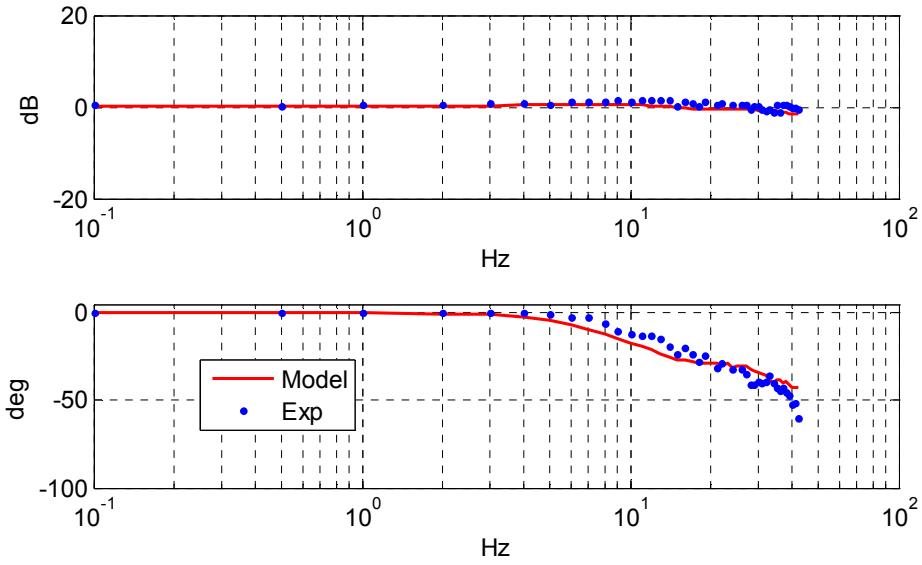

Fig. 41: SPTA closed loop frequency response using PID as compared with model.

Frequency response results are presented in Fig. 41 in comparison with model predictions. The model controller's integral gain was reduced to the same value used in experiment when making these plots. However, the low pass filter used in the experiment was not included here, the effect of which will be discussed later. Note that the appearance of phase lag coincided with an increase in amplitude for both the model and physical system. However, the model predicted a slightly lower corner frequency of about 4 Hz rather than 7-8 Hz for the physical system. Also, the physical system displayed a slightly steeper increase in phase lag with frequency than the model predicts. Still, the model predicts the results of the experimental frequency sweep fairly well.

Closer examination of the waveforms produced by the physical closed loop system reveals important differences between model and experiment. In Fig. 42 through Fig. 45, model and experimental results are compared at 1, 5, 12, and 24 Hz.

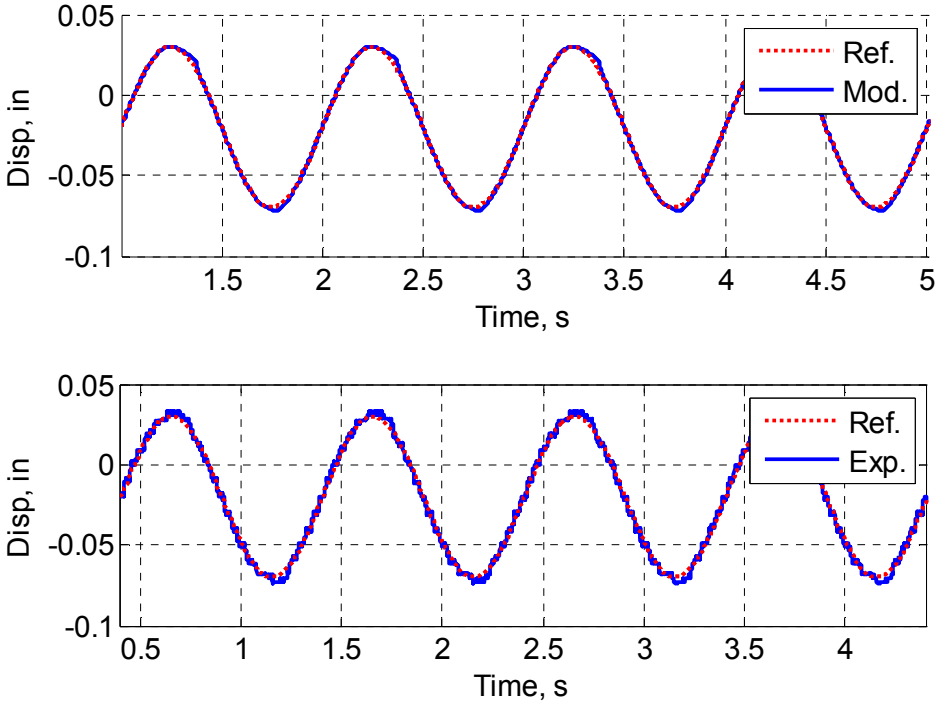

Fig. 42: Model PID (top) vs. experiment PID (bottom), 1 Hz.

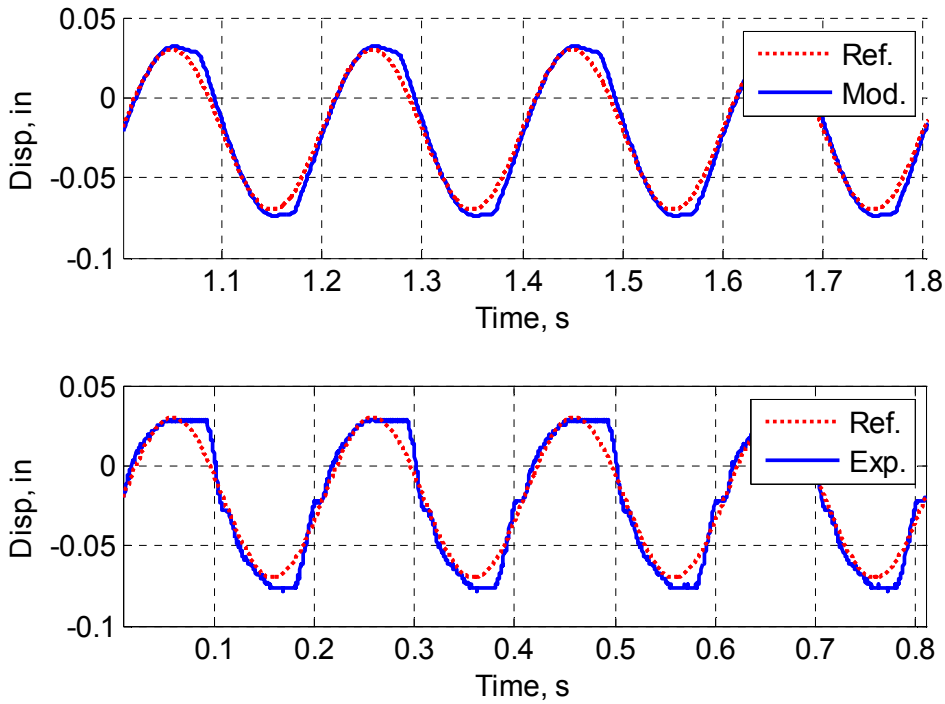

Fig. 43: Model PID (top) vs. experiment PID (bottom), 5 Hz.

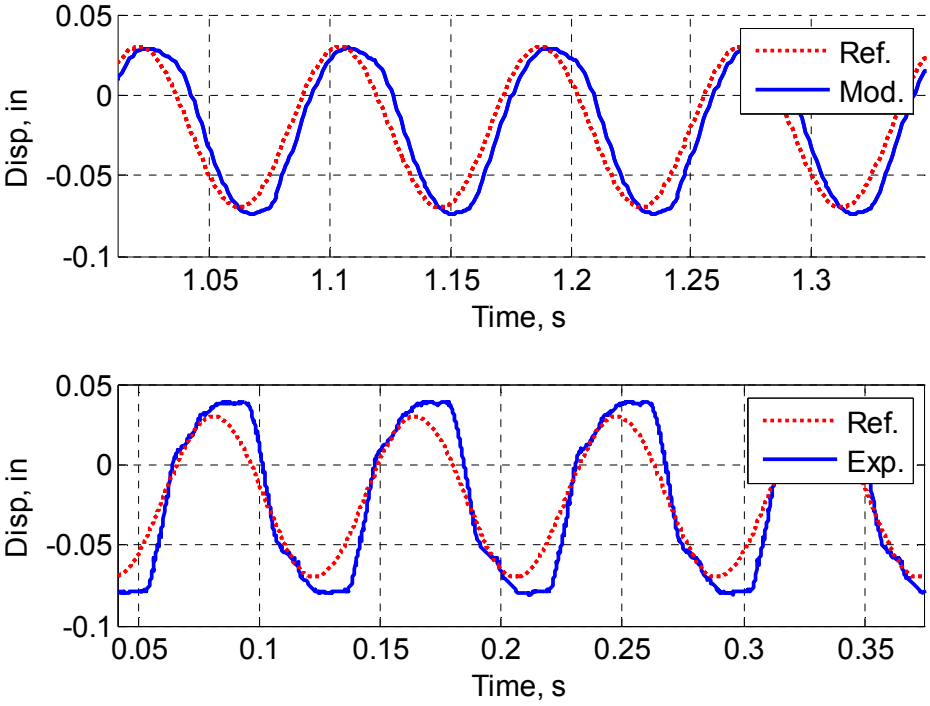

Fig. 44: Model PID (top) vs. experiment PID (bottom), 12 Hz.

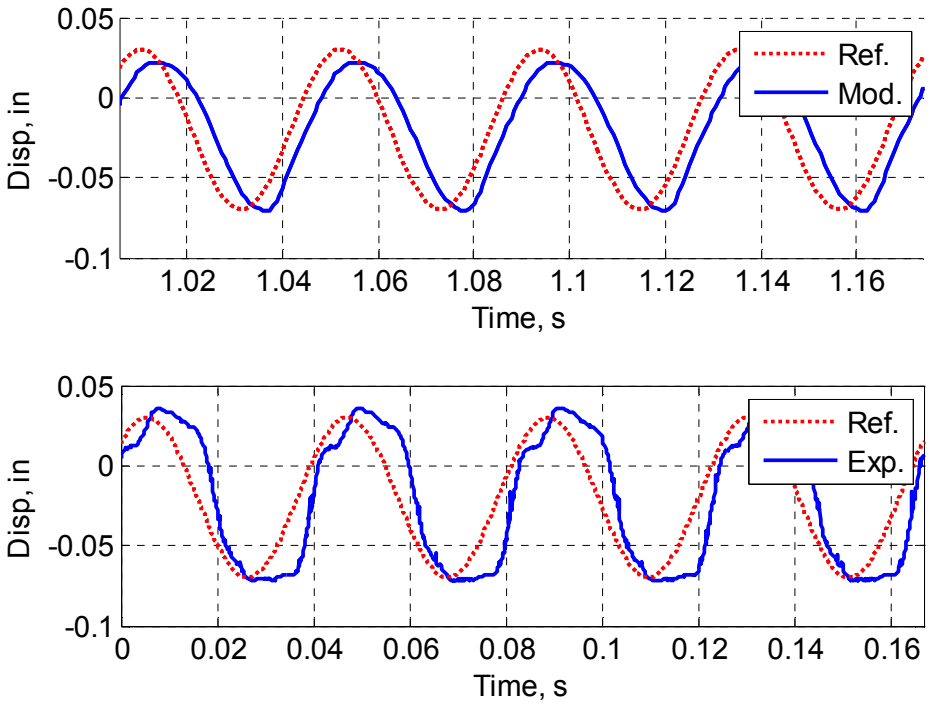

Fig. 45: Model PID (top) vs. experiment PID (bottom), 24 Hz.

A number of key differences can be seen between the model and experimental waveforms. First, the experimental response oscillates at small amplitude and high frequency about the reference signal, which can be seen clearly at 1 Hz in Fig. 42. Second, at frequencies as low as 5 Hz, the physical system lagged behind the reference signal after each peak and trough to a much greater degree than the simulation. In Fig. 43, the model response (top) does exhibit some lag after each direction change, but in the experiment response this lag is greatly exaggerated. At higher frequencies the experimental response actually overshoots at each direction change, as seen at 12 Hz in Fig. 44. The experimental response essentially levels off at each direction change, taking up to 30 ms to respond to the change in direction. Increasing integral and proportional gain did alleviate this to some extent at lower frequencies, but at the expense of stability at higher frequencies (not shown). Last, distortions to the waveform become evident with increasing frequency similar to those seen in the simulated PI response in Fig. 38. The 24 Hz experimental response in Fig. 45 seems to show signs of this phenomenon at the peak of each cycle. While the simulation continues to produce almost a perfect sine wave, the physical system produces an increasingly irregular shape, indicating nonlinearities which are not accounted for in the model.

Several physical explanations for these discrepancies were explored through modification of the model. The use of dSPACE for controller implementation had two major effects not included in the model: analog to digital conversion resulted in some degree of quantization error, and the controller operated in discrete time steps in contrast with the continuous states used in the model. The inclusion of quantization error and

conversion to a fixed time step discrete solution had no discernable effect on the model results.

As mentioned previously, the low pass Butterworth filter applied to the sensor data in the experimental implementation of the controller was not included in the model predictions in Fig. 42 through Fig. 45. Some testing was done to determine the effects of the filter on the model, but the results were inconsistent in terms of matching the experiment qualitatively. At low frequencies, the inclusion of the filter seemed to improve the model's agreement with experiment, as seen in Fig. 46. The small, high frequency oscillation about the reference signal displayed by the experiment in Fig. 42 was replicated by inclusion of the filter.

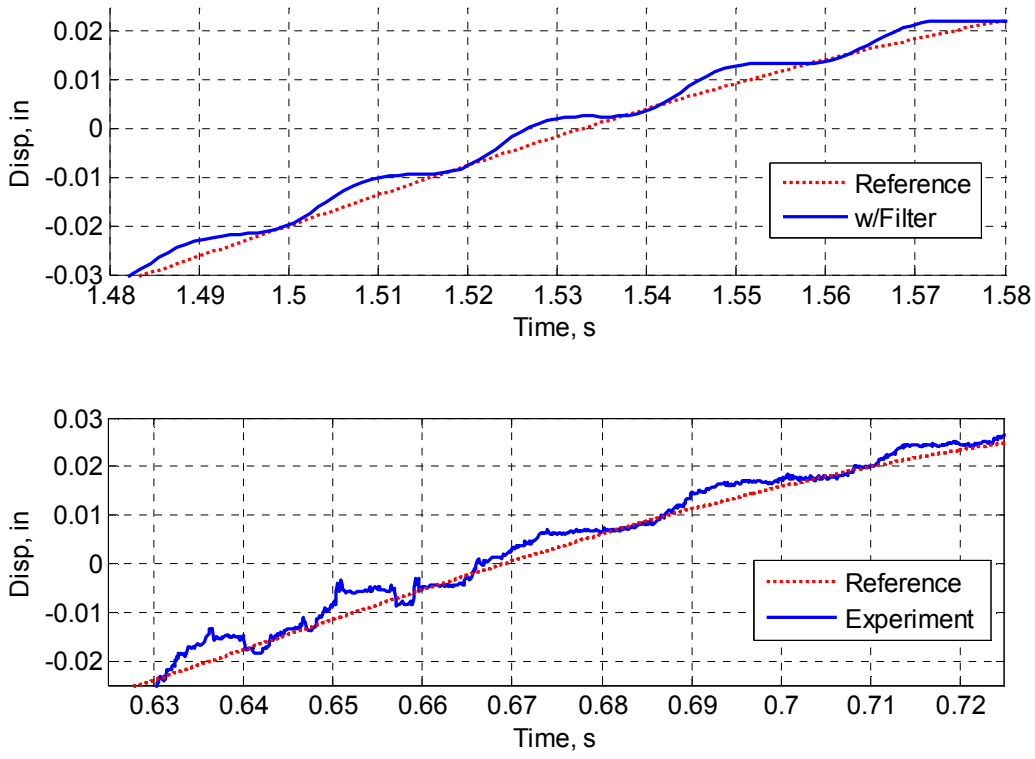

Fig. 46: Effect on model of including low pass Butterworth filter at 2 Hz

However, at frequencies above about 4 Hz, the model results continued to exhibit larger and larger oscillations which were not evident in the experimental results. The divergence was wide enough that the filter effects were not included in the final model predictions. While the filter definitely has some impact on the system, there must be further unmodeled nonlinearities contributing to the high frequency content seen in the experimental results in Fig. 43 through Fig. 45.

Therefore, in spite of their apparently similar frequency responses, the closed loop SPTA system's displacement waveform differed from the simulation at higher frequencies. The helicopter active rotor input simulated in Fig. 40 was repeated in experiment to illustrate the simulation limitations. The same input was used, a 0.1 in amplitude 7 Hz sine wave with higher harmonics at 21 Hz, 28 Hz, and 35 Hz included at lower amplitudes. The closed loop physical response displayed in Fig. 47 largely tracks the input, but as expected fails to track the higher harmonics as well as simulation would suggest.

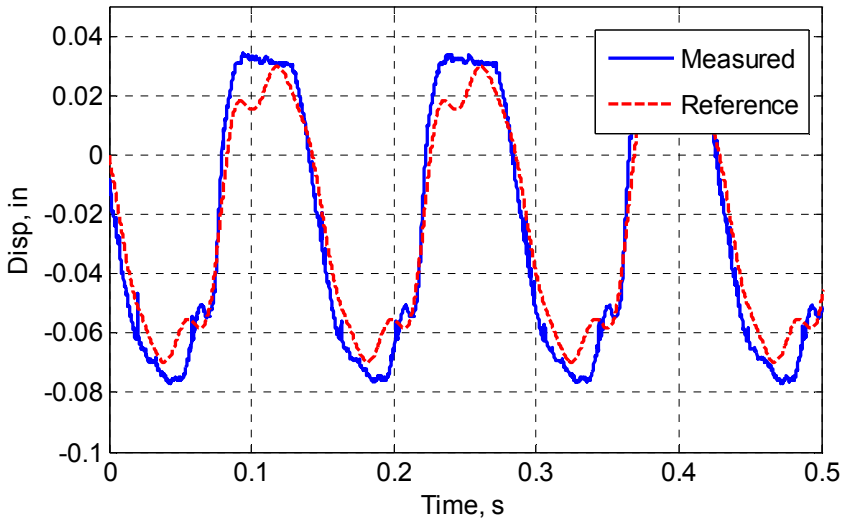

Fig. 47: Experimental closed loop tracking of higher order harmonic input, 7 Hz + 3ω, 4ω, and 5ω sine excitation.

Evaluating system performance based on the control requirements for a fixed-wing UAV, rather than a hypothetical active rotor input, provides a better yardstick for the SPTA controller's usefulness. As a starting point, human pilot bandwidth can be as high as 5-7 Hz, but more realistically is approximately 3 Hz [42,43]. Thus control actuation in response to pilot inputs appears well within the capabilities of the controller/actuator simulated here.

For a UAV, however, smaller scale and lighter weight will lead to reduced inertias and higher natural frequencies than manned craft. Therefore higher bandwidth actuators will be required for stabilization of modes. Using Froude scaling to ensure commonality of inertia/gravity and air/gravity force ratios, a UAV would have a higher natural frequency than a larger aircraft by the square root of the scale factor [44]. As an example, a UAV four times smaller than a light piloted aircraft would have natural frequencies twice as high and require twice the actuation bandwidth to stabilize.

Examining the short period mode for a small UAV provides a reasonable minimum requirement for the SPTA controller's corner frequency. Assuming the UAV's short period frequency can be predicted using Froude scaling, based on a light aircraft with a wingspan of 36 ft and a marginally stable short period frequency of 10 rad/s, a UAV with a 3 ft wingspan would have a short period frequency of 34.6 rad/s or 5.5 Hz. The PAM actuation system presented here demonstrated useful waveform tracking with low phase lag to roughly 8 Hz. Based upon 5.5 Hz as the desired operating frequency, the PAM actuation system would be sufficient for control and stabilization of even a small UAV.

2.6 Conclusion

A PID displacement feedback controller was designed for a single PAM working against a spring with nonlinear stiffness. First a physical system was fabricated and characterized. A Simulink model of the system was then developed and validated using experimental data. The model was used to compare PI and PID control over a large range of operating frequencies. The PID controller displayed superior frequency response and output waveform and was implemented on the physical system to confirm model predictions.

1. The SPTA Simulink model relied heavily on characterization of certain system components, particularly the pneumatic valve and the PAM actuator. Unmodeled nonlinearities limit the usefulness of the model above approximately 10 Hz. However, below this frequency the model matched the nonlinear system performance acceptably under a variety of conditions and this modeling approach would be useful as a design tool for future PAM applications.
2. The tubing loss term in Eq. (14) as presented in [33] by Richer and Hurmuzlu does not appear to predict realistic tubing losses in this simulation. When using the Richer and Hurmuzlu term, predicted flow rate is far slower than demonstrated by experiment for any appreciable tubing length. Assuming Poiseuille flow to calculate pressure drop due to tubing loss provided a much better prediction of pneumatic system performance.
3. Displacement feedback PID control of a PAM actuator system using a proportional valve is shown to be sufficient for tracking a useful range of frequencies at high displacement. For operation below approximately 8 Hz, the PID controller provides

good tracking and waveform replication, results which are sufficient to control a UAV. This contradicts assertions made in a number of PAM control studies suggesting an adaptive or nonlinear controller is necessary to stabilize and control a PAM actuator system at frequencies above 1 Hz. Thus this conclusion makes a contribution to the literature by testing a combination of proportional valve and linear PID controller that has not previously been demonstrated on a PAM system and proving it useful up to 8 Hz.

Chapter 3

Design and Fabrication of a Passive 1-D Morphing Aircraft Skin

3.1 Overview

The primary challenge in developing a morphing skin suitable as an aerodynamic surface is balancing the competing goals of low in-plane actuation requirements and high out-of-plane stiffness. In order to make the skin viable, actuation force requirements must be modest enough to enable a reasonably sized actuation system to stretch the skin to the desired shape and hold it for the required morphing duration. At the same time, the skin must support typical aerodynamic loads without deforming excessively (e.g., rippling or bowing) and degrading the aerodynamic characteristics of the airfoil surface.

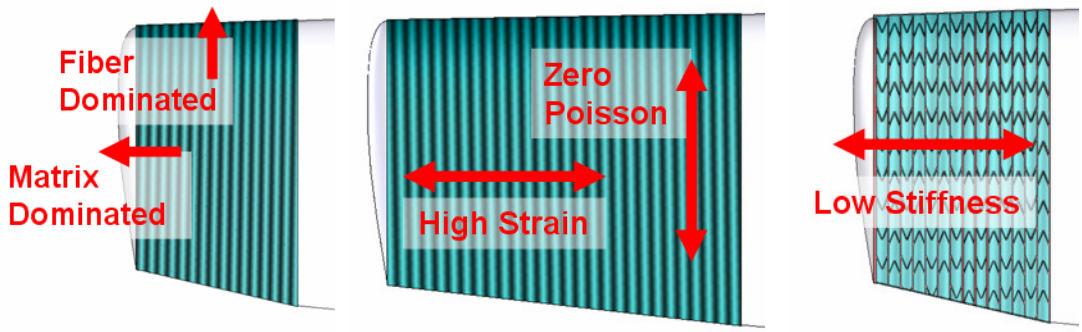

Fig. 48: Overview of morphing skin conceptual design.

To achieve these design goals, a soft, thin silicone elastomer sheet with highly anisotropic carbon fiber reinforcement called a flexible matrix composite (FMC) would be oriented such that the fiber-dominated direction runs chordwise at the wingtip, and the matrix-dominated direction runs spanwise, Fig. 48a. Related research with FMC

materials can also be found [45, 46]. Reinforcing carbon fibers controlling the major axis Poisson's ratio of the sheet would limit the FMC to 1-D spanwise shape change, Fig. 48b. For a given bulk stiffness, actuation requirements will increase in proportion to the skin thickness, t_s, while out-of-plane stiffness will be proportional to t_s^3 by the second moment of the area. Simply increasing thickness to support out-of-plane loading will therefore increase in-plane stiffness as well. To meet these competing goals, a flexible modified honeycomb substructure is desired, Fig. 48c, that is capable of handling out-of-plane loads without greatly adding to the in-plane stiffness. This allows a thinner skin which, in turn, reduces actuation requirements. The combined FMC sheet and honeycomb substructure form a continuous span-morphing skin.

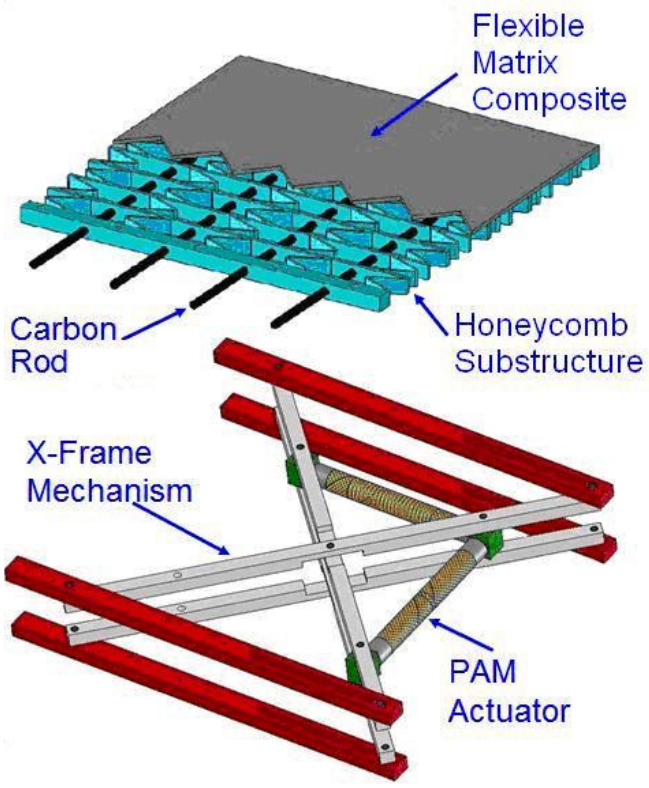

Fig. 49: Proposed morphing skin prototype including PAM actuation system.

To motivate the goal of low in-plane stiffness for this research, the skin prototype was designed in parallel with the span-morphing x-frame actuator mentioned in Chapter 1 and described in [18]. The PAM driven scissor mechanism is shown in Fig. 49 along with a mock-up of the proposed morphing skin. Based upon the predicted abilities of the actuation system, a design skin stiffness was selected that would give greater than 100% strain capability, as modeled in Fig. 50. In this plot, the dashed curve represents the maximum available extensile force predicted for the actuation system, and the solid curve gives the force required to strain the skin based on the design stiffness. Where the two curves intersect determines the maximum strain capability of the morphing system. A margin of 15% was added to the design goal to account for anticipated losses due to friction or manufacturing shortcomings in the skin or actuation system.

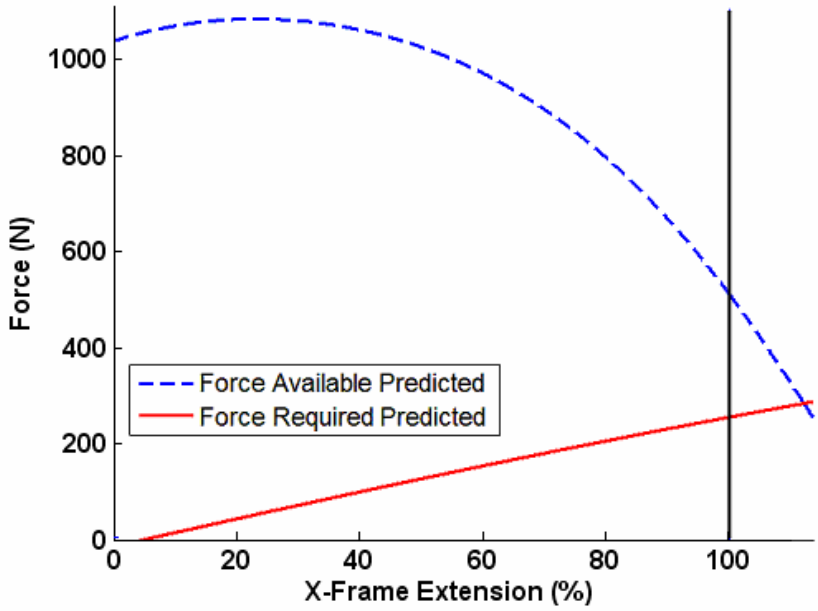

Fig. 50: X-frame force predictions and morphing skin stiffness design goal.

In addition, a design goal was selected for out-of-plane deflection requirements. While under a hypothetical maneuvering wing load of 200 psf (9.58 kPa), an out-of-plane deflection limit of 0.1 in (2.5 mm) was arbitrarily set. Attempting to keep the skin from

deflecting more than this amount gave a reasonable guarantee that the aerodynamic shape of a large UAV wing morphing structure could be maintained during flight.

3.2 FMC Design and Testing

The primary phase of the morphing skin development was to fabricate the FMC sheet that would make up the skin or face sheet. A number of design variables were available for tailoring the FMC to the application, including elastomer stiffness, durometer, ease of handling during manufacturing, and the quantity, thickness, and angle of carbon fiber reinforcement.

3.2.1 Elastomer Selection

Initially, a large number of silicone elastomers were tested for viability as matrix material. Desired properties included maximum elongation well over 100%, a low stiffness to minimize actuation forces, moderate durometer to avoid having too soft a skin surface, and good working properties. Workability became a primary challenge to overcome, as two-part elastomers with high viscosities or very short work times would not fully wet out the carbon fiber layers. While over a dozen candidate elastomer samples were examined, only four were selected for further testing. Fig. 51 and Table 1 detail the silicone elastomers tested as matrix candidates.

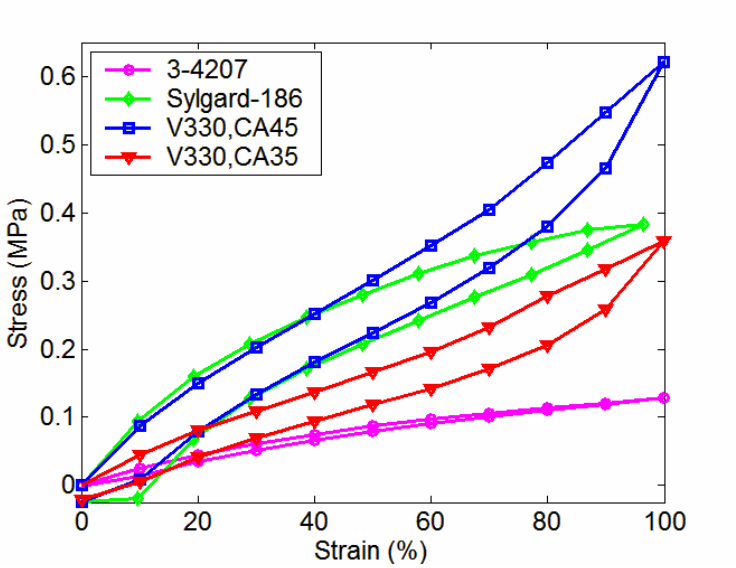

Fig. 51: Elastomer stress-strain curves.

Table 2: Approximate modulus of elastomers.		
Material	**Modulus (kPa)**	**Modulus (psi)**
DC 3-4207	130	19
Sylgard-186	410	59
V-330, CA-45	570	83
V-330, CA-35	330	48

The most promising compositions tested were Dow Corning 3-4207 series and the Rhodorsil V-330 series. Both exhibited the desired low stiffness and greater than 100% elongation, but DC 3-4207 suffered from marginal working qualities and lower maximum elongation and was rejected. Rhodorsil's V-330 series two-part RTV silicone elastomer had the right combination of low viscosity and long work time to enable easy and effective FMC manufacture, and demonstrated high maximum elongation and tear strength. V-330 CA-35 also had the lowest stiffness of the elastomers tested, excluding DC 3-4207. This led to selecting V-330 CA-35 for use in test article fabrication.

3.2.2 CLPT Predictions and Validation

Concurrently, using classical laminated plate theory (CLPT), a simple model of the FMC laminate was developed to test the effects of changing composite configuration on performance. Initial calculations were performed to test the impact of increased number of laminae on out-of-plane stiffness. Only a minor improvement in out-of-plane stiffness was seen and in-plane stiffness suffered greatly. Therefore, the minimal thickness lay-up shown in Fig. 52 was used for further analysis. The basic arrangement calls for two silicone elastomer face sheets sandwiching two symmetric unidirectional carbon fiber/elastomer composite laminae. The fiber layers are offset by an angle θ_f from the **1**-axis, which corresponds to the chordwise direction. Orienting the fiber dominated direction along the chord controls minor Poisson effects while retaining low stiffness and high strain capability in the **2**-axis, which corresponds to the spanwise direction.

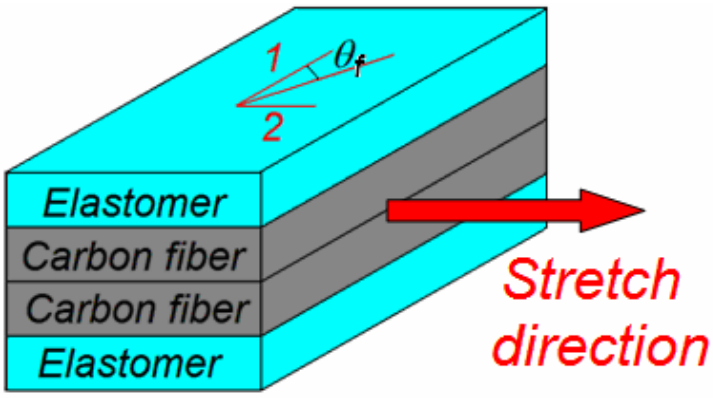

Fig. 52: FMC lay-up used in CLPT predictions

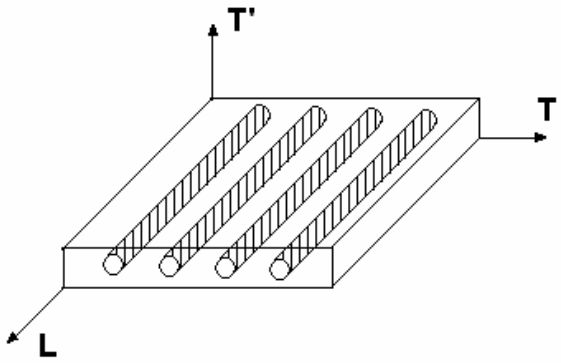

Fig. 53: Unidirectional composite layer showing fiber orientation [47].

In order to determine directional properties of the FMC laminate, directional properties of each lamina must first be found. The following derivation comes from Agarwal et al. [47]. For a unidirectional sheet with the material axes oriented along the fiber direction as shown in Fig. 53, CLPT assumes perfect bonding between the fiber and matrix material such that equal strain is experienced in the longitudinal, or **L**, direction. The longitudinal elastic modulus is given by the rule of mixtures:

$$E_{\mathrm{L}} = E_f V_f + E_m (1 - V_f) \tag{18}$$

Here $E_{\mathbf{L}}$ is the longitudinal elastic modulus for the layer, E_{f} is the fiber elastic modulus, E_{m} is the matrix elastic modulus, and V_{f} is the fiber volume fraction. To find the elastic modulus in the transverse direction, CLPT assumes uniform stress through the matrix and fiber. This in fact proves to be a poor assumption, as will be discussed later. The equation for the transverse modulus, $E_{\mathbf{T}}$, is:

$$E_{\mathrm{T}} = 1/(V_f / E_f + (1 - V_f)/E_m) \tag{19}$$

Similar expressions can be found for the major Poisson's ratio, $\nu_{\mathbf{LT}}$, and shear modulus, $G_{\mathbf{LT}}$, of a unidirectional fiber lamina. Thus, for each of n orthotropic laminae in the FMC, numbered from bottom to top, a stiffness matrix [Q] can be determined. Using the longitudinal modulus from Eq. (18), the transverse modulus from Eq. (19), the shear modulus, and the major Poisson's ratio found for each lamina, a compliance matrix [S] is found, the inverse of which is the lamina stiffness matrix, [Q]:

$$[S] = \begin{bmatrix} E_L^{-1} & -\nu_{LT}/E_L & 0 \\ -\nu_{LT}/E_L & E_T^{-1} & 0 \\ 0 & 0 & G_{LT}^{-1} \end{bmatrix}$$
$$[Q] = [S]^{-1} \tag{20}$$

The stiffness matrix [Q] is given in terms of the material axes in Fig. 53. For a laminate with fiber layers offset from the 1-axis, the stiffness matrix from Eq. (20) must be transformed to the laminate body axes. From the theory, two standard coordinate transformation matrices are obtained as a function of the fiber offset angle, θ_f, yielding an expression for the lamina stiffness matrix transformed into the laminate body axes:

$$\left[\overline{Q}\right] = [T_1(\theta)]^{-1}[Q][T_2(\theta)] \tag{21}$$

Using the transformed stiffness matrix found in Eq. (21) for each lamina k of n laminae, the directional properties of the laminate can now be calculated. The matrices [A], [B], and [D] (the extensional stiffness, coupling stiffness, and bending stiffness matrices, respectively) are determined by summing the weighted laminae stiffnesses using the following equations:

$$
\begin{aligned}
[A] &= \sum_{k=1}^{n} \left[\overline{Q}\right]_k (h_k - h_{k-1}) \\
[B] &= \frac{1}{2} \sum_{k=1}^{n} \left[\overline{Q}\right]_k (h_k{}^2 - h_{k-1}{}^2) \\
[D] &= \frac{1}{3} \sum_{k=1}^{n} \left[\overline{Q}\right]_k (h_k{}^3 - h_{k-1}{}^3)
\end{aligned}
\tag{22}
$$

In these expressions, the values of h_k and $h_{k\text{-}1}$ are the distance of the top and bottom of the k^{th} lamina from the bottom of the FMC laminate. Using the values found for [A], [B], and [D] from Eq. (22), the basic laminate plate constitutive equation is given by:

$$
\begin{Bmatrix} N \\ M \end{Bmatrix} = \begin{bmatrix} A\,B \\ B\,D \end{bmatrix} \begin{Bmatrix} \varepsilon_0 \\ \kappa_0 \end{Bmatrix}
\tag{23}
$$

Here N is a vector of in-plane forces, M is a vector of in-plane moments, ε_0 is a vector of mid-plane strains, and κ_0 is a vector of mid-plane curvatures. For a symmetric laminate such as the one examined here, there is no extension/bending coupling and the B matrix is equal to zero. Equation (23) can then be simplified and expanded for a symmetric laminate yielding:

$$
\begin{Bmatrix} N_1 \\ N_2 \\ N_{12} \end{Bmatrix} = \begin{bmatrix} A_{11} & A_{12} & 0 \\ A_{12} & A_{22} & 0 \\ 0 & 0 & A_{66} \end{bmatrix} \begin{Bmatrix} \varepsilon_1 \\ \varepsilon_2 \\ \gamma_{12} \end{Bmatrix}
\tag{24}
$$

By manipulation of Eq. (24), the laminate transverse modulus and the Poisson's ratio, the two properties of principal interest, can be calculated. Considering a strain in the transverse direction ε_2 due to a force in the transverse direction N_2 for a laminate of thickness t_s and unit width, the transverse elastic modulus can be found from a simple stress-strain relationship:

$$E_2 = \frac{N_2}{t_s \cdot \varepsilon_2} = \frac{A_{22}}{t_s} \tag{25}$$

The minor Poisson's ratio can be found in a similar manner. Consider the ratio of longitudinal strain ε_1 to transverse strain ε_2 due to a transverse force N_2. The minor Poisson's ratio is then given by:

$$\nu_{21} = \frac{\varepsilon_1}{\varepsilon_2} = \frac{N_2 / A_{12}}{N_2 / A_{22}} = \frac{A_{22}}{A_{12}} \tag{26}$$

The CLPT method described above was used as a design tool to explore the effects of different fiber arrangements. Calculations supported the intuitive conclusion that thinner FMC skins would have a lower in-plane stiffness modulus in the spanwise direction, E_2. Predictions for the transverse elastic modulus from Eq. (25) and the minor Poisson's ratio from Eq. (26) are plotted versus fiber offset angle in Fig. 54a and Fig. 54b, respectively, as solid blue lines. In order to provide some validation for the CLPT predictions, three FMC sample coupons were manufactured consisting of 0.5 mm elastomer face sheets sandwiching two 0.2-0.3 mm composite lamina with a fiber volume fraction of 0.7. Nominal fiber offset angles of 0°, 10°, and 20° were used. The measured transverse modulus, Fig. 54a, and minor Poisson's ratio, Fig. 54b, are plotted below as red circles.

It was immediately observed that increasing fiber offset angle adversely increases the in-plane stiffness of the FMC, requiring greater actuation forces. Also, it is noteworthy that the inclusion of unidirectional fiber reinforcement at 0° offset angle nearly eliminates minor Poisson effects.

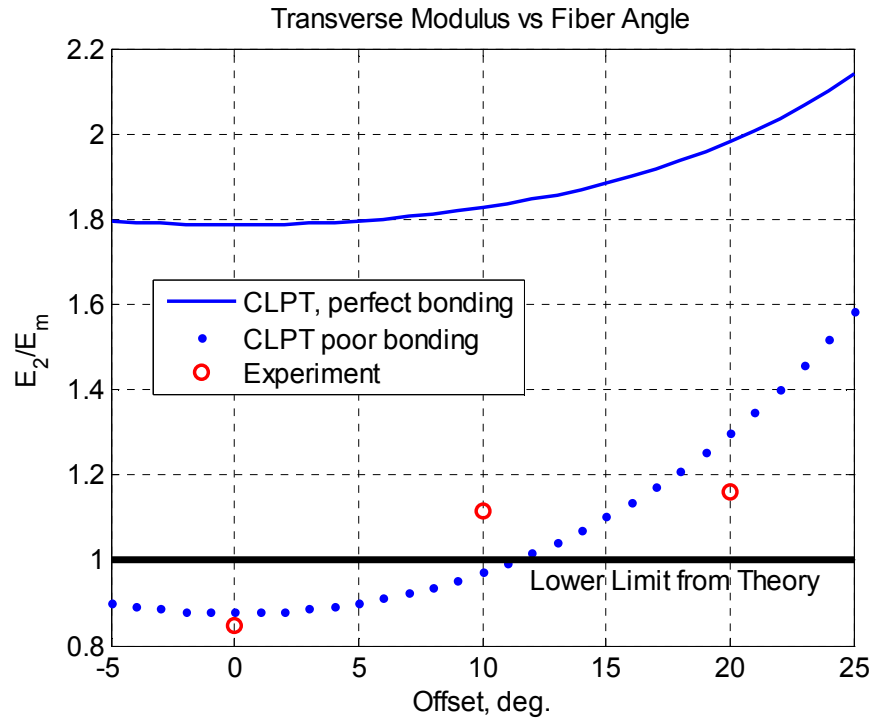

(a)

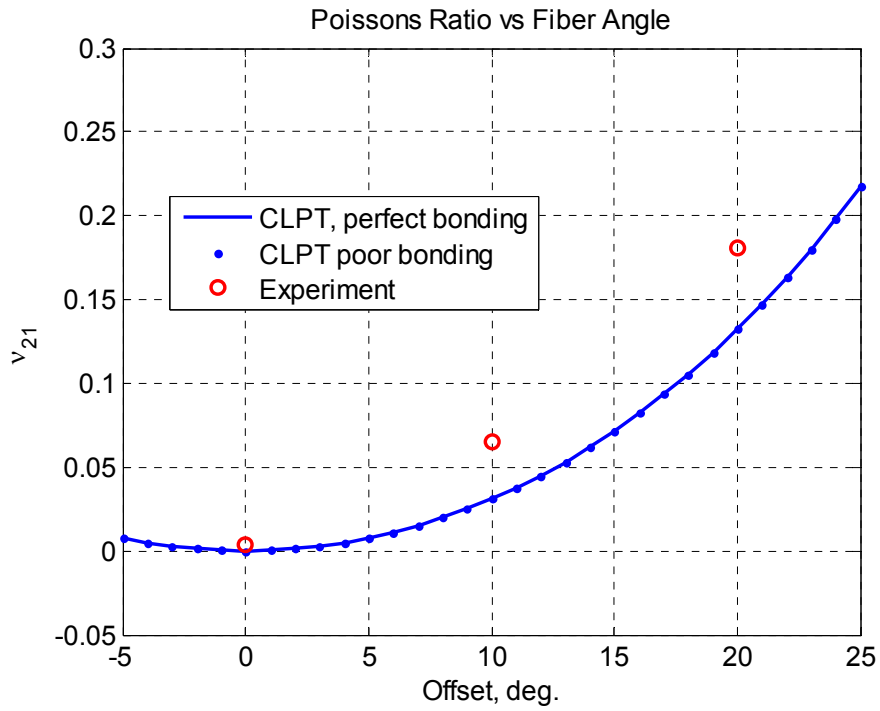

(b)

Fig. 54: Comparison of CLPT predictions with experimental data showing effects of bonding assumptions on solution (a) non-dimensionalized transverse elastic modulus E_2/E_m; (b) minor Poisson's ratio ν_{21}.

It is of critical importance to note that, according to the assumptions used in deriving the lamina transverse modulus in Eq. (19), the transverse modulus has a lower bound equal to the matrix modulus. This lower bound is shown in Fig. 54a as a horizontal black line at $E_2/E_m = 1$. However, the experimental data is close to this lower bound for the 10° and 20° samples, and the modulus is actually below the lower bound for the 0° case. Clearly there is a problem in the assumptions upon which the transverse modulus derivation is predicated.

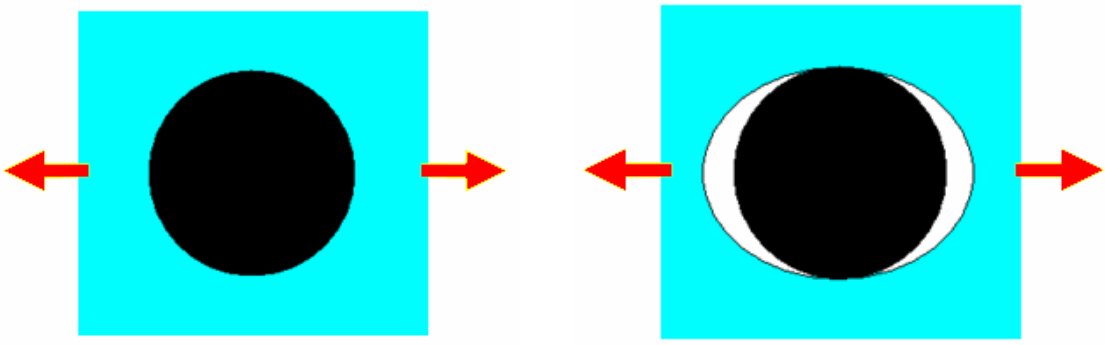

(a) **(b)**

Fig. 55: Fiber/matrix bond (a) assumed perfect bonding and equal transverse stress sharing in CLPT; (b) actual condition with poor fiber/matrix bond and no fiber stress under transverse loading.

Recall it was assumed that perfect bonding between fiber and matrix occurred as illustrated in Fig. 55a. This implies stress was equally shared between matrix and fiber under transverse loading. Close visual examination of the FMC samples during testing revealed that the fiber/matrix bond was actually very poor, and the matrix pulled away from individual fibers under transverse loading as illustrated in Fig. 55b. Thus, the fibers carry no stress in the transverse case, and the effective cross-sectional area of matrix left to carry transverse force in the lamina is reduced by the fiber volume fraction. To account for this, the transverse modulus in Eq. (19) can be replaced with an expression similar to

Eq. (18) by assuming that stress is carried by the matrix alone with a cross sectional area in proportion to its volume fraction:

$$E_{\mathrm{T}} = E_m \cdot (1 - V_f) \tag{27}$$

Using Eq. (27) in the CLPT calculations greatly reduces the transverse stiffness contribution of the fiber lamina, making the overall FMC stiffness less than the stiffness of a solid sheet of matrix material alone at zero degrees fiber angle. Predictions for non-dimensionalized transverse modulus and minor Poisson's ratio are plotted in Fig. 54 as dotted lines. Much better agreement is seen between the analytical and experimental values for E_2/E_{m}.

In spite of the poor bond between fiber and matrix material in the FMCs, the fiber stiffness still appears to contribute to the transverse stiffness at higher fiber offset angles. The minor Poisson's ratio is also influenced by the fiber offset angle, and the FMC's longitudinal modulus, not shown, clearly indicates the fiber is contributing to the stiffness of the laminate. It is hypothesized that friction between fiber and matrix help share load between the two materials in the longitudinal direction, while the matrix is free to pull away from the fiber in the transverse direction. This would explain the stiffening effect seen in the transverse modulus at increased offset angles and the controlling effect the fiber appears to have on Poisson's ratio at very low offset angles.

After this correction to the micromechanics assumptions, the CLPT formulation could be more confidently used to predict FMC directional properties and select a configuration. Based upon these CLPT results, a fiber offset angle of 0° was selected to minimize transverse stiffness and also to minimize the minor Poisson's ratio. As the

analytical and experimental results in Fig. 54b indicate, a 0° fiber offset angle can resist chordwise shape change during spanwise morphing.

3.2.3 FMC Fabrication and Testing

Three FMC samples were manufactured for in-plane testing. First, the outer elastomer face sheets were pre-cured at room temperature between flat plates spaced to give a precise thickness of 0.5 mm, as seen in Fig. 56a. Sheets of 0.15 mm thick, 4.1-oz/yd^2 (0.014 g/cm^2) unidirectional carbon fiber, Fig. 56b, were then prepared by removing the binder threads which otherwise would adversely affect the transverse stiffness. The prepared carbon fiber layers and additional uncured elastomer were then sandwiched between the outer lamina at the appropriate fiber offset angle and cured at room temperature under a weighted aluminum plate. The result was a continuous elastomer matrix with layers of fiber embedded in the center at offset angles, shown before being trimmed to size in Fig. 56c.

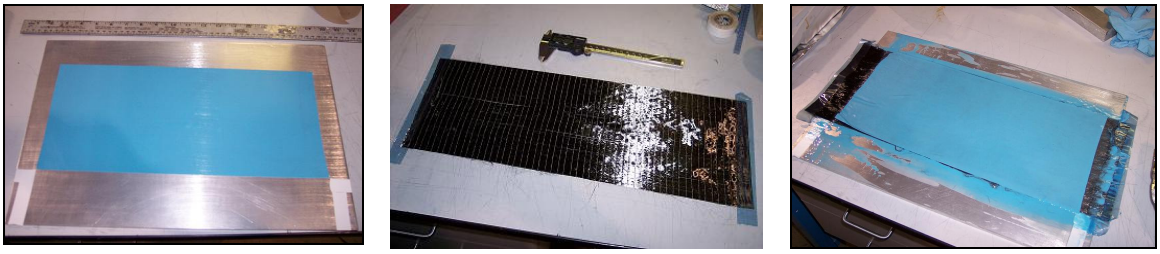

(a) **(b)** **(c)**

Fig. 56: Manufacturing a ~1.5 mm FMC (a) cured 0.5 mm elastomer sheet; (b) raw unidirectional carbon fiber; (c) finished FMC sheet, before trimming and clean-up.

The graphics in Fig. 57 describe the three FMC sheets manufactured in an evolving attempt to maximize in-plane and out-of-plane performance. FMC #1 and FMC #2 had the same lay-up with two 0.5 mm face sheets sandwiching two 0° offset angle carbon fiber layers. However, FMC #1 saw an increased effort to control lamina thickness and

fiber angle to further reduce transverse stiffness, so the carbon fiber lamina ended up slightly thinner than in FMC #2. FMC #3 was a variation intended to increase out-of-plane stiffness at the expense of in-plane stiffness. A single 0° fiber layer was included at the center of the lay-up to affect the minor Poisson's ratio. The central layer was between two symmetric 15° fiber layers, whose offset angle was intended to increase out-of-plane stiffness. Based on CLPT predictions, this FMC was not expected to be competitive with FMC #1 and #2 on in-plane stiffness requirements, but was included in testing to gain experience with other fiber arrangements.

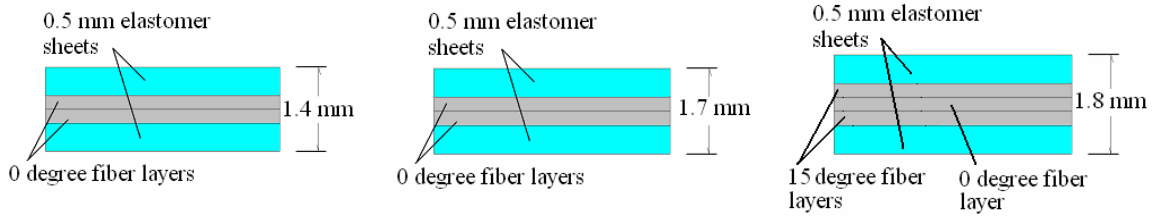

FMC #1 **FMC #2** **FMC #3**

Fig. 57: Lay-ups of FMC samples fabricated for morphing skin evaluation.

Sample strips measuring 51 mm x 152 mm were cut from the three FMCs and tested on an MTS machine. Each sample was strained to 100% of its original length and then returned to its resting position. Data from these tests are presented in Fig. 58. Notice the visibly low Poisson's ratio effects as the FMC is stretched to 100% strain – there is little measurable reduction in width. It is also important to note that the stress-strain curves measured for each FMC reflect not only the impact of their lay-ups on stiffness, but also improvements in manufacturing ability. Thus, due to improved control of carbon fiber angles and the quantity of elastomer matrix, FMC #3 has roughly the same stiffness as FMC #2 in spite of the larger amount of carbon fiber present and higher fiber angles. FMC #1 exhibited high quality control and linearity of fiber arrangement and has the lowest stiffness of all, regardless of its nominal similarity to FMC #2.

Based upon these tests, FMC #1 and FMC #2 were selected for incorporation into integrated test articles. FMC #1 displayed the lowest in-plane stiffness, while FMC #2 had the second lowest stiffness, making them the most attractive candidates for a useful morphing skin.

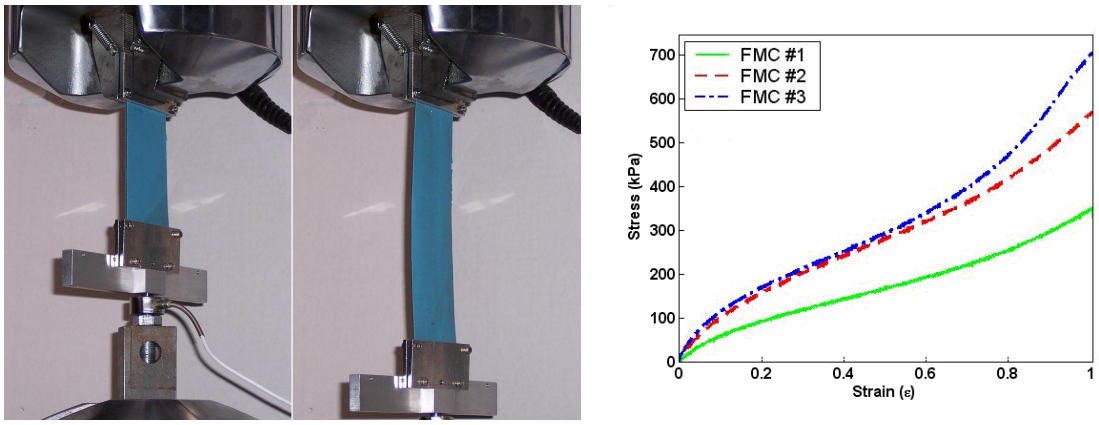

(a) (b)

Fig. 58: In-plane skin testing (a) FMC sample taken to 100% strain; (b) data from FMC samples.

3.3 Substructure Design and Testing

The most challenging aspect of the morphing skin to design was the substructure. Structural requirements necessitated out-of-plane stiffness sufficient to support the entire aerodynamic pressure load while still maintaining low in-plane stiffness and high strain capability.

3.3.1 Honeycomb Design

The substructure concept originally evolved from the use of honeycomb core reinforcement in composite structures such as rotor blades. Honeycomb structures are naturally suited for high out-of-plane stiffness, and if properly designed can have tailored

in-plane stiffness as well [48]. By modification of the arrangement of a cellular structure, the desired shape change properties can be incorporated.

In order to achieve a zero Poisson honeycomb structure, a negative Poisson ratio (auxetic) cellular design presented by Chavez et al. [49] was rearranged to resemble a series of v-shaped members connecting parallel rib-like structures, as seen in comparison in Fig. 59. This arrangement gives large strains in one direction with no deflection at all in the other by means of extending or compressing the v-shaped members.

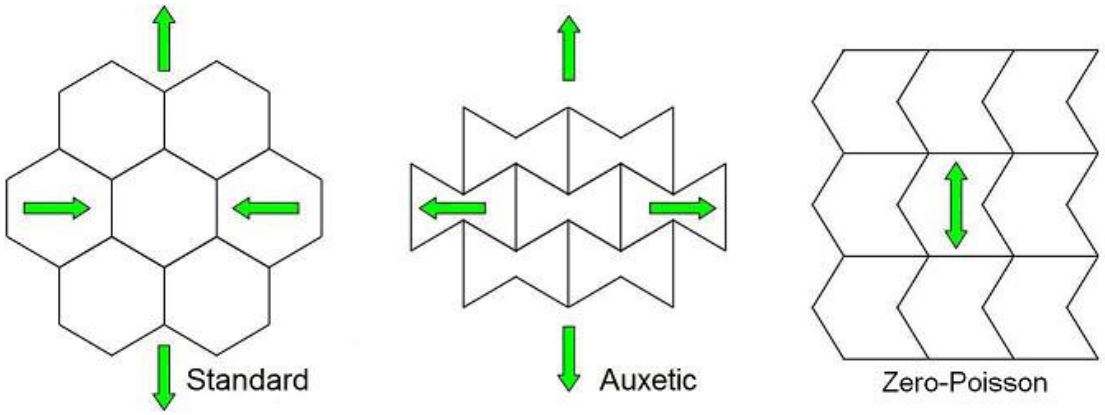

Fig. 59: Comparison of standard, auxetic, and modified zero-Poisson cellular structures showing strain relationships.

For a standard honeycomb, Gibson and Ashby [48] describe the in-plane stiffness as a ratio of in-plane modulus to material modulus, given in terms of the geometric properties of the honeycomb cells. By modifying this standard equation, it is possible to describe the in-plane stiffness of a zero-Poisson honeycomb structure with cell geometric properties as illustrated in Fig. 60. Here t is the thickness of the bending members, ℓ is the length of the v-shaped bending members, h is the cell height, c is the cell width, and θ is the angle between the rib members and the bending members. Note that in the figure the cell is being stretched vertically and F is the force carried by a bending member under tension. Also note that the depth of the cell, denoted as b, is not represented in Fig. 60.

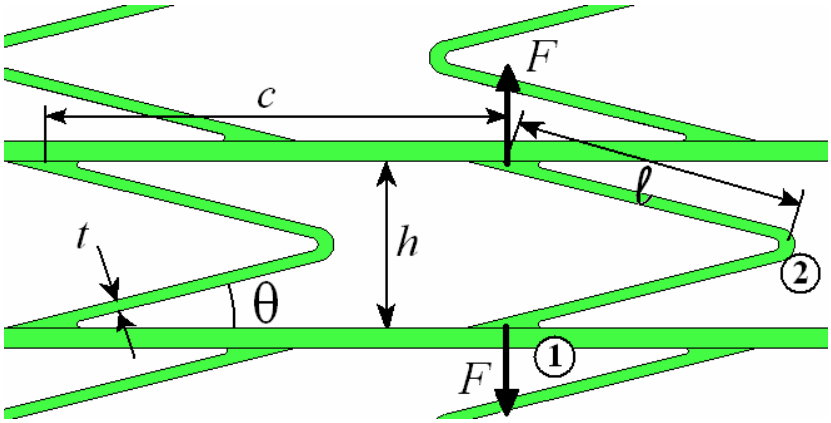

Fig. 60: Geometry of zero-Poisson honeycomb cell.

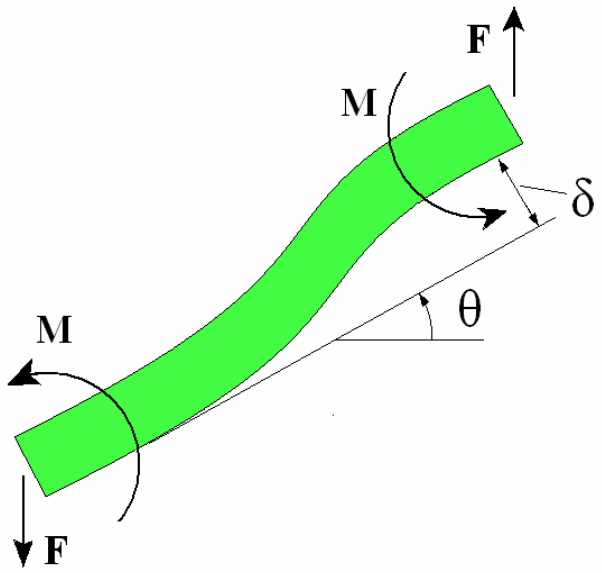

Fig. 61: Forces and moments on bending member leg.

With the geometry of the cell defined, an expression can be found for the honeycomb's equivalent of a stress-strain relationship. For small deflections, the bending member between points **1** and **2** in Fig. 60 can be considered an Euler-Bernoulli beam as shown in Fig. 61, with the forces causing a second mode deflection similar to a pure moment. From Euler-Bernoulli theory, the cosine component of the force F will cause a bending deflection δ [50]:

$$\delta = \frac{F \cos\theta \ell^3}{12 E_0 I} \tag{28}$$

Here E_0 is the Young's Modulus of the honeycomb material and I is the second moment of the area of the bending member; in this case $I = bt^3/12$. In order to determine an effective stiffness modulus for the honeycomb substructure, the relationship in Eq. (28) between force and displacement needs to be transformed into an equivalent stress-strain relationship. The equivalent stress through one cell can be found by using the cell width c and honeycomb depth b to establish a reference area, and the global equivalent strain is determined by non-dimensionalizing the v-shaped member's bending deflection 2δ by the cell height h. These equivalent stresses and strains are used to determine a stiffness modulus for the honeycomb, E_1:

$$\sigma_1 = \frac{F}{cb}, \tag{29}$$

$$\varepsilon_1 = \frac{\delta \cos\theta}{h/2}, \tag{30}$$

$$E_1 = \frac{\sigma_1}{\varepsilon_1} \tag{31}$$

Substituting Eqns. (29) through (31) into Eq. (28) and simplifying yields the following expression for the stiffness of the overall honeycomb relative to the material modulus:

$$\frac{E_1}{E_0} = \left(\frac{t}{l}\right)^3 \frac{\sin\theta}{\frac{c}{l}\cos^2\theta} \tag{32}$$

Because this modified Gibson-Ashby model assumes the bending member legs to be beams with low deflection angles and low local strains, Eq. (32) should only be valid for global strains that result in small local deflections. However, it will be shown that due to the nature of the honeycomb design, relatively large global strains are achievable with only small local strains.

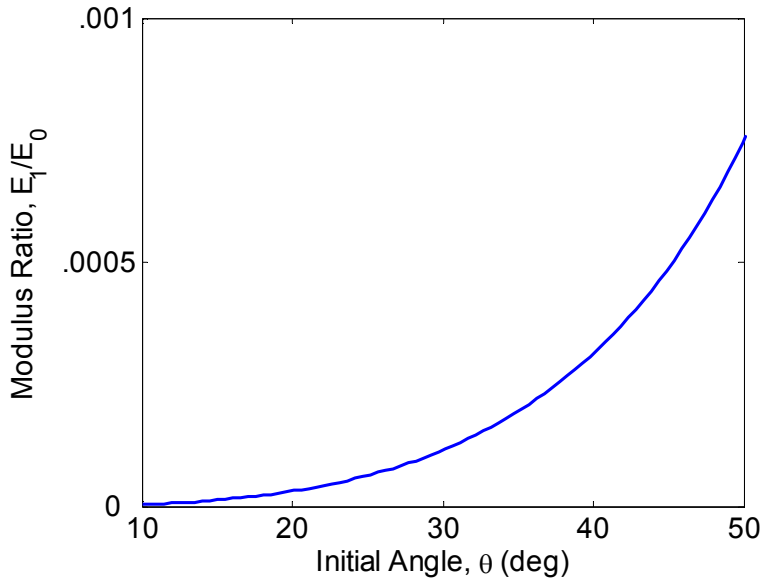

Fig. 62: Analytical results for substructure in-plane stiffness.

With this fairly simple equation, the cell design parameters can easily be varied and their effect on the overall in-plane stiffness of the structure can be studied. For fixed values of t, h, c, and b, the modulus ratio of the structure, E_1/E_0, is plotted in Fig. 62 as a function of the angle θ. As it is shown, smaller angles result in lower in-plane modulus values. Noting the definitions in Fig. 60, it can be seen that decreasing θ consequently affects the bending member length l, as the upper and lower ends must meet to form a viable structure. Thus, for a given cell height h, minimum stiffness limitations are introduced into the design from a practicality standpoint in that the bending members

must connect to the structure and cannot intersect one another. Lower in-plane stiffness can be achieved by increasing cell width to accommodate lower bending member angles.

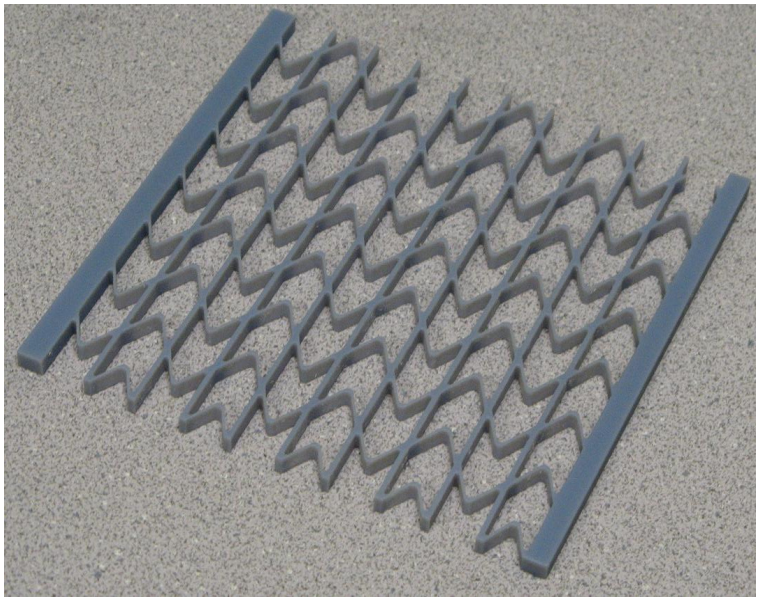

Fig. 63: Example of Objet PolyJet rapid-prototyped zero-Poisson honeycomb.

In Fig. 63, an example is given of a zero-Poisson substructure designed in SolidWorks and produced on an Objet PolyJet rapid prototype machine out of Vero Blue plastic. Using this method, a large number of samples could be fabricated with variations in bending member angle, θ. By testing these honeycombs on an MTS machine, a comparison could be made between the predicted effect of bending member angle on in-plane stiffness and the actual observed effect.

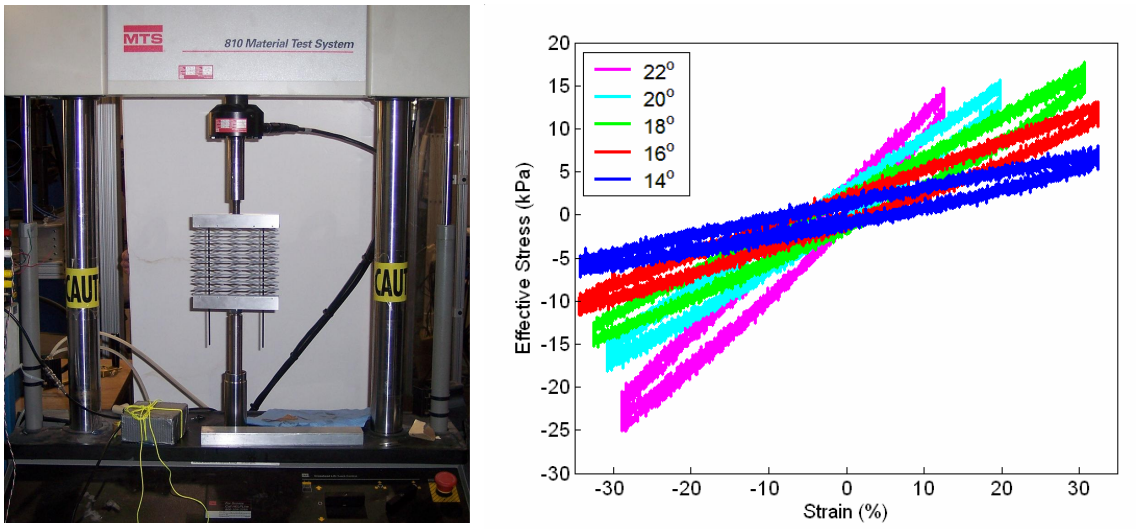

(a) **(b)**

Fig. 64: Substructure testing (a) substructure on MTS machine; (b) stress-strain curves of substructures of various interior angles.

The stress-strain test data from a series of rapid prototyped honeycombs is presented in Fig. 64. Each honeycomb was tested over the intended operating range, starting at 67% of resting length and extending to 133% of resting length to achieve 100% length change. To test the validity of the modified Gibson-Ashby model, comparisons of experimental data and analytical predictions were made. The stiffness modulus of each experimentally tested honeycomb was determined by applying a linear least squares regression to the data in Fig. 64. The resulting stiffnesses were then plotted with the analytical predictions from Eq. (32) in Fig. 65.

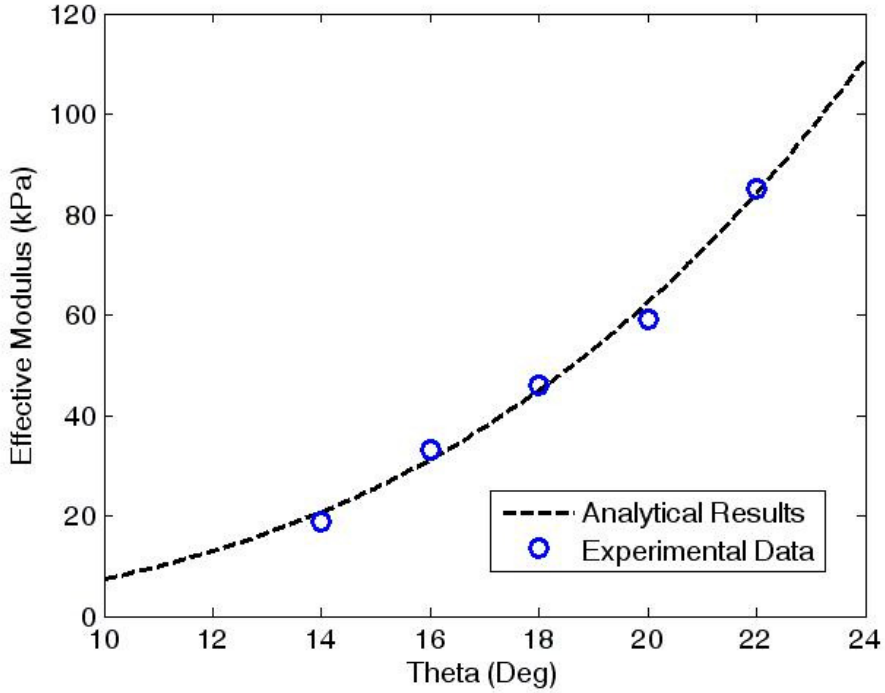

Fig. 65: In-plane substructure stiffness, analytical versus experiment.

The strong correlation between the analytical predictions and measured behavior suggests the assumptions made in the modified Gibson-Ashby equation are accurate over the intended operating range of the honeycomb substructure, and local strains are indeed relatively low. Having low local strain is a benefit as it will increase the fatigue life of the substructure. To minimize the in-plane stiffness of the substructure, the lowest manufacturable bending member angle, 14°, was selected for integration into complete morphing skin prototypes. Furthermore, this testing demonstrated the usefulness of the modified Gibson-Ashby equation, Eq. (32), for future honeycomb substructure design efforts. The in-plane stiffness of zero-Poisson honeycomb structures can be predicted analytically based upon geometry and material properties.

3.3.2 Honeycomb Substructure FEM Analysis

Along with analytical modeling and experimental testing, an FEM analysis of the zero-Poisson honeycomb substructure was conducted to examine strain behavior. Specifically, identifying the maximum local strain could be useful for fatigue analysis in future work. A geometrically nonlinear analysis was conducted on the honeycomb model shown in Fig. 66 under a prescribed displacement at the top in the *z*-direction. The structure was clamped at the bottom and constrained to remain parallel to the *x*-*z* plane as it underwent 76.2 mm (3 in) contraction and extension, equivalent to +/-50% strain. The honeycomb material, VeroBlue, is isotropic with a Young's modulus of E = 2.7 GPa and an assumed Poisson's ratio ν = 0.3. Ten-node tetrahedral solid elements, provided by a commercial program, COSMOSDesignSTAR, are used for the analysis.

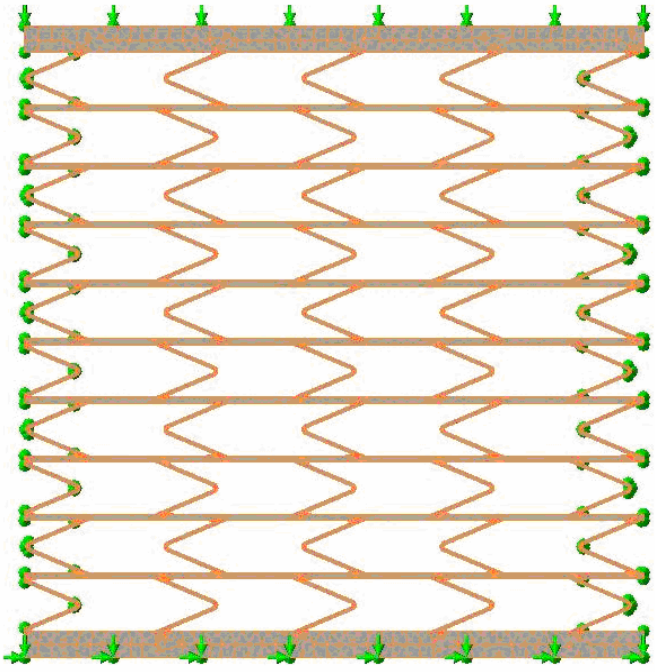

Fig. 66: Geometry, boundary conditions and meshes for honeycomb model.

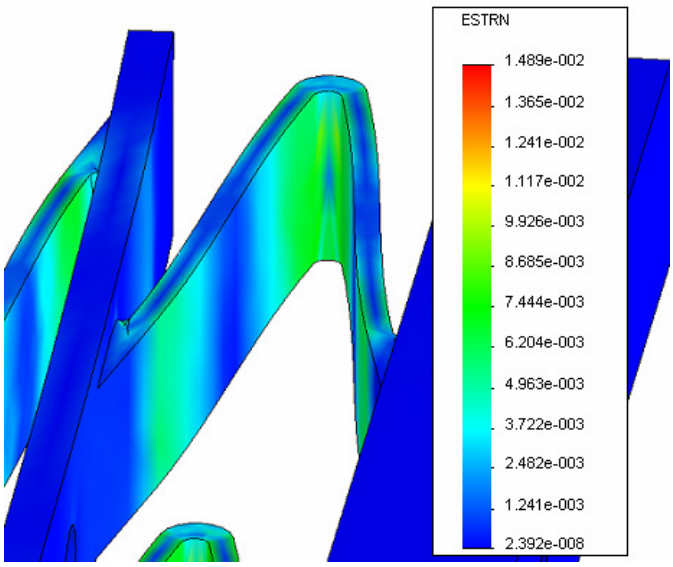

Fig. 67: Local strain during 30% global compression, max local strain = 1.5%.

The FEM results indicate low local strain for a single bending member compared with global strain, as Fig. 67 illustrates. The honeycomb sees a maximum local strain of 1.5% while undergoing 30% compression globally, a 20:1 ratio. This offers hope that a honeycomb substructure capable of high global strains with a long fatigue life can be designed by minimizing local strain, an area which should be a topic of further research.

3.3.3 Carbon Fiber Stringers

One unfortunate aspect of the zero-Poisson honeycomb described above is the lack of bending stiffness about the axis perpendicular to the rib members. Another structural element is needed to reinforce the substructure for out-of-plane loads. In order to reinforce the substructure, carbon fiber "stringers" were added perpendicular to the rib members. Simply comprised of carbon fiber rods sliding into holes in the substructure, the stringers reinforce the honeycomb against bending about the transverse axis. The placement of the carbon fiber stringers in the overall morphing skin arrangement is illustrated in Fig. 68a.

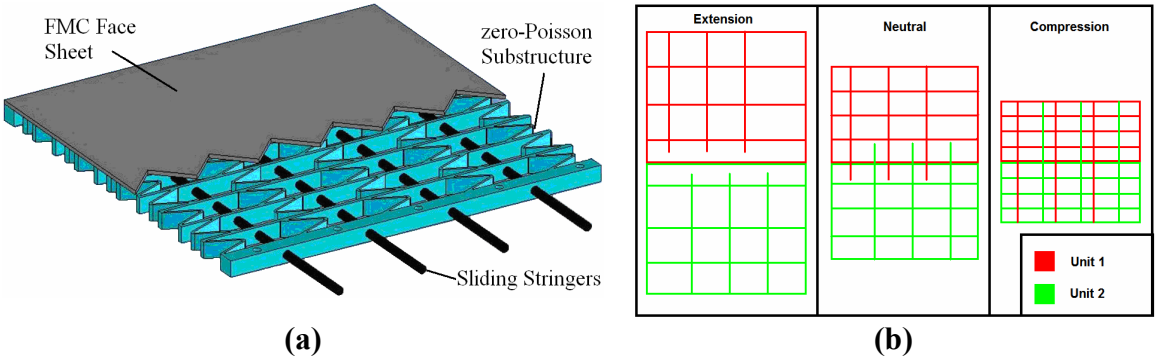

Fig. 68: Reinforced morphing skin cells (a) design of a single cell; (b) interleaving system arrangement.

Because the stringers are of a fixed length, when the morphing skin is less than fully extended, they will protrude from the morphing unit. There are a number of possible ways to mitigate this effect. For example, one concept consists of a system of two adjacent units with interleaving stringers as in Fig. 68b. When compressed, the stringers slide into the adjacent unit such that the combined system undergoes 100% shape change with no fixed length members protruding. Alternatively, for a span-morphing wingtip comprised of only one morphing unit, the sliding stringers could slide into empty space in the fixed wing structure when the wingtip is compressed. There are a number of other suitable ways to address this issue; the selection of a method would depend on the system integration requirements of a given UAV installation.

3.3.4 FMC/Substructure Adhesive

In order to integrate the FMC face sheets with the honeycomb substructure, a suitable bonding agent was necessary. The desired adhesive was required to bond the silicone elastomer FMC to the plastic rapid prototyped honeycomb, while withstanding the shear forces generated while deforming the structure to high strain levels. In addition, the

adhesive also needed to be capable of high strain levels in order to match the local strain of the FMC at the bond site.

Due to the fact that the substructure, and not the FMC itself, would be attached to the actuation mechanism, the adhesive was required to transfer all the force necessary to strain the FMC sheet. Based upon the known stiffness of the FMCs selected for integration into the morphing skin prototype, the adhesive was required to withstand up to 10.5 N/cm of skin width. The adhesive would be bonding the FMC along a strip of plastic 2.54 cm deep, so the equivalent shear strength required was 41.4 kPa.

The following two adhesive candidates were selected for testing:

1. Dow Corning 700 Industrial Grade Silicone Sealant. This is a one-part silicone rubber that is resistant to weathering and withstands temperature extremes.
2. Dow Corning 3-4207 Tough Dielectric Gel. This is the same material that was initially considered as a potential FMC candidate, but during sample preparation and testing, it was discovered that the characteristics of this particular elastomer depended on the mold release, and it turns out that it also demonstrates notable adhesive properties.

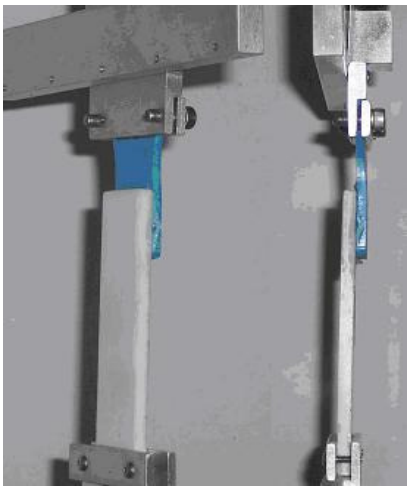

Fig. 69: Two views of a lap shear test sample.

Both candidates were silicone-based to promote adhesion to the silicone FMC skin, and both were capable of high levels of strain. Lap shear specimens as shown in Fig. 69 were prepared for testing with a 6.45 cm^2 bonded area and placed in the MTS machine. The upper portion of the test specimen is a sample of V-330/CA-35 matrix material and the lower portion is a molded polyurethane coupon similar to the material from which the honeycomb structure was fabricated. In this arrangement, the bonded joint is in the middle and the exterior ends are clamped in aluminum fixtures. Note that the fixtures allow for an offset to transfer the force in shear through the bonded joint.

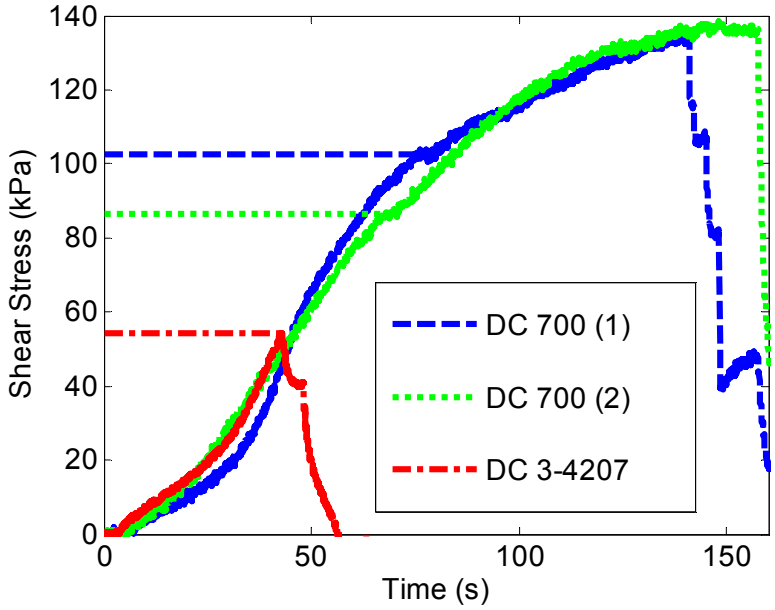

Fig. 70: Adhesive lap shear test results, horizontal lines indicate failure.

The testing procedure simply pulled the elastomer and plastic away from each other until failure occurred. Failure was defined as the first drop in stress, indicating the adhesive had begun to tear. Three tests were conducted using one sample of DC 3-4207 and two samples of DC-700, the results of which are displayed in Fig. 70. Shown are the measured stresses for two DC-700 samples of different joint thicknesses (0.71 mm –

dashed/blue; 0.64 mm – dotted/green) and one 3-4207 sample of comparable thickness (0.51 mm – dash-dot/red). Horizontal dotted lines indicate the onset of failure, where the first reduction in stress occurred. The 3-4207 sample fails before either of the two DC-700 samples, at a stress of approximately 62 kPa. The thinner sample of DC-700 (dotted/green) fails just above 83 kPa, whereas the thicker sample (dashed/blue) does not begin to fail until 103 kPa. However, because it would be difficult to precisely control the bonding layer thickness when attaching the FMC to the honeycomb core, the lowest DC-700 result (83 kPa) was chosen for comparison to the 3-4207 (62 kPa).

Sufficient evidence was provided in this experiment to demonstrate that the DC-700 was a more suitable adhesive for bonding the FMC elastomer matrix to the modified re-entrant honeycomb. Not only did the DC-700 fail at a higher stress than the DC 3-4207, but the initial tear in both DC-700 samples did not immediately propagate through the adhesive layer. The DC-700 samples continued to carry stress until total failure occurred at up to half again as high a stress level, giving it a safety factor of approximately 2. Assuming that future design and manufacturing advances can bring skin stiffness down even further, the already acceptable safety factor of this adhesive has positive implications for the safety and reliability for an actual UAV morphing skin application.

3.4 Integration and Final Testing

Two 152 mm x 152 mm morphing skin samples, Skin #1 and Skin #2, were fabricated from FMC #1 and FMC #2, respectively. VeroBlue 14° angle honeycomb was used for the substructure for both skins, and DC 700 adhesive was used to bond the two FMCs to their respective honeycombs. To assist in the attachment, the rib members of the honeycomb core were designed with raised edges on one side, as shown in Fig. 71a. This

figure shows a side view of the zero-Poisson honeycomb, where it can be seen that the top surface has the ribs extended taller than the bending members. Therefore, the bonding layer can be applied to the raised rib surfaces and pressed onto the FMC without bonding the bending members to the FMC. A sectional side view of a single honeycomb cell, shown in Fig. 71b, illustrates how the bonded morphing skin looks. A thin layer of adhesive is shown between the FMC and the ribs of the honeycomb, but it does not affect the movement of the bending members. The first morphing skin sample, Skin #1, was fabricated using this bonding method.

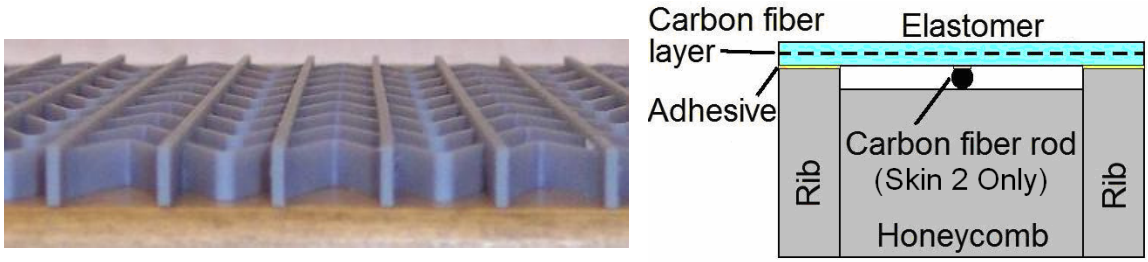

(a) **(b)**

Fig. 71: FMC-structure bonding method (a) honeycomb core; (b) single cell diagram.

A further addition to the substructure reinforcing the FMC sheet was considered for use in the final test article. This concept employed 1.27 mm carbon fiber rods running along the rib direction underneath the FMC, placed between each pair of ribs. The purpose of this concept was to further increase the out-of-plane resistance of the face sheet by adding rigid members at the point of maximum deflection (center point between ribs) and provide a means of comparison for Skin #1. The second morphing skin sample, Skin #2, incorporated added stiffener rods in its construction, shown optionally in Fig. 71b. Silicone adhesive was applied to the FMC to hold the rods in place, although this proved to be a difficult task and a large amount of adhesive was required to ensure good

bonding. The upper and lower surfaces of the assembled Skin #2 sample are displayed in Fig. 72 in neutral position. The carbon fiber stiffener rods are visible as black lines parallel to the ribs on the underside of the sheet.

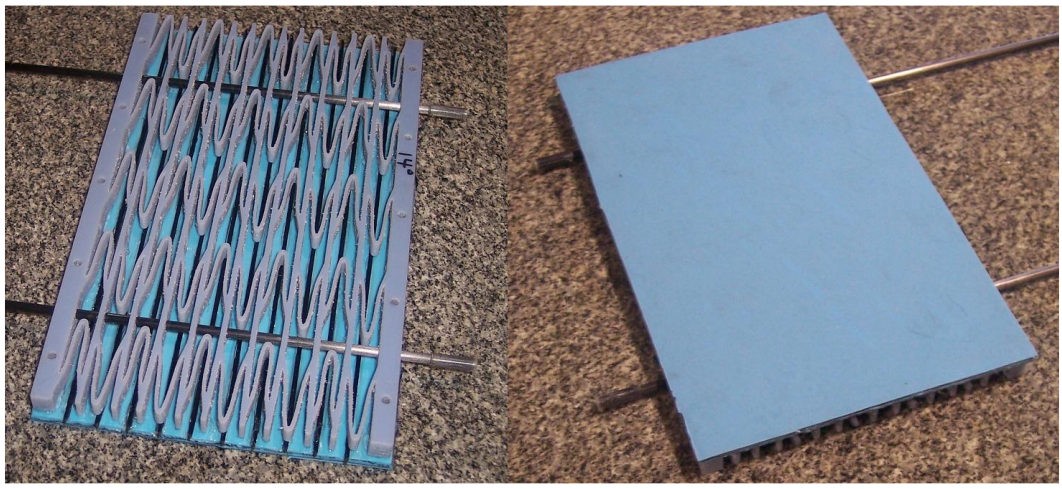

Fig. 72: Completed sample, Skin #2.

The two assembled morphing skin samples were used to assess in-plane and out-of-plane stiffness and select a morphing skin configuration. The configurations of the two morphing skins are summarized in Table 2. The selected design was used to fabricate a final 165 mm x 330 mm test article for combination and evaluation with the actuation system.

Table 3: Morphing Skin Samples, Summary

Test Article	FMC	Honeycomb	Adhesive	Additional Reinforcement
Skin #1	FMC #1, 1.4 mm thick, two CF layers at 0^o	14^o zero-Poisson rapid prototyped VeroBlue	DC-700	None
Skin #2	FMC #2, 1.7 mm thick, two CF layers at 0^o	14^o zero-Poisson rapid prototyped VeroBlue	DC-700	Carbon fiber rods between ribs

3.4.1 In-Plane Testing

Skin #1 and Skin #2 were tested on an MTS machine to 50% strain. The level of strain was limited in order to prevent unforeseen damage to the morphing skins before they could be tested for out-of-plane stiffness as well. In Fig. 73a, Skin #1 is shown undergoing testing, with results from both morphing skins presented in Fig. 73b. Note that the test procedure strained the specimens incrementally, holding the position briefly before starting with the next stage. This is the cause for the dips in force seen in the figure.

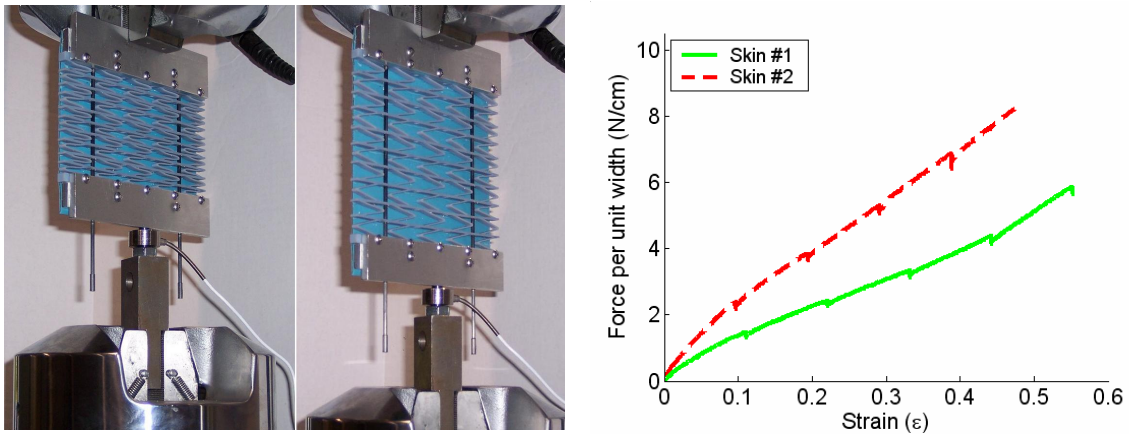

(a) (b)

Fig. 73: Morphing skin sample in-plane testing (a) assembled skin on MTS; (b) data from morphing skin in-plane testing.

Skin #2 demonstrated nearly twice the stiffness of Skin #1, which is at least partly due to the higher stiffness FMC incorporated into Skin #2. However, close examination of the previously measured stiffnesses of the individual components used in both of these morphing skins reveals the percentage contribution due to each structural element. These levels of stiffness contribution are broken down in Fig. 74.

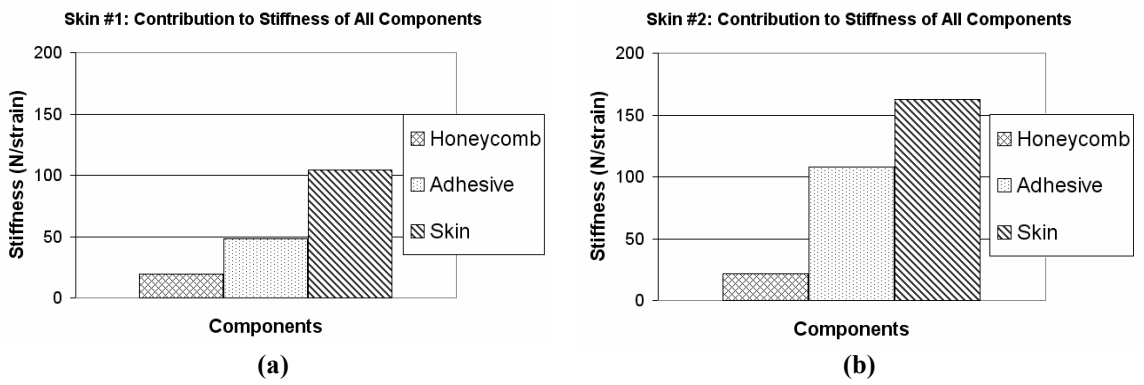

Fig. 74: Contributions to in-plane stiffness (a) Skin #1; (b) Skin #2.

It becomes clear that not only was FMC #2 in Skin #2 stiffer than FMC #1, but Skin #2 had a much higher adhesive stiffness, both relatively and absolutely. The additional carbon fiber ribs added to Skin #2 were not expected to impact in-plane stiffness, but the additional adhesive needed to bond them to the FMC skin still required energy to strain along with the FMC. The extra adhesive needed for the carbon fiber ribs more than doubled the adhesive stiffness contribution of Skin #2 as compared to Skin #1.

3.4.2 Out-of-Plane Deflection

The final phase of evaluation for the two morphing skin samples required a method of measuring out-of-plane deflection under distributed loadings, approximating aerodynamic forces. A number of testing protocols were investigated, including ASTM standard D 6416/D 6416M for testing simply supported composite plates subject to a distributed load. This particular test protocol is intended for very stiff composites, not flexible or membrane-like composites.

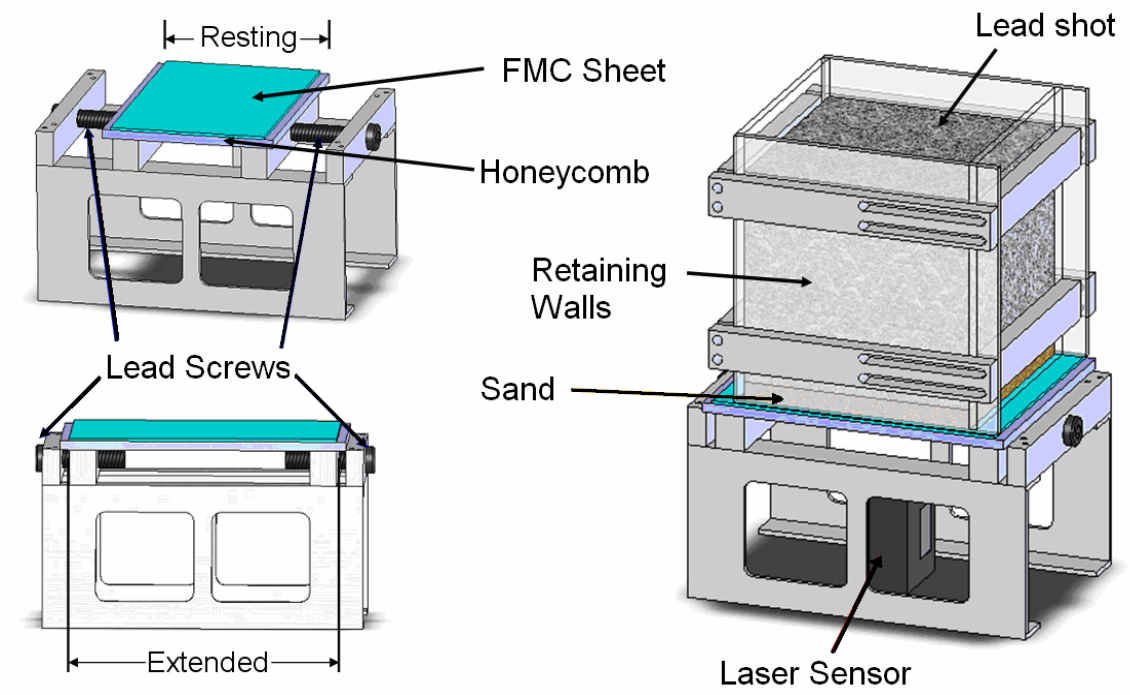

Fig. 75: Out-of-plane deflection test apparatus design.

A simpler approach to the problem was adopted wherein acrylic retaining walls were placed above the morphing skin sample into which a distributed load of lead shot and sand could be poured. The final configuration of the out-of-plane deflection testing apparatus can be seen in Fig. 75. A set of lead screws stretched the morphing skin sample from rest to 100% strain. The acrylic retaining walls could be adjusted to match the active skin area, and were tall enough to contain lead shot equivalent to a distributed load of 200 psf (9.58 kPa). By applying a thin layer of sand directly to the surface of the skin, the weight of the lead shot was distributed relatively evenly over the surface of the FMC. Moreover, as the skin deflected under load, the sand would adjust to conform to the surface and continue to spread the weight of the lead. A single-point laser position sensor was also placed underneath to measure the maximum deflections at the center of the skin, between the rib members. The assembled out-of-plane deflection loading apparatus is shown in Fig. 76a, with the complete test setup in Fig. 76b.

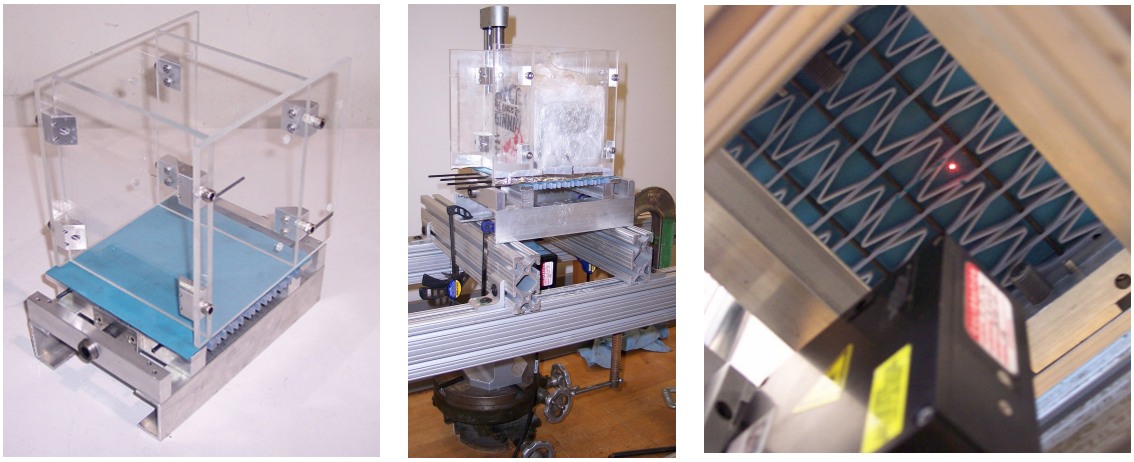

(a) (b) (c)

Fig. 76: Out-of-plane deflection testing (a) test apparatus; (b) laboratory setup; (c) measurement method.

The test procedure for each morphing skin covered the full range of operation, from resting (neutral position) to 100% area change. Lead screws were used to set the skin to a nominal strain condition between 0% and 100% of the resting length. The laser position sensor shown in Fig. 76c was positioned in the center of a honeycomb cell at the center of the morphing skin, where the greatest deflection is seen. This positioning was achieved using a small two-axis adjustable table seen at the bottom of Fig. 76b. The laser was zeroed on the under-surface of the FMC, and the relative distance to the bottom of an adjacent rib was measured. This established a zero measurement for rib deflection as well. A layer of sand of known weight was poured onto the surface of the FMC, and lead shot sufficient to load the skin to one of the three desired distributed loads was added to the top of the sand. Wing loadings of 40 psf (1.92 kPa), 100 psf (4.79 kPa), and 200 psf (1.92 kPa) were simulated. Once the load had been applied, measurements were taken at the same points on the CMC and the adjacent rib to determine deflection. These measurements were repeated for four different strain conditions (0, 25%, 66%, 100%) and the three different noted distributed loads for Skin #1 and Skin #2.

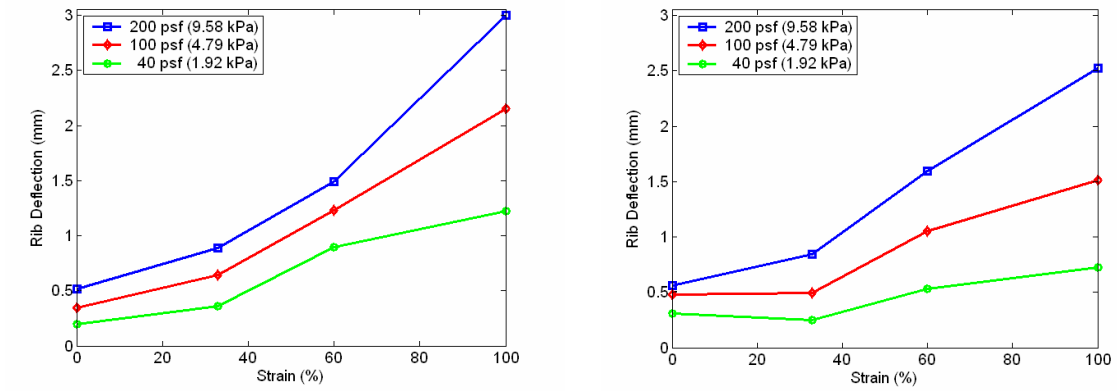

Skin #1 **Skin #2**

Fig. 77: Out-of-plane deflection results as measured on the center rib.

Experimental results from the two morphing skins are provided in Fig. 77. It was observed that, relative to the rib deflections, the FMC sheet itself deflected very little (less than 0.25 mm). The results in Fig. 77 therefore ignore the small FMC deflections and show only the maximum deflection measured on the rib at the midpoint of each morphing skin. Overall, the morphing skin deflections show that as the skin is strained and unsupported length increases, the out-of-plane deflection increases. Naturally, the deflection increases with load, as well. This shows that only one condition (maximum strain, maximum load, on Skin #1) exceeds the specified tolerance of 2.5 mm (10 mil) deflection.

3.4.3 Full-Scale Integration and Evaluation

Based on the results of the previous two sections, the final skin chosen for employment in the morphing cell demonstration device was Skin #1, which was shown to reach over 100% stretch with the lowest in-plane stiffness and largely acceptable out-of-plane performance. A 34.3 cm x 14 cm morphing skin, nominally identical to Skin #2 in configuration, was fabricated and attached to the actuation assembly. The actuation assembly, honeycomb sub-structure, and completed morphing cell can be seen in Fig. 78.

Individual components of the system are pictured in Fig. 78a, while the assembled morphing skin test article appears in Fig. 78b. The active region stretches from 9.1 cm to 18.3 cm with no transverse contraction, thus, producing a 1-D, 100% increase in surface area with zero Poisson's ratio.

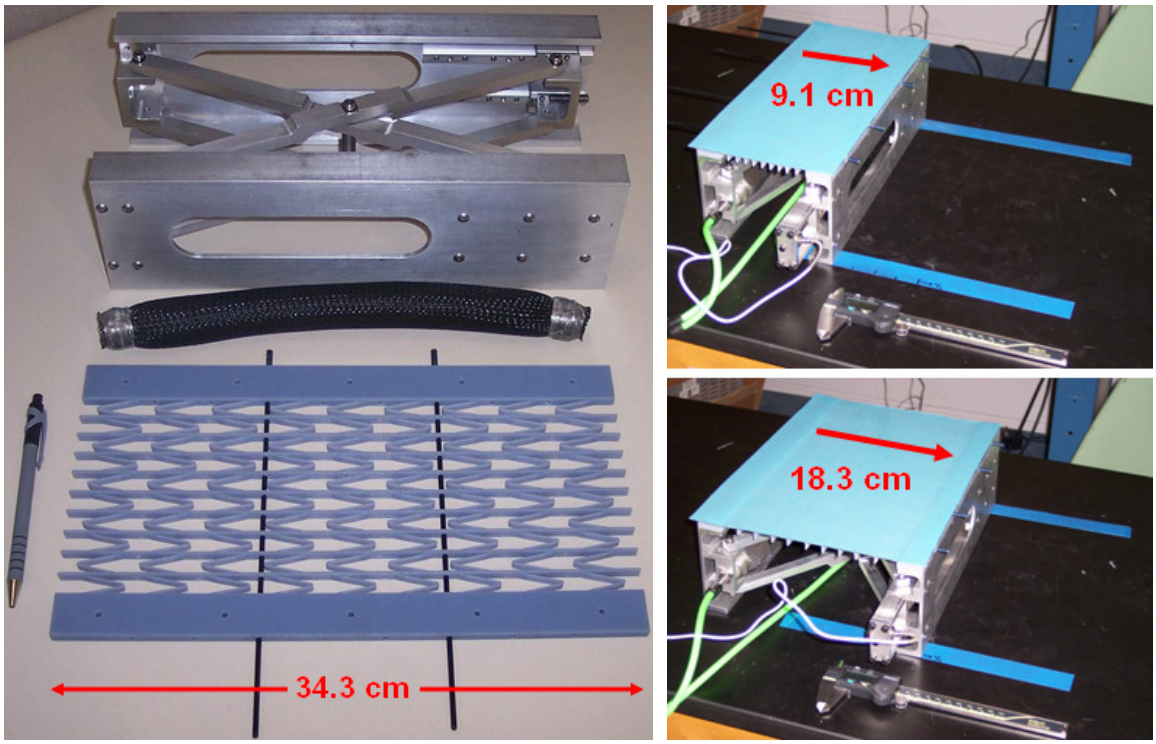

(a) (b)

Fig. 78: Integration of morphing cell (a) actuation and sub-structure components; (b) complete morphing cell exhibiting 100% area change.

To characterize the static performance of the morphing cell, input pressure to the PAM actuators was increased incrementally from approximately 70 kPa to 620 kPa. The strain of the active region was recorded at each input pressure, and a load cell in line with one PAM recorded actuator force for comparison to predicted values. This measurement process was repeated three times, recording strain, input pressure, and actuator force at each point. Note that the entire upper surface of the FMC is not the active region: each of the fixed-length ends of the honeycomb was designed and manufactured with 25.4 mm of

excess material to allow adequate FMC bonding area and an attachment point to the mechanism. This inactive region can be seen on the top and bottom of the honeycomb shown in Fig. 78a. The two extremities of the arrows in Fig. 78b also account for the inactive region at both ends of the morphing skin.

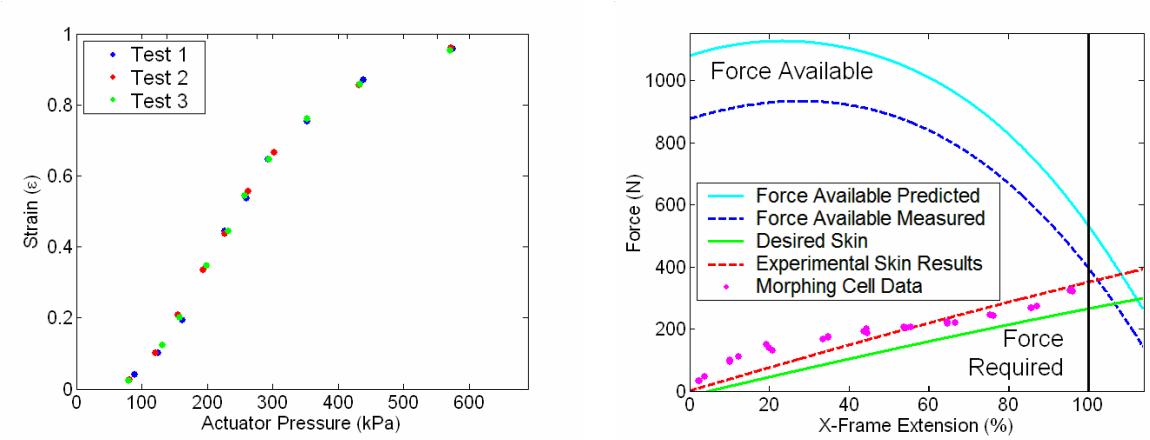

(a) **(b)**

Fig. 79: Morphing cell data (a) static performance; (b) comparison with predictions.

The static strain response to input actuator pressure is displayed in Fig. 79. Strain is seen to level off with increasing pressure due to a combination of mechanism kinematics and the PAM actuator load lines, but the system was measured to achieve 95% strain at 585 kPa and was observed at 100% strain at slightly over 620 kPa.

The measured system performance matches analytical predictions very closely. Evidence is shown in Fig. 79b, where the morphing skin data points overlay the force-displacement data collected during in-plane skin testing. The previously mentioned analytical predictions and associated experimental data for the actuation system and skin performance are also repeated in this figure. The morphing cell performance data, while not perfectly linear, approximately matches the slope of the experimental skin stiffness and intersects the actuation system experimental data near 100% extension. Furthermore, although the performance data falls roughly 15% short of original predictions, the

morphing skin meets the design goal, validating the analytical design process. Losses were not included in the original system predictions. However, the margin of error included in the original design for friction, increased skin stiffness, and other losses enabled the final morphing cell prototype to achieve 100% strain. It should also be noted that 100% area increases could be achieved repeatedly at 1 Hz using manually controlled actuator pressurization.

3.5 Conclusions

A passive 1-D morphing skin was designed for use on an existing pneumatic actuation system. The skin consisted of an FMC face sheet with a zero-Poisson honeycomb substructure intended to support out of plane loads. In-plane stiffness was controlled to match the capabilities of the actuator by careful design and testing of each separate skin component. Complete morphing skins were tested for in-plane and out-of-plane performance and integrated with the actuator to validate the design process.

1. An analytical design procedure was used to size individual morphing skin components so their combined stiffness matched actuator capabilities. FMC performance was calculated using classical laminated plate theory with modified micromechanics, successfully predicting in-plane skin stiffness and Poisson ratio. A zero-Poisson honeycomb substructure was also designed using a modification to Gibson and Ashby's analytical method to accurately predict in-plane stiffness.
2. Using FEM analysis, the local strain in the honeycomb bending members was determined to be an order of magnitude lower than global strain. For +/-30% global strain, the maximum local strain was approximately 1.5%. Based on this result, it is

expected a zero-Poisson honeycomb can be designed to achieve high strain with a reasonable fatigue life.

3. A multi-step composite lay-up procedure was developed for fabrication of FMC skins. The novel procedure relied on the properties of Rhodorsil V-330 CA-35 silicone, in particular the ability to bond pre-cured sheets of V-330 using more V-330 as the adhesive. This enabled FMC skins to be produced with a continuous matrix but different fiber volume fractions in distinct lamina, all using a minimum amount of tooling.
4. Design goals of 100% global strain and 100% area change were demonstrated on a laboratory prototype using the combined morphing skin and actuation mechanism. The morphing skin strained smoothly and exhibited a very low in-plane Poisson's ratio. Actuation frequencies of roughly 1 Hz were achieved.

Chapter 4

Conclusions and Future Work

4.1 Summary of Research and Technical Contributions

The research presented here had two major components which were directed at developing different aspects of a span morphing wingtip. First a control scheme was considered and tested in simulation and experiment for a pneumatic artificial muscle driven extension mechanism. Second a 1-D morphing skin prototype was designed, fabricated, and demonstrated in operation.

4.1.1 PAM Actuator Controller

In Chapter 2, the effectiveness of controlling a Pneumatic Artificial Muscle actuation system through linear control was investigated. A Single PAM Test Apparatus was constructed to provide experimental data over a range of operating conditions against which modeling efforts could be compared. The actuation system was then modeled in Simulink as a combination of analytical expressions from theory and lookup tables based upon characterization of individual components. In particular, the system dynamics and mass flow of air were handled using well-known equations, while the PAM force and volume, spring force, and spool valve cross sectional area were described using experimental data.

Initially, a Simulink model of the pneumatic system was developed and tested against data captured while charging and exhausting a fixed volume cylinder. A tubing loss term given by Richer and Hurmuzlu was found to degrade rather than improve model

predictions, and was replaced by a pressure drop term from basic hydrodynamic internal flow which was iterated at each time step. Subsequently, a full dynamic Simulink model of the actuation system was built and validated using experimental data from the SPTA. The model showed acceptable performance over a range of conditions, matching the data qualitatively and in most cases quantitatively as well.

Finally, two linear controllers using displacement feedback were compared in the Simulink model, one PI and one PID. Ziegler-Nichols tuning was used to determine controller gains. The PID controller was found to be superior in frequency response and final waveform shape, and was subsequently implemented on the SPTA test article. The closed loop experimental system tracked sine inputs with no amplitude attenuation and little phase lag up to 10 Hz. Tracking of waveforms with higher order harmonics to simulate aerodynamic control inputs was demonstrated by the model, but in experiment the PID controller performed poorly at this task, suggesting limitations in the model for predicting the upper limit on input frequency for the system.

4.1.2 Morphing Skin

In Chapter 3, the proposed morphing skin technology was successfully demonstrated through design, fabrication, and testing of a morphing skin. Analytical predictions of FMC in-plane stiffness based on CLPT methods were validated through in-plane testing of individual FMC skin samples. These predictions aided in selecting a skin configuration to match in-plane stiffness goals. Analytical methods were also developed to predict in-plane stiffness of a zero-Poisson honeycomb substructure. Experimental testing of a range of honeycomb substructures validated the predictions and enabled a minimum stiffness honeycomb to be selected. Lap shear testing helped select the appropriate

adhesive to bond the FMC and substructure based upon ultimate strength requirements. In-plane and out-of-plane testing of two different morphing skin candidates demonstrated the viability of the concept by meeting design goals and aided in selecting the best skin available for production as a full-size test article. Finally, a prototype pneumatic actuation system was used to demonstrate the ability of a morphing skin panel to achieve 100% 1-D area change with zero Poisson's ratio.

4.1.3 Technical Contributions

The controller results are promising in that a major hurdle of employing PAM actuators, controllability, was overcome for modest frequencies with a linear PID controller which was simple to tune and implement. Past research which has succeeded at achieving actuation frequencies greater than 1 Hz has focused exclusively on adaptive or nonlinear controllers for PAM systems, so that the results of this work are important for establishing the usefulness and also the limitations of linear controls for PAM actuators.

The main technical contributions of the morphing skin development were two-fold: first, advancements were made to the methods of reinforcing elastomeric morphing skins through the use of anisotropic fiber and a novel honeycomb substructure. Specifically, manufacturing and integration issues were addressed by fabrication a skin panel in a manner which has not been demonstrated in the literature. Second, the design of this morphing skin relied on simple analytical methods which were demonstrated to be effective at predicting in-plane stiffness and which can be applied to future morphing skins of a similar configuration.

4.2 Future Work

The actuation system developed in Chapter 2 was useful as a test article, but is limited in scope and the results may not be directly applicable to a morphing aircraft design. The opposing nonlinear spring load on the actuator provides a reasonable approximation of the work required to strain a morphing skin, but is not representative of the changing aerodynamic loads a morphing actuation system might encounter on an aircraft. These loads would depend heavily on the type of craft, the type and design of the morphing system, and flight conditions, and controller response should be tested under a variety of more complex simulated loads to ensure a linear controller will be adequate.

Furthermore, while the results presented here encourage interest in the described control approach, the controlled PAM system response was only simulated in this work. The immediate next step in developing PAM actuation systems for a morphing craft is closed loop implementation on the SPTA. Discrepancies between the model and the physical system could prove significant enough that changes to the controller are necessary, or could even highlight the need for a more robust controller.

The morphing skin research in Chapter 3 has laid the groundwork for future analytical design and development of viable morphing structures that are capable of producing broad-scale area changes and airframe reconfigurations. As described in the motivation of this research, such skin technology could be useful for a span-changing morphing aircraft. However, when considering integration of the technology into an aircraft, some issues must be addressed. First, the prototype system was a simple morphing cell of rectangular shape. Although this could conceivably illustrate a panel section of a wing, it is limited in application.

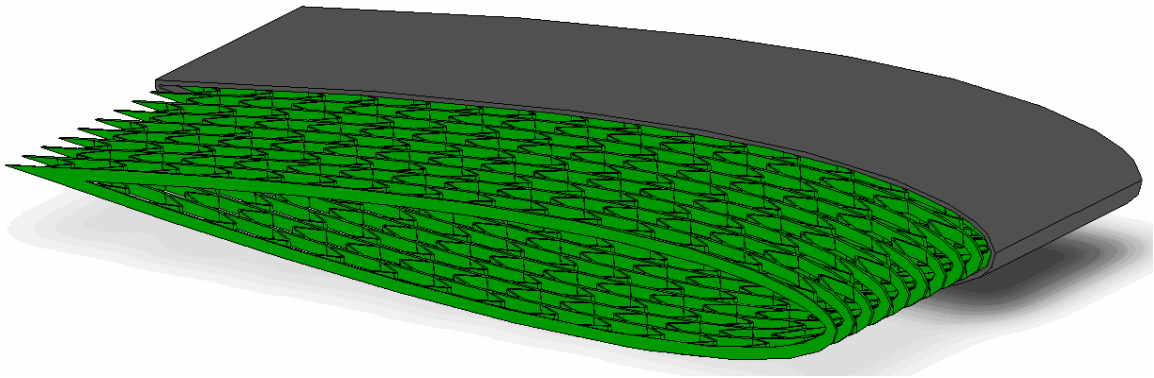

Fig. 80: Span extension of wing using airfoil-shaped substructure layer, chordwise fiber direction.

To increase the potential of this design, alternate implementation strategies should be examined. The most direct extension of the demonstrated technology is presented in Fig. 80. This concept shows a complete airfoil section that would be supported by a thin substructure layer, much like the test article described herein. The substructure in this figure is a zero-Poission honeycomb with airfoil-shaped rib members running along the chord to produce span extension morphing. The FMC sheet is shown to wrap completely around the airfoil/honeycomb sub-structure. An actuation system could then be housed within the hollow section of the airfoil, either the demonstrated pneumatic driven scissor mechanism or some other type of extension mechanism.

Chapter 5

References

[1] Anderson, J. D., *Introduction to Flight*, 2nd ed., McGraw-Hill, Inc., New York, 1985.

[2] Parker, H. J., "The Parker Variable Camber Wing," Report #77 Fifth Annual Report, National Advisory Committee for Aeronautics, Washington, D.C., 1920.

[3] Munk, M. M., "Note on the relative Effect of the Dihedral and the Sweep Back of Airplane Wings," NACA Technical Note 177, 1924.

[4] Buseman, A., "Aerodynamic Lift at Supersonic Speeds," Ae. Techl. 1201, Report No. 2844 (British ARC, February 3, 1937), Bd. 12, Nr. 6, October, 1935, p. 210-220.

[5] Sarh, B., 1991, "Convertible fixed wing aircraft," US Patent No. 4,986,493.

[6] Gevers, D. E., 1997, "Multi-purpose aircraft," US Patent No. 5,645,250.

[7] Blondeau, J. E., and Pines, D. J., "Pneumatic Morphing Aspect Ratio Wing," 45th AIAA/ASME/ASCE/AHS/ASC Structures, Structural Dynamics & Materials Conference, 19 - 22 Apr 2004, Palm Springs, CA, Paper No. AIAA 2004-1808.

[8] Toensmeier, P. A., "Morphing Aircraft Could Bring Multi-Role Capability to Next Generation Aircraft," *Aviation Weekly*, May 2005, p. 72-73.

[9] Gern, F. H., Inman, D. J., and Kapania, R.K., "Structural and Aeroelastic Modeling of General Planform Wings with Morphing Airfoils," *AIAA Journal*, 2002, 40(4): 628-637.

[10] Bae, J. S., Seigler, T. M., and Inman, D. J, "Aerodynamic and Static Aeroelastic Characteristics of a Variable-Span Morphing Wing," Journal of Aircraft, 2005, 42(2): 528-534.

[11] Henry, J. J., "Roll Control for UAVs by Use of a Variable Span Morphing Wing," Master's Thesis, Department of Aerospace Engineering, University of Maryland, College Park, MD, 2005.

[12] Thill, C., Etches, J., Bond, I., Potter, K., and Weaver, P., "Morphing Skins," *The Aeronautical Journal*, Vol. 112, No. 1129, March 2008, pp 117-139.

[13] Hetrick, J. A., Osborn, R. F., Kota, S., Flick, P. M., and Paul, D. B., "Flight Testing of Mission Adaptive Compliant Wing," *Proceedings of 48th AIAA Structures, Structural Dynamics, and Materials Conference*, 23 - 26 Apr 2007, Honolulu, HI, Paper No. AIAA 2007-1709.

[14] Perkins, D. A., Reed, J. L., and Havens, E., "Morphing Wing Structures for Loitering Air Vehicles," *45th AIAA Structures, Structural Dynamics & Materials Conference*, 19-22 April 2004, Palm Springs, CA, Paper No. AIAA 2004-1888.

[15] Bye, D. R., and McClure, P. D., "Design of a Morphing Vehicle," *48th AIAA Structures, Structural Dynamics, and Materials Conference*, 23 - 26 Apr 2007, Honolulu, HI, Paper No. AIAA 2007-1728.

[16] Kikuta, M. T., "Mechanical Properties of Candidate Materials for Morphing Wings," Master of Science Thesis, Virginia Polytechnic Institute and State University, Blacksburg, VA, 2003.

[17] Flanagan, J., Strutzenberg, R., Myers, R., and Rodrian, J., "Development and Flight Testing of a Morphing Aircraft, the NextGen MFX-1" *Proceedings of 48th AIAA Structures, Structural Dynamics, and Materials Conference*, 23 - 26 Apr 2007, Honolulu, HI, Paper No. AIAA 2007-1707.

[18] Wereley, N. M. and Kothera, C. S., "Morphing Aircraft Using Fluidic Artificial Muscles," *Proceedings of the International Conference on Adaptive Structures and Technologies*, 2-5 Oct 2007, Ottawa, ON, Paper ID 171.

[19] Caldwell, D.G., Medrano-Cerda, G.A., and Goodwin, M., "Control of Pneumatic Muscle Actuators," *IEEE Control Systems*, Feb 2005, pp 40-48.

[20] Medrano-Cerda, G.A., Bowler, C.J., and Caldwell, D.G., "Adaptive position control of antagonistic pneumatic muscle actuators," *IEEE/RSJ International Conference on Intelligent Robots and Systems*, Vol. 1, No. 1, Aug 1995.

[21] Kothera, C.S., Jangid, M., Sirohi, J., and Wereley, N.M., 2006, "Experimental Characterization and Static Modeling of McKibben Actuators," *ASME International Mechanical Engineering Congress and Exposition*, 5-10 Nov 2006, Chicago, IL, Paper No. IMECE2006-15390.

[22] Gentry, M. F., and Wereley, N. M., "Effects of Braid Angle on Pneumatic Artificial Muscle Actuator Performance," *Proceedings of the ASME Conference on Smart Materials, Adaptive Structures and Intelligent Systems,* 28-30 Oct 2008, Ellicott City, MD, Paper No. SMASIS2008-539.

[23] Nickel, V., et al., 1965, "Synthetically Powered Orthotic Systems," *Journal of Bone and Joint Surgery*, Vol. 47-B, Aug 1965, pp 458-464.

[24] Tondu, B. and Pierre, L., "Modeling and Control of McKibben Artificial Muscle Robot Actuators," *IEEE Control Systems Magazine*, Apr 2000, pp 15-38.

[25] Schroder, J., Erol, D., Kawamura, K., and Dillman, R., "Dynamic pneumatic actuator model for a model-based torque controller," *Proceedings 2003 IEEE International Symposium on Computational Intelligence in Robotics and Automation.*, Vol. 1, 16-20 Jul 2003, pp. 342-347.

[26] Paul, A.K., Mishra, J.K., and Radke, M.G., "Reduced Order Sliding Mode Control for Pneumatic Actuator," *IEEE Transactions on Control Systems Technology*, Vol. 2, No. 3, Sept 1994.

[27] Richer, E., and Hurmuzlu, Y., "A High Performance Pneumatic Force Actuator System: Part II – Nonlinear Controller Design," *ASME Journal of Dynamic Systems, Measurement, and Control*, Vol. 122 Sept 2000, pp. 426-434.

[28] Khalil, H. K., *Nonlinear Systems*, Prentice Hall, Upper Saddle River, 2002.

[29] Hildebrandt, A., Sawodny, O., Neumann, R., and Hartmann, A., "A Flatness Based Design for Tracking Control of Pneumatic Muscle Actuators," *Seventh International Conference on Control, Automation, Robotics and Vision*, Singapore, Dec 2002.

[30] van der Linde, R.Q., "Design, Analysis, and Control of a Low Power Joint for Walking Robots, by Phasic Activation of McKibben Muscles," *IEEE Transactions on Robotics and Automation*, Vol. 15, No. 4, Aug 1999.

[31] Chou, C.P., and Hannaford, B., "Measuring and Modeling of McKibben Pneumatic Artificial Muscles," *IEEE Transactions on Robotics and Automation*, Vol. 12, No. 1, Feb 1996.

[32] Gaylord, R., 1958, "Fluid actuated motor system and stroking device," US Patent No. 2,844,126.

[33] Richer, E., and Hurmuzlu, Y., "A High Performance Pneumatic Force Actuator System: Part I – Nonlinear Mathematical Model," *ASME Journal of Dynamic Systems, Measurement, and Control*, Vol. 122 Sept 2000, pp. 416-425.

[34] Al-Ibrahim, A. M., and Otis, D. R., "Transient Air Temperature and Pressure Measurements During the Charging and Discharging Processes of an Actuating Pneumatic Cylinder," *Proceedings of the 45th National Conference on Fluid Power*, 1992.

[35] Beater, P., *Pneumatic Drives: System Design, Modelling, and Control*, Springer, New York, 2007.

[36] Burrows, C. R., and Peckham, R. G., "Dynamic characteristics of a pneumatic flapper valve," *Proc Instn Mech Engrs*, *Journal of Mechanical Engineering Science*, Vol. 19(3), Part C, pp. 113-121.

[37] Pugi, L., Malvezzi, M., Allotta, B., Banci, L., Prescniani, P., "A parametric library for the simulation of a Union Internationale des Chemins de Fer (UIC) pneumatic braking system," *Proc Instn Mech Engrs*, *Journal of Rail and Rapid Transit*, Vol. 218, Part F, pp. 117-132.

[38] Carducci, G., Giannoccaro, N. I., Messina, A., and Rollo, G., "Identification of viscous friction coefficients for a pneumatic system model using optimization methods," *Mathematics and Computers in Simulation* 71, 2006, pp 385-394.

[39] Incropera, F. P., and DeWitt, D. P., *Fundamentals of Heat and Mass Transfer*, John Wiley & Sons, New York, 2006.

[40] Ziegler, J. G., and Nichols, N. B., "Optimum settings for automatic controllers," *ASME Transactions*, Vol. 64, 1942, pp. 759-768.

[41] Shen, J., Yang, M., and Chopra, I., "Swashplateless Helicopter Rotor with Trailing-Edge Flaps for Flight and Vibration Control," AIAA/ASME/ASCE/AHS/ASC 45th Structures, Structural Dynamics and Materials Conference, Palm Springs, CA, 2004.

[42] Hess, R. A., "Structural Model of the Adaptive Human Pilot," *AIAA Journal of Guidance and Control*, Vol. 3, No. 5, 1980, pp 416-423.

[43] Nieuwenhuizen, F. M., Beykirch, K. A., Mulder, M., Bulthoff, H. H., "Identification of Pilot Control Behavior in a Roll-Lateral Helicopter Hover Task," AIAA Modeling and Simulation Technologies Conference, 20 - 23 Aug 2007, Hilton Head, SC, Paper No. AIAA 2007-6799.

[44] Theodore, C. R., Tischler, M. B., Colbourne, J. D., "Rapid Frequency Domain Modeling methods for UAV Flight Control Applications," *AIAA Atmospheric Flight Mechanics Conference and Exhibit*, 11-14 Aug 2003, Austin, TX, Paper No. AIAA 2003-5538.

[45] Murray, G., Gandhi, F., and Bakis, C., "Flexible Matrix Composite Skins for One-Dimensional Wing Morphing," *Proceedings of 48th AIAA Structures, Structural Dynamics, and Materials Conference*, 23 - 26 Apr 2007, Honolulu, HI, Paper No. AIAA 2007-1737.

[46] Olympio, K. R., "Design of a passive flexible skin for morphing aircraft structures," M.S. Thesis, Pennsylvania State University, 2006.

[47] Agarwal, B. D., Broutman, L. J., and Chandrashekhara, K., *Analysis and Performance of Fiber Composites*, John Wiley & Sons, Hoboken, 2006.

[48] Gibson, L. J. and Ashby, M. F., *Cellular Solids: Structure and Properties*, Pergamon Press, Oxford, 1988.

[49] Chaves, F. D., Avila, J., and Avila, A. F., "A morphological study on cellular composites with negative Poisson's ratios," *Proceedings of 44th AIAA Structures, Structural Dynamics, and Materials Conference*, 7-10 Apr 2003, Norfolk, VA, Paper No. AIAA 2003-1951.

[50] Shigley, J., Mishke, C., and Budynas, R., *Mechanical Engineering Design*, McGraw-Hill, New York, 2004.